

FABRICATION AND CHARACTERIZATION OF MAGNETOTRANSPORT IN
COLOSSAL MAGNETORESISTIVE MANGANITE THIN FILMS AND HYBRID
STRUCTURES

By

SRINIVAS V. PIETAMBARAM

A DISSERTATION PRESENTED TO THE GRADUATE SCHOOL
OF THE UNIVERSITY OF FLORIDA IN PARTIAL FULFILLMENT
OF THE REQUIREMENTS FOR THE DEGREE OF
DOCTOR OF PHILOSOPHY

UNIVERSITY OF FLORIDA

2001

I would like to dedicate this dissertation to my dad, who has been my constant inspiration
and my mom, who didn't live to see me graduate

ACKNOWLEDGMENTS

Life is not an easy journey, especially for an international student who has to be away from his family in a far off land. I have found no justifiable way to thank and acknowledge all those who have helped me to be where I am today.

Firstly, I would like to express my heartfelt gratitude to my advisor, Dr. Rajiv K. Singh, for his guidance, support and encouragement. The freedom to try out various ideas and several valuable suggestions, he gave me helped me to learn more and realize the importance of creative thinking. Thanks are also due to my doctoral committee members, Dr. Stephen Pearton, Dr. Cammy Abernathy, Dr. Fred Sharifi and Dr. Wolfgang Sigmund, for their interest, discussions and assistance in this work. I would also like to thank all the professors in the Department of Materials Science and Engineering for my maturation as a scientist/engineer and as a person.

Special thanks are due to Dr. Dhananjay Kumar. He was the one who introduced me to the field of pulsed laser deposition, taught me the deposition technique and shared ideas and discussions throughout my research. He, along with my sister, Radhika, my brother-in-laws, Dr. Krishna Maruvada and Dr. Madhav Durbha, my friends Dr. Uday Mahajan, Anuranjan and Sai, helped me in many ways during my stay in Gainesville. I would like to thank Dr. Craciun for his helpful suggestions and XPS work. Also, I would like to thank Dr. Perriere of Universites Paris VII for his RBS work. Special thanks are also due to Dr. Hebbard and his students, Dr. Sharifi and his students and Brian Watson

for their upkeep of the SQUID magnetometer. The MAIC staff was also very helpful in teaching and troubleshooting their equipment.

I would also like to acknowledge my group members and other friends, who made graduate school a very pleasant experience. Thanks go to Ali, Anupam, Dr. Don Gilbert, Dr. Dong-Gu Lee, Frank, Hui, Dr. Hyoung-June Kim, Jaeyoung, Jeremiah, Dr. Jim Fitzgerald, Josh, Joodong, Katar, Kyo-Se, Dr. Kyu –Gong Cho, Marc, Mike, Nabil, Pankaj, Rajesh, Dr. Ravi Adimula, Sai Kiran, Sang Hyun, Seung-Mahn, Supriya, Usha, Won-Seok, Wonseop, Dr. Yun Daniel Park, Zhan and many others.

In closing, I would like to single out my father to express special thanks for his constant support and inspiration. I would also like to acknowledge my second sister, Aparna, for her support and advice.

TABLE OF CONTENTS

	<u>page</u>
ACKNOWLEDGMENTS	iii
LIST OF TABLES	viii
LIST OF FIGURES	ix
ABSTRACT.....	xiii
1. INTRODUCTION	1
Motivation and Objectives.....	1
Dissertation Outline	4
2. LITERATURE SURVEY	7
Magnetotransport/Magnetoresistance	7
Magnetic Recording Heads.....	8
Anisotropic Magnetoresistance (AMR).....	9
Giant Magnetoresistance (GMR).....	10
Colossal Magnetoresistance (CMR)	11
Introduction.....	11
Materials Properties of CMR Materials.....	14
CMR Effect in Thin Films	16
Structure-Property-Composition Correlation.....	18
Magnetic Properties	22
Mechanism of CMR – Possible Origins	23
Practical Limitations of CMR Materials and Efforts to Overcome Them.....	26
Pulsed Laser Deposition (PLD)	28
3. EXPERIMENTAL APPROACH.....	39
Target Preparation.....	39
Substrate Materials.....	39
CMR Film Fabrication	39
Characterization	40
X-Ray Diffraction (XRD)	41
Atomic Force Microscopy (AFM).....	41
Transmission Electron Microscopy (TEM)	42

Variable Angle Spectroscopic Ellipsometry (VASE).....	43
X-ray Photoelectron Spectroscopy (XPS)	43
Rutherford Back Scattering Spectrometry (RBS).....	44
SQUID Magnetization Measurements.....	44
Magnetization measurements.....	45
Magnetotransport measurements	47
4. EFFECTS OF POST DEPOSITION HEAT TREATMENT.....	52
Overview.....	52
Experimental Details.....	53
Results and Discussion	54
Structural and Chemical Characterization	54
Magnetoresistance Behavior.....	57
Magnetic Properties	62
Conclusions.....	63
5. STUDY OF SELF, EXTERNAL AND MIXED DOPED SYSTEMS.....	72
Overview.....	72
Experimental Details.....	73
Results and Discussion	74
Structural Characterization	74
Magnetoresistance Behavior.....	77
Magnetic Properties	82
Bolometric Properties	84
Conclusions.....	85
6. EFFECT OF A LOCAL FERROMAGNETIC BIASING FIELD	104
Overview.....	104
Effects of Magnetic and Non-Magnetic Impurity Addition	104
Overview.....	104
Experimental Details.....	105
Results and Discussion	106
Structural characterization	106
Magnetoresistance behavior.....	106
Magnetization measurements.....	110
Effect of Superlattice Configuration – Perovskite Oxide Superlattices.....	112
Overview.....	112
Experimental Details.....	113
Results and Discussion	114
Structural characterization	114
Magnetoresistance behavior.....	114
Magnetization measurements.....	116
Conclusions.....	117

7. CONCLUSIONS AND FUTURE WORK.....	128
Conclusions.....	128
Future Work.....	131
LIST OF REFERENCES	133
BIOGRAPHICAL SKETCH	142

LIST OF TABLES

<u>Table</u>	<u>Page</u>
3.1. Processing conditions for manganite thin films.....	40
4.1. Compositions of the LCMO films subjected to various post deposition heat treatments measured using RBS	55
6.1. MR ratio (%) of the films at low and high fields.....	107

LIST OF FIGURES

<u>Figure</u>	<u>Page</u>
1.1: Large magnetoresistance (dubbed colossal magnetoresistance) observed in $\text{La}_{0.7}\text{Ca}_{0.3}\text{MnO}_3$ epitaxial thin films.....	6
2.1: Schematic of s- and d- bands attributed to conduction with relative population and energy with respect to fermi energy	33
2.2: Geometry of a dual gap magnetoresistive (MR) recording head. The top shield of the read head element also serves as the bottom pole of the write element.....	34
2.3: Lattice structure and magnetic moments in LaMnO_3 (a) Sketch of the Jahn-Teller distorted LaMnO_3 lattice structure, (b) alignment of magnetic moment of Mn^{3+} ions based on Wollan's neutron study	35
2.4: Magnetic phase diagram of $\text{La}_{1-x}\text{Ca}_x\text{MnO}_3$	36
2.5: AFM surface images of (a) as-grown, (b) oxygen annealed and (c) argon annealed $\text{La}_{0.7}\text{Ca}_{0.3}\text{MnO}_3$ films grown on LaAlO_3	37
2.6: Schematic illustration of PLD experimental setup for large area processing by rastering of a large diameter target with rastered laser beam.....	38
3.1: Schematic illustration of 248 nm KrF excimer PLD system equipped with a multi-target carousel and its controller, ambient gas supplier, and programmable heating and cooling controller for fabricating CMR films.....	50
3.2: Schematic of SQUID magnetometer detection and electronics. Note that the sample is usually placed in a plastic sample holder, which is moved up and down along the coils to induce current in the circuit. The sample is centered in the middle of the coil by fully sweeping along the sample traverse range. During measurement, usually three sweeps are made for averaging purposes and with a scan length of 4 cm. Along the scan, 32 separate measurements are made, which are fitted to a signal of certain emu	51
4.1: X-ray diffraction patterns of $\text{La}_{0.7}\text{Ca}_{0.3}\text{MnO}_3$ films, (a) no anneal, (b) 900 °C oxygen anneal, and (c) 900 °C argon anneal.....	65

4.2: RBS spectra (random and channeling) of $\text{La}_{0.7}\text{Ca}_{0.3}\text{MnO}_3$ films, (a) no anneal, (b) 900 °C oxygen anneal, (c) 900 °C argon anneal, (d) 500 °C oxygen anneal, and (e) 500 °C argon anneal	66
4.3: XPS spectra of the as-deposited, 900 °C oxygen and argon annealed films (a) Mn 2p and (b) O 1s regions	67
4.4: Variation of electrical resistance with temperature for (a) no anneal, (b) 900 °C oxygen anneal, (c) 900 °C argon anneal, (d) 500 °C oxygen anneal, and (e) 500 °C argon anneal (filled circle (0 T), filled diamond (2 T) and filled triangle (5 T))	68
4.5: Variation of MR ratio with temperature for $\text{La}_{0.7}\text{Ca}_{0.3}\text{MnO}_3$ films subjected to various post deposition heat treatments.....	69
4.6: Variation of magnetization with temperature at 0.5 T for $\text{La}_{0.7}\text{Ca}_{0.3}\text{MnO}_3$ films as deposited and annealed at 900 °C in oxygen and argon ambient.....	70
4.7: <i>M-H</i> curves at 10 K for $\text{La}_{0.7}\text{Ca}_{0.3}\text{MnO}_3$ films as deposited and annealed at 900 °C in oxygen and argon ambient	71
5.1: X-ray diffraction patterns of (a) $\text{La}_{0.7}\text{Ca}_{0.3}\text{MnO}_3$, (b) $\text{La}_{0.7}\text{Ca}_{0.2}\text{MnO}_3$, and (c) $\text{La}_{0.7}\text{MnO}_3$ targets synthesized using a ceramic route.....	87
5.2: X-ray diffraction patterns of (a) $\text{La}_{0.7}\text{Ca}_{0.3}\text{MnO}_3$, (b) $\text{La}_{0.7}\text{Ca}_{0.2}\text{MnO}_3$, and (c) $\text{La}_{0.7}\text{MnO}_3$ films grown at 700 °C on (100) LaAlO_3 substrates	88
5.3: AFM micrographs of (a) $\text{La}_{0.7}\text{Ca}_{0.3}\text{MnO}_3$, (b) $\text{La}_{0.7}\text{Ca}_{0.2}\text{MnO}_3$, and (c) $\text{La}_{0.7}\text{MnO}_3$ films grown at 700 °C on (100) LaAlO_3 substrates.....	89
5.4: Multi-beam diffraction contrast images of the cross sections of (a) $\text{La}_{0.7}\text{Ca}_{0.3}\text{MnO}_3$, (b) $\text{La}_{0.7}\text{Ca}_{0.2}\text{MnO}_3$, and (c) $\text{La}_{0.7}\text{MnO}_3$ films grown at 700 °C on (100) LaAlO_3 substrates	90
5.5: Electron diffraction patterns of the cross sections of (a) $\text{La}_{0.7}\text{Ca}_{0.3}\text{MnO}_3$, (b) $\text{La}_{0.7}\text{Ca}_{0.2}\text{MnO}_3$, and (c) $\text{La}_{0.7}\text{MnO}_3$ films grown at 700 °C on (100) LaAlO_3 substrates	91
5.6: Selected area diffraction pattern of the cross section of the $\text{La}_{0.7}\text{MnO}_3$ film grown at 700 °C on (100) LaAlO_3 substrates.....	92
5.7: High resolution transmission electron microscopy images of the cross sections of (a) $\text{La}_{0.7}\text{Ca}_{0.3}\text{MnO}_3$, (b) $\text{La}_{0.7}\text{Ca}_{0.2}\text{MnO}_3$, and (c) $\text{La}_{0.7}\text{MnO}_3$ films grown at 700 °C on (100) LaAlO_3 substrates	93
5.8: Resistance versus temperature plots for (a) $\text{La}_{0.7}\text{MnO}_3$, (b) $\text{La}_{0.7}\text{Ca}_{0.2}\text{MnO}_3$, and (c) $\text{La}_{0.7}\text{Ca}_{0.3}\text{MnO}_3$ films in 0 and 5 T magnetic field	94

5.9: Variation of MR ratio with temperature for $\text{La}_{0.7}\text{MnO}_3$ (filled square), $\text{La}_{0.7}\text{Ca}_{0.2}\text{MnO}_3$ (filled triangle), and $\text{La}_{0.7}\text{Ca}_{0.3}\text{MnO}_3$ (filled circle) films.....	95
5.10: Low temperature (below $T_c/2$) resistance fits for $\text{La}_{0.7}\text{Ca}_{0.3}\text{MnO}_3$ (filled circle), $\text{La}_{0.7}\text{Ca}_{0.2}\text{MnO}_3$ (filled triangle), and $\text{La}_{0.7}\text{MnO}_3$ (inset) films at 0 and 5 T	96
5.11: Resistance temperature fits for $\text{La}_{0.7}\text{Ca}_{0.3}\text{MnO}_3$ (filled circle), $\text{La}_{0.7}\text{Ca}_{0.2}\text{MnO}_3$ (filled triangle), and $\text{La}_{0.7}\text{MnO}_3$ (filled square) films at 0 and 5 T up to T_c	97
5.12: Low temperature MR for $\text{La}_{0.7}\text{Ca}_{0.3}\text{MnO}_3$ (filled circle), $\text{La}_{0.7}\text{Ca}_{0.2}\text{MnO}_3$ (filled triangle), and $\text{La}_{0.7}\text{MnO}_3$ (filled square) films at 3 T. Inset shows the low-temperature MR for $\text{La}_{0.7}\text{Ca}_{0.3}\text{MnO}_3$ at 5 T	98
5.13: High-temperature resistance fits for $\text{La}_{0.7}\text{Ca}_{0.3}\text{MnO}_3$ (filled circle), $\text{La}_{0.7}\text{Ca}_{0.2}\text{MnO}_3$ (filled triangle), and $\text{La}_{0.7}\text{MnO}_3$ (filled square) films	99
5.14: Variation of magnetization with temperature for $\text{La}_{0.7}\text{Ca}_{0.3}\text{MnO}_3$ (filled circle), $\text{La}_{0.7}\text{Ca}_{0.2}\text{MnO}_3$ (filled triangle), and $\text{La}_{0.7}\text{MnO}_3$ (filled square) films at 0.5 T	100
5.15: M - H curves for (a) $\text{La}_{0.7}\text{Ca}_{0.3}\text{MnO}_3$, (b) $\text{La}_{0.7}\text{Ca}_{0.2}\text{MnO}_3$, and (c) $\text{La}_{0.7}\text{MnO}_3$ at 10 K.	101
5.16: Saturation magnetization fits for $\text{La}_{0.7}\text{Ca}_{0.3}\text{MnO}_3$ (filled circle), $\text{La}_{0.7}\text{Ca}_{0.2}\text{MnO}_3$ (filled triangle), and $\text{La}_{0.7}\text{MnO}_3$ (filled square) films up to $T_c/2$	102
5.17: TCR and T_p for $\text{La}_{0.7}\text{Ca}_{0.3}\text{MnO}_3$ (filled circle), $\text{La}_{0.7}\text{Ca}_{0.2}\text{MnO}_3$ (filled triangle), and $\text{La}_{0.7}\text{MnO}_3$ (filled square) films	103
6.1: X-ray diffraction patterns of (a) $\text{La}_{0.7}\text{Ca}_{0.3}\text{MnO}_3$, (b) Ag added $\text{La}_{0.7}\text{Ca}_{0.3}\text{MnO}_3$, and (c) Co added $\text{La}_{0.7}\text{Ca}_{0.3}\text{MnO}_3$ films grown on LaAlO_3 substrates.....	119
6.2: Resistance versus temperature plots for (a) $\text{La}_{0.7}\text{Ca}_{0.3}\text{MnO}_3$, (b) Ag added $\text{La}_{0.7}\text{Ca}_{0.3}\text{MnO}_3$, and (c) Co added $\text{La}_{0.7}\text{Ca}_{0.3}\text{MnO}_3$ films in 0, 0.1 and 5 T	120
6.3: Variation of MR ratio with temperature for (a) $\text{La}_{0.7}\text{Ca}_{0.3}\text{MnO}_3$, (b) Ag added $\text{La}_{0.7}\text{Ca}_{0.3}\text{MnO}_3$, and (c) Co added $\text{La}_{0.7}\text{Ca}_{0.3}\text{MnO}_3$ films in 0.1 and 5 T	121
6.4: Variation of magnetization for the films with temperature at 0.5 T	122
6.5: Symmetric X-ray diffraction patterns of various superlattices (legend inset shows each type of super lattice).....	123
6.6: (a) High-resolution TEM micrograph and (b) corresponding SAD pattern of a typical superlattice (18/5).....	124
6.7: Resistance versus temperature plots for (a) 18/1, (b) 18/2, (c) 18/5, and (d) 18/8 superlattices in 0 T (circle) and 5 T (triangle) fields	125
6.8: Variation of MR ratio with temperature for various superlattices in 5 T field.....	126

6.9: Variation of magnetization with temperature for various superlattices at 150 G.....	127
--	-----

Abstract of Dissertation Presented to the Graduate School
of the University of Florida in Partial Fulfillment of the
Requirements for the Degree of Doctor of Philosophy

FABRICATION AND CHARACTERIZATION OF MAGNETOTRANSPORT IN
COLOSSAL MAGNETORESISTIVE MANGANITE THIN FILMS AND HYBRID
STRUCTURES

By

Srinivas V. Pietambaram

August 2001

Chairman: Rajiv k. Singh

Major Department: Materials Science and Engineering

The continually increasing demand for magnetic information storage and retrieval has driven a significant worldwide effort to improve the performance of relevant hard ware components. As the areal density continues to increase, more sensitive materials and innovative structures will be required to detect the decreasing fringe fields emanating from the media. Doped manganites in thin film form are being examined as a possible next generation magnetoresistance sensor material. The magnetoresistance of these doped manganite thin films is of unprecedented magnitude; however, these large resistance changes are achieved only in a strong field in the Tesla range, thus severely limiting their practical utility. This dissertation addresses some of the critical parameters, which influence the properties and efforts to reduce the field scale necessary to observe high magnetoresistance ratios in these films.

The primary deposition technique used in this work is pulsed laser deposition. Initial work was concentrated on the optimization of various process parameters to obtain high quality thin films of manganites. Systematic post deposition heat treatments in oxygen and argon ambient at elevated temperatures revealed that transition temperature is related to the Mn-O fraction and uniform distribution of oxygen across the films rather than just the oxygen content of the films as proposed by others. MR ratio is improved by the improvement in the microstructure (recrystallization and grain growth) of the films after annealing; however vacancies created on the lanthanum site by the high temperature anneal also seem to be an important factor in the determination of the MR ratio.

Self-doped, mixed doped and external doped lanthanum manganite thin films, where the external dopant is Ca, have shown different transition temperature and MR ratios. The variation in the insulator-to-metal transition could be explained on the basis of Mn^{4+} content while the MR property seemed to be related to the microstructure of the films (impurities, defects, grain boundary and domain wall scattering).

A novel way to reduce the fields necessary to produce high magnetoresistance ratios in doped manganites may be to provide a local biasing field. This local biasing field may be generated either by the addition of a magnetic impurity (such as cobalt in this study) or by another ferromagnetic film in close proximity as that in a superlattice configuration. Indeed, an enhancement in magnetoresistance was observed in both the studies.

CHAPTER 1 INTRODUCTION

Motivation and Objectives

Mention magnetism and an image arises in one's mind of a small boy playing with a magnet, trying to attract a variety of things or of researchers in dusty physics labs with iron filings under their finger nails, but not the stuff from which career dreams are spun. Think of the giant magnetic recording industry; it is a major world industry that is experiencing an above average growth. The magnetism story does not end with recording. New technology and applications are being developed for ultra-sensitive magnetic sensors and magnetoresistive random access memory technology, bringing back excitement in magnetism [Sim95].

Magnetic recording and optical recording are the major technologies used to produce long term storage of information in today's computer systems. Magnetic recording has been used for data storage in computer systems for over 40 years, and the advances that have occurred in that time frame are nothing short of phenomenal. One might expect that after forty years of dominance, the rate of progress in magnetic recording would be slowing down and that other technologies would be moving in to replace it. However, rather than slowing down its rate of progress, magnetic recording is now advancing at a faster rate than before. The materials used in magnetic recording heads have recently received a tremendous amount of attention. Ever-increasing demands

for information storage, especially for graphics-intensive applications, have necessitated unprecedented increases in disk-drive areal densities.

This continually increasing demand for magnetic information storage and retrieval has driven a significant worldwide effort to improve the performance of relevant hardware components. Modern magnetic recording heads and disk drives utilize a thin magnetoresistive element, made out of permalloy, which senses the slight change in resistance (about 2%) that occurs as the angle of magnetization is changed when the magnetized data bits pass beneath the head. For ultra high recording densities the signal strength produced in the heads diminishes considerably. Therefore, more sensitive materials and innovative structures will be required to detect the decreasing magnetic fringe-fields emanating from the media.

Doped LaMnO_3 in thin film form is being examined as a possible next generation magnetoresistance sensor material. Large magnetoresistance was observed in the 1970s and 1980s in bulk ceramic and single-crystal forms of doped manganite perovskites. The recent interest in magnetoresistance in doped perovskite manganites was initiated by the discovery of a large room-temperature magnetoresistance in epitaxial thin films [Von93]. Fabrication of thin films with large magnetoresistance at room temperatures is key for application of these materials in read heads for hard disk drives and magnetic random access memories.

For CMR effects in both bulk and thin film materials, the basic phenomenon seems to be the same. Over an appreciable range of doping, these materials exhibit a very large magnetoresistance effect at temperatures close to where they undergo a ferromagnetic-paramagnetic transition [Von93, Cha93, Jin94, Ju94] (see Figure 1.1). The

basic manganite, LaMnO_3 , is antiferromagnetic and insulating. Partial doping of La sites with alkaline earth cations in LaMnO_3 results in a $\text{Mn}^{3+}/\text{Mn}^{4+}$ mixed valence state which is responsible for both metallic conductivity and ferromagnetism in accordance with double exchange interaction [Jon50, Zen51, DeG59].

The magnetoresistance of manganites is of unprecedented magnitude; however, these large resistance changes are achieved only in a strong field in the Tesla range, thus severely limiting their practical utility. Reducing the field scale and increasing the operating temperature has been the goal of a number of research groups worldwide. Some important parameters, whose effect on the properties of the films are not clearly understood and need further study, are oxygen content and crystallinity of the films. To reduce the field scale for realizing high magnetoresistance ratios, three different approaches have been reported in the literature. One is to study the magnetotransport properties due to spin dependent transport across grain boundaries, both natural and artificial. Another approach exploits the naturally occurring two-dimensional structure in the layered derivative of the manganese perovskite compounds, where inter-plane transport exhibits low-field magnetoresistance. The third approach involves spin-dependent tunneling magnetoresistance across a ferromagnetic electrode/insulating barrier/ferromagnetic electrode tri-layer structure. Another novel approach, which needs to be explored, may be by providing a local biasing field. This local biasing field may be generated either by the addition of a magnetic impurity or by another ferromagnetic film in close proximity as that in a superlattice configuration.

Creating vacancies on the lanthanum site instead of chemical doping by a divalent ion like Ca, Ba, etc. is another way to produce colossal magnetoresistance. This unique

system is known as a self doped system. A comparison of the transport and magnetic properties of self, external and mixed doped (has both vacancies and external doping) systems will give useful insights into the physics of magnetotransport and the mechanism of colossal magnetoresistance in these systems.

Dissertation Outline

In chapter 2 an overview of the literature survey on the related subjects to this research is presented. The mechanism of colossal magnetoresistance currently understood, critical parameters which influence the properties of these thin films, some of the effects not clearly understood, the practical limitations in the utilization of these thin films and approaches used by researchers to overcome these limitations are discussed briefly in this chapter. Chapter 3 discusses the experimental procedure used to grow colossal magnetoresistant thin films and characterization techniques used to characterize the properties of these films.

The properties of manganite thin films are highly sensitive to post deposition heat treatments. In the early studies on CMR materials, a post deposition anneal at high temperature was critical for obtaining large magnetoresistance. However, it was not clear whether the improvement was due to improvement in microstructure or increase in the oxygen content of the film or any subtle changes in the composition. Different groups have studied this outstanding issue, but some aspects of the study still remain unclear. We have performed a systematic study to discern these effects by annealing in various ambients and followed them with various characterization techniques to get a clear picture. The results are presented in chapter 4. $\text{La}_{1-x}\text{MnO}_3$ is unique among the manganite systems by virtue of showing high magnetoresistance ratios without external doping.

Chapter 5 explains the differences in transport and magnetic properties of self, mixed and external doped lanthanum manganites with the same lanthanum content. The former study is important from the fundamental view of understanding the structure-composition-property relationship, while the latter is important for the physics of magnetotransport and the type of magnetic excitations in these systems which might throw a light on the mechanism of colossal magnetoresistance.

The magnetoresistance of doped manganites is of unprecedented magnitude; however, these large resistance changes are achieved only in a strong field in the Tesla range, thus severely limiting their practical utility. Reducing the field scale and increasing the operating temperature have been the goals of a number of research groups worldwide. A novel approach to reduce the field scale is to provide a local biasing field. The biasing field can be provided either by addition of a magnetic impurity or by another ferromagnetic film in close proximity as that in a superlattice configuration. Chapter 6 discusses these effects in detail. Chapter 7 gives a summary of the whole study and future directions.

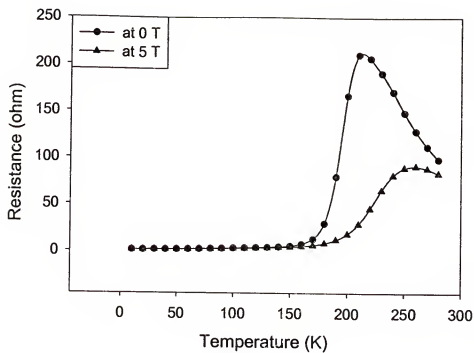


Figure 1.1: Large magnetoresistance (dubbed colossal magnetoresistance) observed in $\text{La}_{0.7}\text{Ca}_{0.3}\text{MnO}_3$ epitaxial thin films [Pie98a]

CHAPTER 2 LITERATURE SURVEY

Magnetotransport/Magnetoresistance

All charged carriers are affected by magnetic fields. Applied magnetic fields have many wide-ranging effects from the Hall effect to lowering the mean free path as electrons precess along the applied field under Lorentz forces. The resistivity dependent on the square of the magnetic field is sometimes referred to as ordinary magnetoresistance. Ever since Mott [Mot64], the general assumption of transport and conduction in ferromagnets is that it is carried by two independent channels that are parallel, one for spin up or majority spin and the other for spin down or minority spin. Generally, spin-flip scattering mechanisms do not dominate until temperatures are much higher than ferromagnetic ordering temperatures. Other scattering processes such as defects, impurities, surfaces, and interfaces complicate this simple view of independent and parallel channels.

Another influential scattering mechanism is scattering between s- and d- bands, which are generally attributed to conduction in the ferromagnetic transition metals. The d-band plays a particularly important role since it is the final state of this scattering process. A schematic of the band energies is shown in Figure 2.1. The asymmetry in population and energies explains ratios of resistivity of minority spin to majority spin as high as ten for certain alloys. How the d-band distorts in applied magnetic fields gives the subtle foundations of anisotropic magnetoresistance, AMR [McG75], discussed later in the chapter.

Magnetic Recording Heads

The materials used in the magnetic recording heads have recently received a tremendous amount of attention. Ever-increasing demands for information storage, especially for graphics-intensive applications, have necessitated unprecedented increases in disk-drive areal densities. Combined with this are recent discoveries in the area of magnetoresistive materials, enabling the design and fabrication of much more sensitive recording heads.

The recording heads that are used in high-performance disk drives typically consist of separate magnetoresistive head and inductive write heads as shown in Figure 2.2. Previously, a single inductive head performed both the functions. Separation of the two heads allows each to be optimized for its individual function, an essential factor in enabling disk drives to contain gigabytes of storage. The write head consists of a U-shaped ferromagnet surrounding a set of coils. The ends of the ferromagnet are the magnetic poles defining the write gap. When current passes through the coils, a field bridges the gap, setting the orientation of the magnetization in the media. Information is stored by changing the polarity of the current in order to write a pattern of magnetic domains in the media.

The read head senses the stored information in the media by detecting the fringe fields from the transitions between oppositely magnetized domains. The fields are detected by a magnetoresistor using a simple two-point resistance measurement. The resolution of the head is determined by its size: delineated in the cross-track direction by the distance between the contacts on the sensor and along the track by the separation of the magnetic shielding. The contact separation is generally several micrometers, and typical shield-to-shield distances are 0.2-0.3 μm .

The areal density that can be achieved depends on the properties of the magnetic recording medium, the distance between the medium and the read head, and the sensitivity of the recording head. Higher sensitivity allows smaller bits to be detected and loosens the restraint on flying height. The sensitivity is dependent on the particular type of magnetoresistive material used. Various magnetoresistive materials and the origin of magnetoresistance in these materials will be discussed in the following sections.

Anisotropic Magnetoresistance (AMR)

The term anisotropic magnetoresistance describes the fact that magnetoresistance differs depending on the geometry of the orientation of the transport current and the applied magnetic field. It results from an anisotropic scattering mechanism such as that provided by spin-orbit coupling, which is a relativistic effect [Par94]. In the case when the current is parallel to the applied field, the magnetoresistance (MR) is positive; i.e., the resistance increases as the applied field is increased. This response is also referred to as longitudinal AMR. When the current is perpendicular to the applied field, the MR is negative; i.e., the resistance decreases as the applied field is increased. Like longitudinal AMR, this geometry labels this response as transverse AMR. The value quoted for AMR is the percent change of resistance from the parallel to the perpendicular case. Typical AMR values are 3-5% at room temperature [Cam82].

AMR has been successfully developed in such applications as read-head for hard disk drive applications and have replaced inductive heads. Due to the relatively small but well-behaved percent change, AMR structures are limited to devices with minimum sizes of a couple of micrometers. For structures at smaller dimensions, the device resistance increases and the MR signals are no larger than background noises. To overcome these limitations, there has been a considerable interest in developing structures consisting of

magnetic multilayers (exhibiting GMR) and in searching for materials exhibiting higher magnetoresistance values.

Giant Magnetoresistance (GMR)

An interesting and well-studied phenomenon in magnetic multilayers is oscillatory ferromagnetic coupling between magnetic layers separated by a non-ferromagnetic spacer layers [All98]. Such a coupling mechanism has been observed in many ferromagnetic layers and many spacer layers (which include non-ferromagnetic transition metals [Par91] and noble metals [Ben90]). The coupling energy oscillates depending on the spacer thickness, changing from ferromagnetic coupling (magnetization is parallel) to anti-ferromagnetic coupling (magnetization is anti-parallel), between two or more ferromagnetic layers.

Such a phenomenon has been predicted in theory for metallic multilayer systems but not demonstrated until the late 1980s [Fer94]. In metallic systems the conduction electrons are delocalized and are able to “carry” magnetic exchange through non-ferromagnetic metallic spacer layers. In general terms, the conduction electrons mediate the coupling, which is described by the RKKY (Ruderman-Kittel-Kasuya-Yosida) interaction [Rud54]. Reviews of the oscillatory coupling behavior in magnetic multilayer structures are found in the literature. Studies of this phenomenon led inadvertently to the discovery of Giant Magnetoresistance (GMR). Researchers in France conducting transport experiments on Fe/Cr anti-ferromagnetically coupled multilayers found negative magnetoresistance (i.e., resistance decreases as the applied field is increased) with the change in resistance being orders of magnitude higher than AMR [Bai88].

GMR can be explained in terms of bulk or interface scattering as the mean free paths of minority spin and majority spin carriers are altered. There are many theories

proposed for GMR, with both semi-classical and quantum mechanical models as examples [Cam 89, Lev90]. Semi-classical models introduced parameters such as relaxation times and transmission coefficients to account for various scattering mechanisms. The Boltzmann equation is then used to describe how the perturbation of electron distribution is affected by neighboring magnetic layers [Bar90]. A limit to the semi classical approach occurs as the magnetic thickness approaches zero. Quantum mechanical models predict that the resistivity varies as $1/t^2$ and fit the experimental data better for thin films [Fis89]. The key to successful quantum mechanical modeling is to accurately describe the spin scattering of free electrons.

Anti-parallel magnetization between successive magnetic layers is very important for GMR. Hence, many clever ways to achieve such an alignment have been developed. An excellent review of various GMR structures is given in Dieny [Die94].

Colossal Magnetoresistance (CMR)

Introduction

As the areal density continues to increase, more sensitive materials and innovative structures will be required to detect the decreasing magnetic fringe fields emanating from the media. One of the promising alternatives is colossal magnetoresistant (CMR) material. These materials were recently discovered in manganite perovskite thin film materials such as $\text{La}_{0.67}\text{Ca}_{0.33}\text{MnO}_{3+\delta}$. The resistance in thin-film samples was reduced by 99.9 % (normalized with respect to low field resistance) at 77 K with the application of a magnetic field of 6 T, which is dubbed as colossal magnetoresistance to distinguish it from giant magnetoresistance.. CMR has been observed in perovskite structures of the general formula, $\text{A}_{1-x}\text{B}_x\text{MnO}_{3+\delta}$, where A = La, Pr, Nd, and B = Ba, Sr, Ca, Pb. In this dissertation, some of the outstanding issues and novel approaches to reduce the field scale

necessary to produce CMR will be reported. In the following sections, a brief review on the history and current understanding of the phenomenon of CMR will be presented.

Large magnetoresistance (MR) was observed in the 1970s and 1980s in bulk ceramic and single-crystal forms of doped perovskites. Large negative magnetoresistance was observed in bulk doped perovskite manganite $\text{Nd}_{0.5}\text{Pb}_{0.5}\text{MnO}_3$, for which a magnetic-field-induced change in resistance $\Delta R/R (H=0) > 50\%$ was found near its ferromagnetic transition at a temperature of 184 K [Kus89]. Here $R (H=0)$ is the resistance in zero field $H=0$, and $\Delta R = R (H=0) - R (H \neq 0)$. Earlier, Searle and Wang [Sea69] had reported spin-dependent metal-insulator transitions in single crystals of $(\text{LaPb})\text{MnO}_3$. The recent interest in doped perovskite manganites was initiated by the discovery of large room-temperature magnetoresistance in epitaxial thin films [Von93]. Thin films with large room temperature open up new possibilities for applications in diverse areas of technology such as magnetic random access memories and read heads for hard disk drives. With the efforts invested in the commercialization of high temperature superconductors – a class of doped cuprate perovskites with materials characteristics similar to those of the doped manganite perovskites, thin film deposition technology for complex oxide materials has seen rapid strides. Doped manganite perovskites were successfully synthesized in thin film form first by Kasai and Ohno [Kas90] when they reported their work on the superconducting proximity effect in sandwiched epitaxial $\text{YBa}_2\text{Cu}_3\text{O}_7 / \text{La}_{0.7}\text{Ca}_{0.3}\text{MnO}_3 / \text{YBa}_2\text{Cu}_3\text{O}_7$ thin films. Also, Cho et al. [Cho90] reported successful synthesis of $\text{La}_{0.7}\text{Sr}_{0.3}\text{MnO}_3$ in epitaxial form by rf diode magnetron sputtering in 1990.

In 1993, Von Helmolt et al. [Von93] reported a large negative magnetoresistance effect, of the order $\Delta R/R (H=0) > 60\%$ at room temperature in a 7-tesla field, in laser

deposited thin film $\text{La}_{0.67}\text{Ba}_{0.33}\text{MnO}_x$. This was soon followed by the report of McCormack et al. [McC94] and Jin et al. [Jin94] of their findings that thin film $\text{La}_{0.67}\text{Ca}_{0.33}\text{MnO}_3$ exhibits $\Delta R/R$ ($H=6$ T) = 127000 % at 77 K. This large magnetoresistance effect has since been referred to as “colossal magnetoresistance” (CMR). In these early studies a post deposition anneal (900 °C, 30 min, oxygen atmosphere) was critical for obtaining large magnetoresistance [McC94, Jin94, Von93]. However, it was not clear whether the improvement was due to improvement in microstructure, increase in the oxygen content of the film or any subtle changes in the composition. This thesis addresses this outstanding issue in one of the chapters (chapter 4). Soon afterwards, Jin et al. [Jin95a] demonstrated that chemical substitution on the trivalent site could have an effect equivalent to a controlled anneal. They showed that a large magnetoresistance of 10^5 % at temperatures close to 140 K and in a magnetic field of 6 T could also be obtained in samples of bulk ceramic form by replacing 7 % of lanthanum by yttrium. Using the same 7 % yttrium substitution, Sun et al. [Sun95a] demonstrated magnetoresistance values of 2×10^4 % around 100 K with laser ablated as-grown thin films at 600 °C without a post deposition anneal.

For CMR effects in both bulk and thin film materials, the basic phenomena seem to be the same. The resistivity peaks near the Curie temperature, around which the largest magnetoresistance is obtained. Above the Curie temperature, the resistivity shows a thermally activated behavior [Xio97]. Below the Curie temperature, the resistivity decreases with decreasing temperature as the magnetic moment grows. A correlation between resistivity and magnetization has been established [Sun95a]. Magnetoresistance values are related to the pseudoperovskite cell size. A large pseudoperovskite cell size seems to lead a lower Curie temperature, which in turn leads to a high resistivity peak

accompanied by a large magnetoresistance effect. All reports of large magnetoresistance involve the preparation of the materials in such a way as to suppress its resistance peak temperature to below 150 K. The saturation magnetic field necessary to achieve a full CMR effect in the generic materials is large, usually of the order of several Tesla.

Materials Properties of CMR Materials

Manganite perovskite oxides were first systematically studied in the 1950s [Jon56, Jon50]. The parent compounds $\text{La}^{3+}\text{Mn}^{3+}\text{O}_3$ and $\text{Ca}^{2+}\text{Mn}^{4+}\text{O}_3$ both have a perovskite structure. $\text{La}^{3+}\text{Mn}^{3+}\text{O}_3$ is a layered antiferromagnet, while $\text{Ca}^{2+}\text{Mn}^{4+}\text{O}_3$ is an antiferromagnet with opposite spin orientations for nearest-neighbor Mn^{4+} spins [Wol55].

$\text{La}^{3+}\text{Mn}^{3+}\text{O}_3$ is an antiferromagnetic insulator. Its cell structure is shown in Fig 2.3 (a). A Jahn-Teller distortion lifts the double degeneracy of the E_g orbitals and defines the direction along which the Mn^{3+} moments order antiferromagnetically. A schematic of layered antiferromagnetic Mn^{3+} moment arrangement is shown in Fig.2.3 (b). From neutron diffraction studies [Wol55], Mn^{3+} moment must lie in the plane of Mn-O sheet, although the relative orientation of the moment with respect to the cell edge could not be determined from the powder diffraction data. Lecoer et al. [Lec97] recently concluded from their work on thin film $\text{La}_{0.7}\text{Sr}_{0.3}\text{MnO}_3$, that a magnetic easy axis may exist for the magnetic moments to align along the (110) direction of the pseudocubic perovskite cell, as shown in Fig. 2.3 (b). CaMnO_3 is also an antiferromagnetic insulator; Mn^{4+} moment aligned antiferromagnetically with a cubic symmetry [Wol55]. It has a Neel temperature of 120 K.

A continuous solid solution exists between these two end compounds whose structural, magnetic, and transport properties depend sensitively on doping level x . The magnetic phase diagram of $\text{La}_{1-x}\text{Ca}_x\text{MnO}_3$ [Sch95] (Fig.2.4) shows that the Curie

temperature peaks around $x \sim 0.3$. Around $x \sim 0.5$, the system exhibits a complex first-order ferromagnetic-antiferromagnetic transition accompanied by a metal-insulator transition [Kuw96]. Long range ordering of the dopant charge is believed to exist at this doping level and is responsible for the first-order phase transition. This phase diagram is also qualitatively true for $\text{La}_{1-x}\text{Ba}_x\text{MnO}_3$ and $\text{La}_{1-x}\text{Sr}_x\text{MnO}_3$. Pr- and Nd- based manganites, which show similar behavior, have also been studied. $\text{La}_{1-x}\text{MnO}_{3-\delta}$ self-doped system also exhibits ferromagnetic ordering with a maximum Curie temperature around 300 K [Man95].

The magnetic and transport properties of doped manganite perovskites show sensitive pressure dependence. Upon the application of hydrostatic pressure, the Curie temperature rises, the resistivity decreases and the effective amount of magnetoresistance decreases [Arn95]. Studies by numerous groups on pressure dependence have revealed a positive dT_c/dp (change in transition temperature per unit change in pressure) in various systems.

Doped manganite perovskites show a strong correlation between their magnetic state and structural properties. As we increase the doping level, x , a metallic and ferromagnetic state develops accompanied by a diminishing orthorhombic distortion; i.e., the difference between a_1 and a_2 disappears. Large changes in lattice parameter were observed when samples go through their ferromagnetic transition. Asamitsu et al. [Asa95] reported a first-order structural phase transition between the orthorhombic form (low temperature, ferromagnetic) and rhombohedral form (high temperature, paramagnetic) that can be triggered either by varying the temperature near the Curie point or by the application of magnetic field of the order of 1 Tesla for single crystal La_{1-x} .

$x\text{Sr}_x\text{MnO}_3$. Near the Curie temperature, a relatively small field could lead to phase transition.

New compounds exhibiting similar magnetic and transport behaviors are being rapidly discovered. Layered perovskite system $(\text{La}_{1-x}\text{Sr}_x)_{n+1}\text{Mn}_n\text{O}_{3n+1}$ shows a resistance change close to two orders of magnitude in a field of 7 Tesla for $n = 2$ compound at $x = 0.4$ near its Curie temperature of around 130 K [Mor96]. Large magnetoresistance was also observed in the Pyrochlore compound, Ti_2MnO_7 , having a Curie temperature around 150 K [Shi96, Sub96]. Majority carriers in this system are electrons in contrast to the doped perovskites, where the majority carriers are holes. Several interesting questions arise in the pyrochlore system such as how the ferromagnetism develops in this system and whether the mechanism leading to ferromagnetic and metallic states is double-exchange interaction alone. Ongoing research in these systems will answer the questions in the near future.

CMR Effect in Thin Films

Von Helmolt et al. [Von93] was the first to report a large, room-temperature magnetoresistance in $\text{La}_{0.7}\text{Ba}_{0.3}\text{MnO}_3$ epitaxial thin films made using pulsed laser deposition in off-axis geometry. This geometry reduces the number of particles formed on the film surface. They used stoichiometric ceramic targets, single crystal SrTiO_3 substrates, substrate temperature of 600 °C and a background pressure of oxygen of 300 mTorr. They reported that a higher substrate temperature resulted in polycrystalline films, not a commonly seen phenomenon. The Curie temperature increased to room temperature after annealing the films at 900 °C in air. A magnetoresistance of $1.5 \times 10^4\%$ was seen in a magnetic field of 7 Tesla. The magnetic moment was found to be only 90% of the bulk material in 2 Tesla field.

Soon after Helmolt, Jin et al. [Jin94] and McCormack et al. [McC94] reported the successful synthesis of epitaxial thin films of $\text{La}_{0.67}\text{Ca}_{0.33}\text{MnO}_3$ by pulsed laser deposition that exhibited a field-driven change in resistivity of three orders of magnitude in a field of 6 Tesla. They used a substrate temperature of 650-700 °C, oxygen background pressure of 100-300 mTorr and (100) LaAlO_3 substrate. A subsequent heat treatment in oxygen ambient produced the films with highest magnetoresistance. Xiong et al. [Xio95a] reported a large CMR effect in pulsed laser deposited $\text{Nd}_{0.7}\text{Sr}_{0.3}\text{MnO}_3$ thin films. Many more thin film systems have since been investigated.

Commonly used deposition techniques for perovskite oxides include laser ablation, reactive sputtering, co-evaporation, and CVD. Laser ablation is most widely used in laboratory environment for the deposition of oxides. It is by far the most straightforward deposition method for complex oxides because of the ease of obtaining stoichiometric transfer of materials from target to substrate. The major drawbacks are scalability and particulate generation. Reactive sputtering is very good for deposition of large area films; however, in case of complex oxides there may be a problem of nonstoichiometric transfer and resputtering at the substrate. This problem may not be as serious for manganites as it is in the case of high temperature superconducting cuprates such that one has to use off-axis sputtering for good enough stoichiometric transfer [Cho90, Sri95, Zen95]. Other growth techniques such as reactive molecular beam epitaxy, MOCVD, and sol-gel have also been applied successfully for the growth of epitaxial thin films of manganites [Ach95, Sny96, Bae96].

The substrates used in all these studies are either SrTiO_3 or LaAlO_3 perovskite single crystals. This is because a good lattice match to the manganites is required to observe CMR effect. There are some recent reports [Tra96] on the successful growth of

high quality epitaxial thin films on buffered silicon substrates, which might be interesting for technological reasons.

Structure-Property-Composition Correlation

The properties of manganite thin films are highly sensitive to post deposition heat treatment. This is probably due to the strong mutual dependence of magnetic state and the local lattice configuration, especially that of the Mn-O-Mn bond length and bond angle. Direct comparison of the data between thin film and bulk samples is difficult because of the large amount of residual uniaxial stress in thin films.

The effects of oxygen in manganite films have been a focus since the discovery of extraordinary magnetotransport in this kind of materials. There is no quantitative relation between the oxygen content and the magnetic and transport properties in thin films till date due to the difficulty in the determination and control of oxygen content. Substrate temperature, oxygen partial pressure, and deposition rate could have an effect on the oxygen content of the film severely [Jin94, Xio95a, Wei96]. Vacuum annealing can produce a deficiency in oxygen [Ju 95], while annealing in oxygen can produce excess in oxygen. All these indicate that oxygen content can be flexible in manganese oxides. In the early studies of CMR materials, a post deposition anneal in oxygen at high temperatures was critical for achieving large magnetoresistance [Von93, Jin94]. However, it was not clear whether the improvement was due to improvement in microstructure, increase in the oxygen content of the film or any subtle changes in the composition. Improvement in the crystallinity and grain growth enhances the properties of the oxide thin films [Mat90, Sin92]. Surprisingly, studies to discern these important effects are surprisingly missing in the literature

The first study to understand the effect of annealing was done by Prellier et al. [Pre99] In their study, they compared the properties of as-grown films with those of films annealed under argon and oxygen. They have obtained a phase diagram as a function of temperature and doping concentration for both as grown and oxygen annealed films. They observed an increase in the transition temperature of the films upon annealing in oxygen. There is no effect on the films upon annealing in argon. According to them, annealing the films in oxygen ambient increases the oxygen content of the films, which leads to an equal number of vacancies at both of the cation sites and hence to an increase of the Mn^{4+} content. The increase in Mn^{4+} content leads to an increased transition temperature, T_c and metal-insulator transition temperature, T_{MI} . Their studies do not discuss the effect of annealing on the magnetoresistance properties of the films. Surprisingly, they have found no differences in the properties of the films annealed in argon and oxygen. They concluded that effect of annealing (change in the transition temperature of the films) is from oxygen incorporation and not the thermal effect.

Since, many groups have studied the effect of annealing on the properties of CMR films. All their studies were concentrated on the effect of annealing in oxygen on their properties. In all the studies, there is an improvement in the transition temperature as well as MR ratio. None of these studies have considered the thermal effects. The next effort to discern the effects of temperature and oxygen content on the properties of CMR films was done by our group and Nam et al. [Nam01] independently. Nam et al. have adopted a similar study as us except that they have compared the properties of the films grown on two different substrates as well. They have (similar to us) found that the effect of annealing in oxygen and argon leads to different properties contrary to the observations made by Prellier et al. [Pre99] (above). XRD results of the films grown on both the

substrates indicate a decrease in Full Width at Half Maximum (FWHM) after annealing implying an enhancement in the crystallinity of the films. The (004) peaks of the films grown on both the substrates approach the bulk value, suggesting that post-annealing relieves the structural strain induced by the substrate-film lattice mismatches. There is a decrease in the resistances of the films after annealing in oxygen. They also observed an improvement in the MR ratio of the films. The MR curves of the films on both the substrates were virtually identical, although their temperature-dependent resistivity data are different, indicating that MR property has a different origin, probably related to the microstructural change on the surface.

Two effects driven by oxygen annealing at high temperatures can be expected. One is oxygen incorporation, which not only leads to the optimal doping level but also increases the strength of the Mn-O bond due to saturation of anion defect sites, as observed by a reduction of the Mn-O bond length (from XRD data). Accordingly, this may increase the orbital overlap and in turn enables electrons to hop easily. The other effect, the thermal effect, would relieve the structural strain induced by lattice mismatch and also create microstructural change. These two possible effects can be separated by annealing the film in an ambient other than oxygen (for example in argon) and compare the properties with a film annealed in oxygen. The (004) peak of the argon annealed film shifted very close to the bulk value. The interesting feature of the argon annealed film is that its insulator-to-metal transition temperature is virtually identical to that of the as grown film, while the oxygen annealed film exhibited a higher transition temperature. This indicates that the insulator-to-metal transition temperature is primarily dependent on the oxygen incorporation. However, there is a considerable improvement in the MR ratio of the film as compared to that of as grown films. The MR value is similar to that of the

oxygen annealed film (they claim, though there is a discrepancy in the values reported by them in their paper) implicating that the MR ratio is mainly associated with the microstructural change induced by the thermal effect.

To further ascertain their interpretation that the MR property is related to the microstructural change associated with annealing, they have done atomic force microscopy measurements on these films (Figure 2.5). They observed a remarkable improvement in the surface morphologies of the post-annealed films. The average grain sizes of the post-annealed films were about three times larger than as deposited films. The roughnesses of the post-annealed films are reduced considerably as well. As deposited films have a rough surface and small-sized grains probably hinting at the strain experienced by the film layer. Upon annealing, recrystallization process takes place enlarging the grain size and diminishing the surface roughness. This microstructural change is considered to be consistent with the enhancement of MR ratio and sharpness of resistance versus temperature plots in the post annealed films.

But from their study, there still remain certain aspects, which are not clear. A high temperature anneal in argon ambient may lead to a loss in oxygen from the films. There is no comment on the oxygen content of the film annealed in argon. In fact, they have observed a decrease in the lattice parameter after annealing in argon. This should indicate that annealing in argon should enhance the Mn-O bond strength. Detailed compositional analysis is needed before one can comment on the oxygen content of the films (rather than just from XRD results). Near the grain boundaries, the pairs of spins of Mn^{3+} and Mn^{4+} may not be parallel. As a result the electron transfer between pairs of Mn^{3+} and Mn^{4+} ions across the grain boundary is difficult and the resistance is high. Increase in the grain size of the films might lead to a decrease in the amount of grain boundaries in a

specified area. This should lead to a decrease in the resistance of the films. But their results show only a little decrease in the resistance of the argon-annealed films as compared to as deposited films and much higher than the resistance of oxygen annealed films. Hence the resistance of the films must be having a different origin. The enhancement in the MR ratio of the argon annealed films is much higher than that of oxygen annealed films. Indeed the improvement in the microstructure of the films leads to an enhancement in the MR ratio of the films. They do not have an explanation why would there be a discrepancy in the MR ratios of the films annealed in oxygen and argon if they both have undergone the same microstructural improvements. These aspects still need further explanation and more studies to understand them. We tried to answer these questions in our study (chapter 4).

Magnetic Properties

The saturation magnetic moment of $\text{La}_{1-x}\text{Ca}_x\text{MnO}_3$ peaks around $x = 0.3$ [Wol55]. As deposited films exhibit coercivities of 10-500 Oe depending on the type of material, growth condition, and operating conditions. The magnetization of most of the laser deposited films lie in the film plane; however, it is not clear if there is any preferential directions for the magnetic moment to align in plane. Studies of Optical Kerr contrast microscopy on as deposited $\text{La}_{0.67}\text{Sr}_{0.33}\text{MnO}_3$ thin films indicated a possible in-plane easy axis along the pseudocubic cell axis of the manganites [Lec97]. However, magnetic hysteresis loops of several samples have shown no significant differences when the field is aligned along the (100) or (110) direction of the pseudocubic axis. As grown thin films of $\text{La}_{1-x}\text{Ca}_x\text{MnO}_3$ exhibit a significant amount of line width broadening in the ferromagnetic resonance (FMR) spectrum suggesting the presence of magnetic

inhomogeneity [Lof95]. Annealing at high temperature reduced their FMR line width suggesting a decrease in magnetic inhomogeneity.

Mechanism of CMR – Possible Origins

Goodenough [Goo55] and Goodenough et al. [Goo61] proposed a qualitative theory for the magnetic interaction in the manganites based on a special type of covalent Mn-O-Mn bond, which he denotes as the semi covalent bond. For this type of bond, the distance between the ions is very important. For magnetic moments of ions sharing the oxygen ion, a small lattice constant would lead to antiparallel or negative exchange coupling, while a longer bond length would lead to a parallel or positive exchange coupling. For the doped manganite perovskite family of compounds, there is a weak magnetic exchange coupling between the Mn^{3+} ions, a negative interaction between the Mn^{4+} ions, and a strong positive interaction between Mn^{3+} and Mn^{4+} ions [Jon56]. The type and strength of magnetic exchange coupling between adjacent manganese ions in the Mn-O-Mn bond depends sensitively on the valency of Mn, or the doping level x of the compound.

One peculiar feature of the doped manganite perovskites is the close association of ferromagnetism with metallic conduction. Zener proposed the double exchange mechanism [Zen51] to explain this correlation. Doping of the trivalent rare-earth site by divalent ion cause a corresponding number of formerly triply charged Mn to become quadruply charged and the displacement of these holes (also called zener carriers) increases the conductivity. As already mentioned before there is a strong positive exchange coupling between Mn^{3+} and Mn^{4+} ions in Mn^{3+} -O- Mn^{4+} provides a mechanism for ferromagnetic ordering. For such a model, the transfer integral for one electron is given by $t_{ij} = b_{ij} \cos (\theta_{ij}/2)$, where θ_{ij} is the angle between the two ionic spins and b_{ij} is the

coupling constant [And55, DeG59]. In the environment of an extended lattice, this interplay between dopant level and magnetic ground state leads to the theoretical proposal of a canted or spiral ground state for the Mn spin, with θ_j determined by the doping level x [Ino95].

Double exchange provides a mechanism for the simultaneous onset of ferromagnetism and metallicity. However, calculations [Mil95] have shown that double exchange is insufficient to account for the large magnetoresistance observed in CMR compounds. Also it predicts an incorrect temperature and field dependence when compared with experiment. A strong electron-phonon interaction mediated by the Jahn-Teller coupling of the Mn^{3+} ions must be included. $3d^4$ Jahn-Teller distortion of Mn^{3+} is known to be strong. This Jahn-Teller distortion with energy of the order of 1 eV [Mil95], is the underlying driving force for tetragonal-to-orthorhombic transition for $x \leq 0.2$ and also cubic-tetragonal transition at 800 K in LaMnO_3 [Goo55]. "Dynamic Jahn-Teller" polaron model gives a more satisfactory explanation and is supported by recent structural [Rad95] and neutron diffraction studies. Above Curie temperature and for $x > 0.2$, slowly fluctuating local Jahn-Teller distortions localize the conduction-band electrons into polarons. The polaronic effect is turned off as temperature is decreased through T_c , leading to a metallic state. The competition between electron itinerancy and self-trapping is controlled by the ratio of the Jahn-Teller self-trapping energy E_{J-T} and an electron itinerancy energy which is parameterized by an effective hopping matrix element t_{eff} . Double exchange causes t_{eff} to be effected by the degree of magnetic order, and spin disorder leads to its reduction. When E_{J-T}/t_{eff} exceeds a critical value, the phonon effect dominates and polarons form, localizing the electrons causing the insulating state. Jaimie

et al. [Jai96] reported polaronic dominated conduction in these materials. Their transport measurements gave an evidence of the presence of Holstein polarons.

Pickett and Singh [Pic96] reported an explicit band calculation of the Mn d - O p hybridization using local spin density approximation. They concluded that the electronic structure for $\text{La}_{1-x}\text{Ca}_x\text{MnO}_3$ ($x = 1/3$) is very nearly half-metallic near the Fermi surface. They found a spin dependent hybridization. The O p bands and Mn d bands are non-overlapping and hybridize much more weakly for the minority channel as compared to the majority channel at the Fermi level. The Mn d site energy varies depending on the Ca/La local environment disorder, which can create incoherent minority states near E_F . This results in E_F lying below a mobility edge leading to non-conducting minority states. The half metallicity is a local effect that persists near flipped Mn spins (e.g., abrupt "domain walls"). The lack of Stoner continuum and the possibility of minority spin polarons in a half-metallic ferromagnet provide possibilities for transport anomalies and for a large magnetoresistance.

In case of CMR materials, the ferromagnetic transition broadens, the low-temperature saturation magnetic moment increases, and a large reduction of resistance occurs in an applied field of several Tesla. This strong field dependence of magnetic properties suggests the presence of magnetic inhomogeneity. Another theoretical model proposed predicts the presence of fluctuating magnetic clusters and their possible relation to magnetic excitations in the system [Zha96]. The effective magnetic moment saturates at a value of around $20 \mu_B$ in high fields suggesting a rather small ferromagnetic cluster consisting of only four or five Mn ions. There is also evidence that the density of such magnetic clusters may be correlated to the dopant concentration on the lanthanum site [Sun96a]. These magnetic clusters may be related to the Jahn-Teller distortion-based

magnetic polarons described before. In such a magnetically inhomogeneous system, CMR effect may be related to the spin-dependent transport between these ferromagnetic (and thus metallic) clusters, with the amount of intercluster conductivity determined by the relative alignment of the magnetic moment of the clusters. The large saturation field for CMR effect is an indication of the small size of such magnetic clusters.

The role of magnetic inhomogeneities has been discussed widely in the literature. Ju et al. [Ju 95] pointed out that magnetic domain walls might be important in determining the magnetoresistance based on their studies on polycrystalline $\text{La}_{0.67}\text{Ba}_{0.33}\text{MnO}_3$. Hwang et al. [Hwa96] suggested spin dependent tunneling to be responsible for intergranular transport in polycrystalline samples from their studies on bulk single crystal and polycrystalline $\text{La}_{2/3}\text{Sr}_{1/3}\text{MnO}_3$ samples. An additional low-field cusp observed in the magnetoresistance plots in the polycrystalline samples might have the origin in such a tunneling mechanism.

Practical Limitations of CMR Materials and Efforts to Overcome Them

The magnetoresistance of doped manganites is of unprecedented magnitude; however, these large resistance changes are achieved only in a strong field in the Tesla range, thus severely limiting their practical utility. Reducing the field scale and increasing the operating temperature has been the goal of a number of research groups worldwide. Magnetic oxide materials having a high degree of spin polarization are expected to exhibit enhanced spin-dependent transport phenomenon. Three different approaches have been reported in the literature.

One is to study the magnetotransport properties due to spin-dependent transport across grain boundaries, both natural and artificial [Gup96, Mat97]. The observation of pinning of magnetic domain walls at grain boundaries has led to the investigation of

magnetotransport studies in polycrystalline materials, as well as thin films grown on polycrystalline substrates. The possible effect of magnetic domain boundary pinning by polycrystalline grain boundaries was investigated by Gupta et al. [Gup96]. They observed an enhanced magnetoresistance in the low-temperature region compared to that observed for epitaxial thin films grown on single crystal substrates. Mathur et al. have grown $\text{La}_{0.7}\text{Sr}_{0.3}\text{MnO}_3$ and $\text{La}_{0.7}\text{Ca}_{0.3}\text{MnO}_3$ films by pulsed laser deposition on symmetrical bicrystal substrates consisting of two (001) SrTiO_3 crystals with a variety of misorientation angles [Mat97, Isa98, Eve98]. They have observed a qualitatively similar behavior to that of polycrystalline films with two low field hysteretic peaks at fields similar to the bulk coercive field.

Another approach exploits the naturally occurring two-dimensional structure in the layered derivative of the manganese perovskite compounds, where inter-plane transport exhibits low-field magnetoresistance [Kim96]. Such compounds consist of multilayers of metallic sheets separated by insulating material, thus possessing naturally occurring ferromagnetic/insulating/ferromagnetic junctions in the c -axis direction. Single crystal compound, $\text{La}_{2-2x}\text{Sr}_{1+2x}\text{Mn}_2\text{O}_7$ is the only example in this category till date. Large low-field MR has been observed in this compound for $x = 0.3$ [Kim96]. It can be viewed as consisting of a stack of ferromagnetic-metallic sheets of MnO_2 , separated by the $(\text{La}, \text{Sr})_2\text{O}_2$ rocksalt layers acting as non-magnetic barrier. This is similar to artificially fabricated thin film tunneling devices, where the tunnel junction provides a weak, field-sensitive link between two ferromagnetic layers. The transport in this two-dimensional material is very anisotropic. As in the case of perovskite manganites, a fairly large CMR effect is observed near the ferromagnetic transition, with a much larger MR in the c -axis direction because of the insulator-metal transition. The unique aspect of this material is

that very substantial MR remains even at temperatures far below the transition temperature. Kim et al. [Kim96] suggested that the transport across MnO_2 planes is spin-dependent tunneling. However, recent neutron diffraction studies suggest the dominant role of a more intrinsic effect [Per98]. The mechanism of transport in these materials is still under investigation.

The third approach involves spin-dependent tunneling MR across a ferromagnetic electrode/insulating barrier/ferromagnetic electrode tri-layer structure [Sun96b]. One example is the $\text{La}_{0.67}\text{Sr}_{0.33}\text{MnO}_3 - \text{SrTiO}_3 - \text{La}_{0.67}\text{Sr}_{0.33}\text{MnO}_3$ epitaxial trilayer junction, which gave the first demonstration of large MR in the manganites at low fields [Sun96b, Lu 96, Vir97]. They reported a resistance change of a factor of 2 with a switching field less than 200 Oe at 4.2 K. However; this large low-field magnetoresistance is observed only at low temperatures, usually below 100 K. The mechanism of spin-dependent transport process in this system is yet to be understood and is still under investigation.

Despite of the recent flurry of investigations in the field of colossal magnetoresistant (CMR) materials, there are still some outstanding issues, which need to be addressed. Some novel approaches yet remain to be explored. This thesis hopes to address some of these outstanding issues and also outlines our novel efforts to reduce the field scale necessary to produce CMR effect.

Pulsed Laser Deposition (PLD)

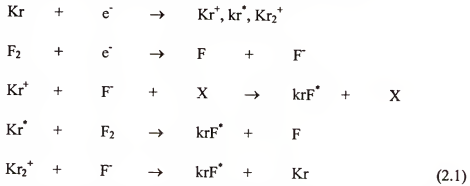
A variety of growth techniques such as evaporation, spray pyrolysis, sputtering, metal organic chemical vapor deposition (MOCVD), molecular beam epitaxy (MBE), metal organic molecular beam epitaxy (MOMBE), and PLD, are employed for the fabrication of thin films. PLD is recognized as one of the most convenient techniques for the fabrication of multicomponent oxide thin films and multilayered structures because it

is a conceptually and experimentally simple but highly versatile technique for them. PLD offers numerous advantages for the growth of thin films of oxides and other chemically complex materials, including congruent (stoichiometric) transfer of material, low contamination level, high deposition rate, non-equilibrium processing, growth from an energetic beam, reactive deposition, simplicity for the growth of multilayered structures, atomically sharp step coverage and thickness control [Low96, Sin98]. These advantages have made PLD one of the most popular methods to fabricate thin films for various applications.

PLD was first used more than three decades ago after the pulsed ruby laser was invented [Smi65]. However, PLD has been experimentally developed and widely applied for thin film growth as one of the most convenient and efficient techniques after it was shown that high quality high transition temperature (high- T_c) superconducting thin films could be synthesized in a low pressure oxygen ambient without any further post deposition processes [Dij87, Low96, Sin98]. This discovery has opened, invigorated, and enriched the growth fields of oxide-based ceramics and other complex material systems with a wide variety of properties [Low96]. The complex thin films grown by PLD with high quality include high- T_c superconductors [Sin98], dielectrics [Sri99], luminescent films [Cho97], diamond-like carbons [Chr94], hard coatings [Lee98], ferroelectrics [Chr94], compound semiconductors [Chr94], and colossal magnetoresistant thin films [Pie98a, b; Pie99a, b; Pie00, Pie01].

KrF is the most popular excimer (excited dimer) laser in laser research since it shows the highest gain among the electrically discharged pumped excimer lasers which are the gas lasers that emit powerful UV pulses lasting from 10 to 50 nanoseconds [Gre94, Low96]. The UV wavelengths have the highest absorption and lowest reflectivity

for most materials. The usual active medium is a mixture of gases of a rare gas (Kr, Ar, or Xe) and a halogen (F₂) which combine to form a short-lived rare-gas halide molecules through avalanche electric discharge excitation [Hec92]. Once the excimer is formed, it decays via spontaneous emission and collisional deactivation processes [Hec92]. KrF laser system typically produces 248 nm wavelength and consists of ~ 3.5 % Kr and ~ 0.1 % F with neon and or/helium as buffer gases to mediate energy transfer with total gas pressure of ~ 3.6 atm. Some important reactions for the KrF system are:



the asterisk (*) represents an electronically excited state of the species and X is a buffer gas (He, Ne) [Gre94].

PLD uses a high power pulsed laser as an energy source to induce the flash evaporation (or ablation) of a very small segment of a solid or liquid target [Bou99]. When a rotating target material is hit by an UV pulsed laser beam focused with 1 ~ 5 J/cm² energy density, several physical events occur: rapid heating and vaporization of the segment; increased absorption by the vapor until breakdown occurs to form a dense plasma (or plume); and absorption of the remainder of the laser pulse to heat and accelerate the plasma which contains various species such as neutral atoms, ions, molecules, and energetic electrons, in both excited and ground states [Low96]. The species undergo collisions in the highly dense region near the target surface (Knudsen layer, typically a few hundred micrometers thick) to create a highly directional energetic

plume perpendicular to the target surface with initial velocities greater than 10^6 cm/s [Low96]. If PLD is performed in a low oxygen pressure environment, oxide molecules are also formed in the expanding plume. In this case, the plume expansion is generally governed by the background gas pressure, which results in collisions between the expanding plume and the gas molecules [Low96, Sin98].

PLD shows several characteristics differentiating it from other thin film growth techniques due to its use of energetic pulsed UV laser. Firstly, under optimized condition, congruent transfer of the target material to thin film sets PLD apart from thermal evaporation or sputtering which are incongruent transfer methods [Low96]. Congruent transfer is the consequence of the vaporization of the entire segment of the target in less than a nanosecond into an energetic plume of material [Bou99].

Secondly, deposition is induced by energetic plasma, which contains ablated non-equilibrium species inside. The kinetic (typically, ≥ 52 eV for 100 atomic mass units) and internal excitation energies of ablated species in the plume can be used to assist film formation and to promote chemical reactions, both in gas phase and on the growing film surface [Low96]. This non-equilibrium processing enables PLD to grow high quality thin films at 50 – 100 °C lower temperatures than used in other thin film growth techniques [Sin90, Sin98]. Introduction of short wave-UV lamp inside the PLD chamber broadens the versatility of the non-equilibrium processing in many areas [Cra98, Sri99].

Thirdly, its capability for reactive deposition in ambient gases is attributed to not having to use electron beams or hot filaments. Energetic species in the plume react readily with gas molecules to form simple oxides, nitrides, or hydrides, which allows the growth of multicomponent ferroelectric, ferrite, and biocompatible oxide ceramics [Low96].

Fourthly, multilayered epitaxial heterostructures can be grown by PLD using a multitarget carousel for rapid target switch with a separate target for each layer. By choosing a low deposition rate ($\sim 0.1 \text{ \AA/pulse}$) with automatic controlling system, atomic layer step coverage and thickness control is possible in PLD [Low96].

Finally, the presence of particulates and spatial thickness and compositional variations are commonly observed in PLD films, which have limited their use for semiconductors and other electronic applications. A rotating vane velocity filter is reported as an effective remover of the particulates during deposition [low96]. Otherwise low energy deposition is the only solution [Sin98]. Laser beam rastering over a large area diameter target, as shown in Figure 2.5, deposited successfully over 150 mm diameter substrates with variations of $\pm 2.3 \%$ in thickness and $\pm 0.5 \%$ in composition [Gre95].

In order to understand the fundamental mechanisms of PLD and fabricate high quality thin films, several in situ diagnostic techniques such as mass spectrometry, high speed photography, optical absorption, and emission spectroscopy techniques have been developed in PLD [Sin98, Xu 95]. Mass spectrometry allows the analysis of the charged part of the plume, and both absorption and emission spectroscopy techniques provide complementary information together on the nature of the species present in the laser-induced plasma [Sin98]. Emission spectrometer depends on the presence of excited species, whereas absorption spectrometer is capable of inspecting cool species [Sin98]. The detailed information on the optical measurement techniques are published elsewhere [Bat94, Bro93, Geo94]. Information obtained from these techniques with time-resolved high speed photographs is used to investigate both the quantitative and qualitative analysis of the species in the laser-induced plasma, which can eventually lead to deposition of high quality thin films.

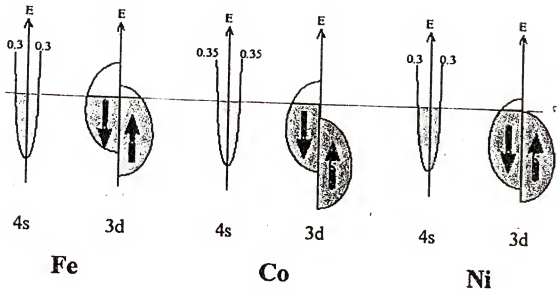


Figure 2.1: Schematic of s- and d- bands attributed to conduction with relative population and energy with respect to fermi energy [Mat91]

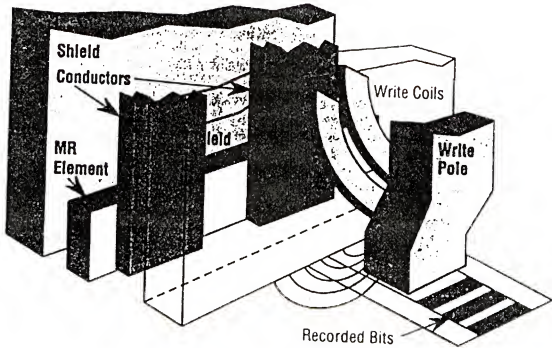


Figure 2.2: Geometry of a dual gap magnetoresistive (MR) recording head. The top shield of the read head element also serves as the bottom pole of the write element [Bru96]

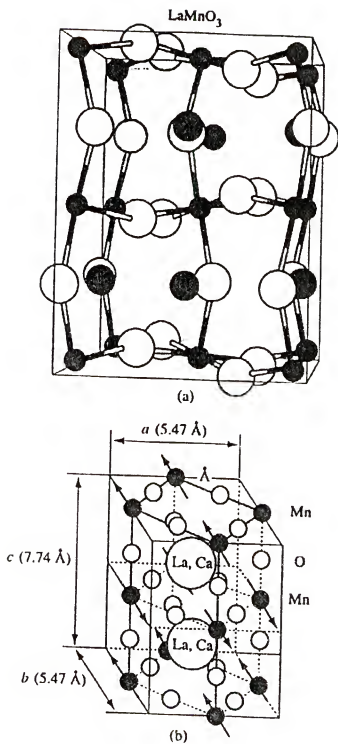


Figure 2.3: Lattice structure and magnetic moments in LaMnO_3 (a) Sketch of the Jahn-Teller distorted LaMnO_3 lattice structure [Pic96], (b) alignment of magnetic moment of Mn^{3+} ions based on Wollan's neutron study [Cha93]

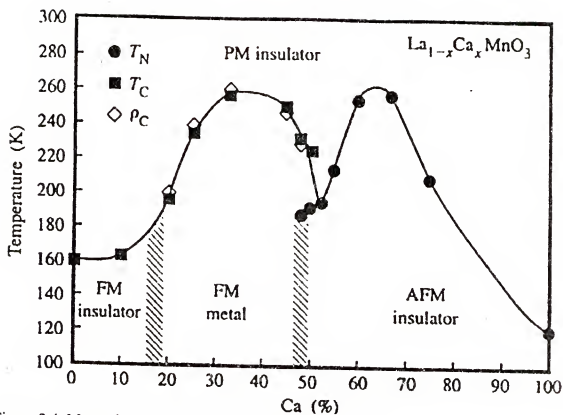
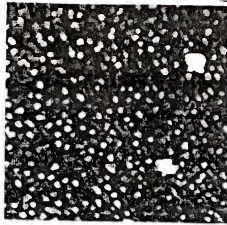


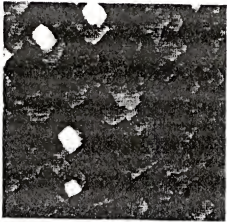
Figure 2.4: Magnetic phase diagram of $\text{La}_{1-x}\text{Ca}_x\text{MnO}_3$ [Sch95]



(a)



(b)



(c)

Figure 2.5: AFM surface images of (a) as-grown, (b) oxygen annealed and (c) argon annealed $\text{La}_{0.7}\text{Ca}_{0.3}\text{MnO}_3$ films grown on LaAlO_3 [Nam01]

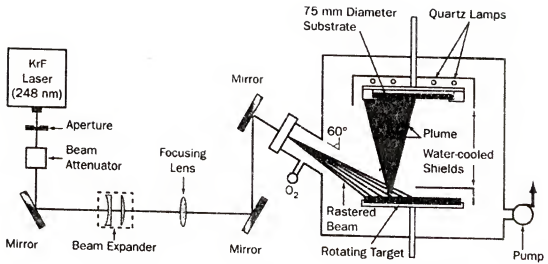


Figure 2.6: Schematic illustration of PLD experimental setup for large area processing by rastering of a large diameter target with rastered laser beam [Bou99]

CHAPTER 3 EXPERIMENTAL APPROACH

Target Preparation

Bulk PLD targets used in this research were prepared by a ceramic method. The required quantities of respective oxides and carbonates (in case of lanthanum calcium manganese oxide: La_2O_3 , CaCO_3 and MnCO_3) were mixed, cold pressed into a 1-inch diameter pellet. The pellet was then sintered at 1400 °C for 24 hours in air. After the initial firing, the pellet was reground, repressed and resintered to produce a dense compact solid target. With this technique various targets of required stoichiometric composition can be synthesized. The chemical composition and homogeneity of the final target was examined using powder x-ray diffraction, Auger electron spectroscopy (AES) and energy dispersive x-ray spectrometer (EDS) on the outer as well as on the fractures surfaces of the sintered targets.

Substrate Materials

As has been discussed earlier in the literature review (chapter 2), for manganite films to exhibit good CMR properties, good lattice match with the substrate is necessary. The substrate used in this research is (100) single crystal, lanthanum aluminum oxide (LaAlO_3).

CMR Film Fabrication

Fabrication of various colossal magnetoresistant thin films was carried out in a vacuum chamber where a rotating bulk manganite target was ablated by an incident KrF

pulsed excimer laser with a wavelength of 248 nm. The substrates were mounted on the faceplate of a substrate heater placed parallel to the target surface. A schematic illustration of the PLD system used for fabricating manganite thin films is shown in Figure 3.1. The processing conditions used to fabricate the manganite films are shown in Table 3.1. Temperature of the substrates was controlled and monitored using a programmable temperature controller and a pyrometer. The fabrication of superlattices was accomplished with the help of a computer operated multitarget carousel. The deposition rates in this case were calibrated against the number of pulses.

Table 3.1. Processing conditions for manganite thin films.

Energy density (J/cm ²)	Repetition rate (Hz)	Oxygen Pressure (mTorr)	Distance from target to substrate (cm)	Substrate temperature (°C)
1.0 – 2.0	5	200 - 400	5 - 9	700 - 850

Characterization

Microstructural analysis of the colossal magnetoresistant thin films was carried out using X-ray diffraction (XRD), atomic force microscopy (AFM), Rutherford back scattering spectrometry (RBS) and transmission electron microscopy (TEM). Surface chemistry and chemical composition of the films were analyzed using X-ray photoelectron spectroscopy (XPS) and Rutherford back scattering spectrometry (RBS) respectively. RBS analysis was done at Universites Paris VII. Film thicknesses were estimated using VASE, TENCOR Alpha-step 500 surface profilometer having a mechanical stylus, and TEM cross-sectional views of the films. Magnetic and magnetotransport measurements were made using the superconducting quantum

interference device magnetometer (SQUID). The TEM analysis was conducted at the Physical Analysis Laboratory of Motorola, Inc.

X-Ray Diffraction (XRD)

A Philips APD 3720 X-ray diffractometer was used to analyze structural changes, crystallinity of the films and epitaxial growth of the films on the substrate. A collimated beam of x-rays was incident on a specimen and was diffracted by the crystalline phases in the specimen according to Bragg's Law ($\lambda = 2d \cdot \sin\theta$, where d is the spacing between atomic planes in the crystalline phase). The intensity of the diffracted x-rays was measured as a function of the diffraction angle 2θ and the specimen's orientation. The tube generator was operated at 40 KV and 20 mA at a wavelength (λ) of 1.54 \AA Cu- K_α radiation. X-ray step scan was performed in the range of 10° to 140° with a step size of 0.05° and 0.25 second integration time per step. Receiving slit of 0.2 was used.

Atomic Force Microscopy (AFM)

AFM was used to get information on the surface roughness and other morphological details of the CMR films. The scan area was in the range of 10×10 to $40 \times 40 \text{ }\mu\text{m}^2$ and contact mode was used to scan the areas. AFM employs very sharply etched silicon nitride tip attached to a cantilever for contact mode (or silicon tip for tapping mode). As the tip is brought close to the sample surface, it experiences a weak Van der Waals attractive force. The tip is drawn closer causing the electron clouds of the tip and sample to overlap which induces a repulsive electrostatic force. This force goes to zero as the distance between the atoms reach a few angstroms. AFM is in the contact mode when the Van der Waals force becomes repulsive, while it is in tapping mode when the force is in the attractive regime.

In contact mode, AFM is operated by scanning across the sample surface with the tip attached to the end of the cantilever. The sample surface is monitored by measuring changes in deflection of the cantilever with a split photodiode detector. A feedback loop maintains a constant deflection between the cantilever and the sample by vertically moving the scanner at each (x,y) data point to maintain a set point deflection. By maintaining a constant deflection, the force between the tip and the sample also remains constant. The distance that the scanner moves vertically at each (x, y) data point is stored by the computer to form the topographic image of the sample surface as well as other quantitative topographic data such as roughness, grain size, step height, hardness, friction, and wear strengths.

Transmission Electron Microscopy (TEM)

A JEOL 2010 FX TEM was used to investigate the crystal structure of CMR films on LaAlO_3 substrate. The TEM was operated at 200 KV. Low magnification bright field images were taken to get thickness of the films. Selected area electron diffraction patterns were taken to get information of lattice matching in perpendicular as well as along the substrate surface. Multibeam bright-field electron diffraction contrast images were obtained to determine the detailed atomic structure of films as well as the interface.

Samples for TEM studies were prepared by mechanical grinding, polishing, dimpling (using a Gatan dimpler), followed by Ar^+ ion milling. The ion milling was carried out using the precision ion polishing system (PIPS). The guns were oriented at an angle of 8° with respect to the surface and a voltage of 4.5 KeV was used during milling. Cross-sectional slices were obtained by cutting the CMR/ LaAlO_3 along the [100] or [010] directions (using pseudocubic indexing) and then gluing face to face using metallic bond, followed by curing for an hour at 100 °C.

Variable Angle Spectroscopic Ellipsometry (VASE)

J. A. Woollam VASE was used to measure the thicknesses and optical constants of CMR films and substrates. Ellipsometry measures the change in polarized state of light reflected from the surface (or transmitted through) a sample. An incident beam of light with a known polarization state is reflected from the surface (or interface). The change in the polarization state of the incident light due to the sample is measured. The measured values are expressed as azimuth (ψ_r) and the phase difference (Δ). These values are related to the ratio of Fresnel reflection coefficients, R_p and R_s for p- and s-polarized light, respectively, as defined as, $R_p/R_s = \tan(\psi_r)\exp(i\Delta)$. The calculation of the two parameters based on physical models gives information on film thickness and optical properties such as extinction coefficient (k) and refractive index (n) of the film and/or substrate.

X-ray Photoelectron Spectroscopy (XPS)

The chemical composition and atoms bonding of CMR films were investigated using x-ray photoelectron spectroscopy (XPS, Perkin Elmer 5100, Mg K_{α} radiation, take off angle 45°). In this technique, monoenergetic soft x-rays bombard a sample material, causing electrons to be ejected. Identification of the elements present in the sample can be made directly from the kinetic energies of these ejected photoelectrons. On a finer scale it is also possible to identify the chemical state of the elements present from small variations in the determined kinetic energies. The relative concentrations of elements can be determined from the measured photoelectron intensities. For a solid, XPS probes 2-20 atomic layers deep, depending on the material, the energy of the photoelectron concerned, and the angle (with respect to the surface) of the measurement.

Rutherford Back Scattering Spectrometry (RBS)

Rutherford back scattering spectrometry was used to analyze the crystallinity and quantitative depth profiling of the CMR films. In this technique, a monoenergetic beam of high energy particles, typically helium, with an energy of a few MeV bombards a sample target. A fraction of the incident atoms scatter backwards from heavier atoms in the near-surface region of the target material, and are detected usually with a solid state detector that measures their energy. The energy of a backscattered particle is related to the depth and mass of the target atom, while the number of backscattered particles detected from any given element is proportional to the concentration. This relationship is used to generate a quantitative depth profile of the upper 1-2 μm of the sample.

Alignment of the ion beam with the crystallographic axes of a sample permits crystal damage and lattice locations of impurities to be quantitatively measured and depth profiled. RBS measurements were used to analyze the effects of various post deposition heat treatments in CMR films.

SQUID Magnetization Measurements

SQUID (Superconducting Quantum Interference Device) is a superconducting loop with one or two Josephson junctions in the loop's current path. A Josephson junction is a narrow physical gap or a highly resistive area. Because of the quantized states of the superconducting ring, SQUIDs are able to resolve changes in external fields ranging from small to large fields. The SQUID also exhibits excellent non-linear behavior associated with the Josephson junctions and works extremely well as a very sensitive current-to-voltage converter. Thus, the SQUID does not directly detect the magnetic field from the sample. In the commercial rf-SQUID system used in this study, the sample was moved through a series of superconducting detection coils arranged as a

second order gradiometer (see Figure 3.2). The sample moving through such arranged coils induces a current, which is inductively coupled to the SQUID sensor. The output voltage is proportional to the current flowing in the SQUID input coil [Van81].

The SQUID magnetometer is one of the most sensitive methods used to measure magnetization. The commercial rf-SQUID (Quantum Design MPMS-5S) has a range of 10^{-8} emu to 2 emu. Typically CMR materials (when in the ferromagnetic regime) possess magnetization values on the order of 10^2 to 10^3 emu/cm³. Theoretically, the SQUID magnetometer can detect a ferromagnetic particle with a diameter on the order of 2 μ m. Such theoretical limits are unattainable because of noise from electronics and background magnetic response (such as diamagnetic contributions from the sample holder and LaAlO₃ substrate).

Magnetization measurements

For measurements, the sample is placed in a plastic tube container (much like a drinking straw) and is secured by the straw's elasticity. Although the plastic straw may encompass magnetic contamination, as long as the sample holder is uniform along the length of the scan distance, it will induce no signal. The background signal ($\sim 10^{-8}$ emu at low fields < 200 Oe) is usually more than two orders of magnitude lower than the signal from the CMR films considered. Due to anisotropic effects, the plane of the substrate is aligned parallel to the applied field direction. During measurement, the magnet is operated in the 'non-overshoot mode' where the set field is approached slowly and not exceeded. This precaution is important in case of 'soft' magnetic materials with small coercive fields. We have used this precautionary measure in CMR materials also because they exhibit a wide range of coercivities depending on their thickness as well as the

processing conditions. In addition, before measurement, the sample area is degaussed to remove any remnant magnetization, and the magnet is reset to remove any persistent current in the superconducting magnet. The operation of the superconducting magnet is by the persistent mode. In this mode, the persistent current in the superconducting Nb alloy wires of the magnet provides the field. Field changes are made by applying more or less current through a persistent switch. A persistent switch works by locally heating an area on the superconducting magnet. This action would result in changing the superconducting properties to normal. Although this operation is time consuming, it is much more sensitive since noise from a power supply is eliminated during measurement.

Before recording data, a nominal field is applied and a sweep of full length (16 cm) is done to center the sample. During measurement, the sample is swept at least three times (4 cm scan length) allowing three measurements of the SQUID response. For smaller signals ($< 10^{-5}$ emu), the sample is swept five times. During each measurement, the computer fits a response by various iteration schemes and records the fit (emu value), deviation, temperature, time, and applied field, etc. Once the experiment is finished, the data is extracted and fitted, which requires subtracting diamagnetic contributions from the straw and the LaAlO_3 substrate. Although the LaAlO_3 substrate constitutes the vast majority of the sample, the diamagnetic response is orders of magnitude smaller than the ferromagnetic response, especially at low fields. For most of the raw data in this study, hysteresis loops consist of a negative sloped component. This linear response can be fitted to extract $\chi_{\text{dia}} (< 0)$, which is used to extract the ferromagnetic component.

$$M_{\text{measured}}(H) = M_{\text{ferro}}(H) + M_{\text{dia}}(H) \quad (3.1)$$

$$M_{\text{ferro}}(H) = M_{\text{measured}}(H) - \chi_{\text{dia}} \times H \quad (3.2)$$

For low field measurements ($H < 100$ Oe), the sample area retaining magnetization complicates the matter. The specification for commercial SQUID magnetometer used in this research states a remnant field of around 20 Oe. This figure of merit depends on the history of the magnetic measurement itself. By calibration using a paramagnetic palladium sample, zero field offsets of few oersteds was found. This shouldn't be a problem in case of CMR materials as measurements are made at fields of the order of at least 10,000 Oe.

In any experimental measurement, one needs to specify the sources of error and the possible consequence on the measurement. An error in SQUID magnetometer measurement is determined from the fit of the SQUID response. This error scales with the magnitude of the signal, and for the smallest signals considered, the deviation is always an order of magnitude less. User errors such as, an imperfect alignment of the sample parallel to the applied field are minute. Such errors would correspond to asymmetry in the hysteresis loops. When coercive field values are reported, an average value between left and right is quoted. Due to the nature of plotting hysteresis loops, error bars were not displayed to avoid cluttering a large ensemble of data points. The error in the applied field and the temperature is minimal, as they are set by commercially available controllers. For each temperature setting, the sample is held at the temperature for up to five minutes to ensure that the sample temperature is equalized to the temperature measured. For each field, the sample is held for at least ten seconds after the superconducting magnet is charged.

Magnetotransport measurements

CMR films undergo an insulator to metal transition as the temperature is reduced from room temperature. The temperature at which they undergo this transition is referred

to as the transition temperature. CMR effect is observed in the vicinity of the transition temperature. Hence, the variation of resistance with temperature is a very important measurement in this study.

The temperature dependence of resistance of the films was examined in zero and applied fields using a four-probe technique. In this geometry, two leads were used to inject and collect current and two leads were used to sense the potential difference. The temperature controls and field controls are part of the commercial SQUID magnetometer, which allows the user external control of its functions. The polarity of the current was alternated at least three times. This alternation eliminates any offsets in contact resistances and minimizes thermal conductivity effects [Cab97]. While making the measurements, both the transport current and applied field were in the film plane. The magnetoresistance (MR) ratio $\Delta R/R(H)$ was calculated using the formula:

$$\text{MR ratio (in \%)} = \Delta R/R(H) \times 100 = [(R(0) - R(H))/R(H)] \times 100 \quad (3.3)$$

Where $R(0)$ and $R(H)$ are resistances in zero and applied fields

Again like the magnetization measurement, more than one measurement was performed at a specific temperature and applied field. Special care as described above was used to minimize noise and fluctuations in the measurement. Commercially available controllers are used to control the temperature and applied field. Temperature was usually set to one-thousandths of a Kelvin, and like magnetization measurements, the system was placed in idle for nominal periods to equilibrate the temperature and field. Sensitivity is an indirect function of the injected current since the greater the current, the greater the read voltage drop. To control cryogenic temperatures, there is a limit for current injected as the resistive heating load renders temperature control impossible. These limitations

restrict injected currents on the order of a fraction of a milliamperere, which gives a voltage signal on the order of hundreds of microvolts. Commercially available voltmeters are well suited to measure such levels.

Further, if there are any variations or any specific experimental procedure, they will be discussed along with the data in the respective chapters.

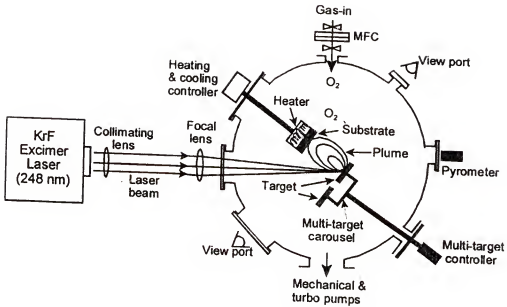


Figure 3.1: Schematic illustration of 248 nm KrF excimer PLD system equipped with a multi-target carousel and its controller, ambient gas supplier, and programmable heating and cooling controller for fabricating CMR films

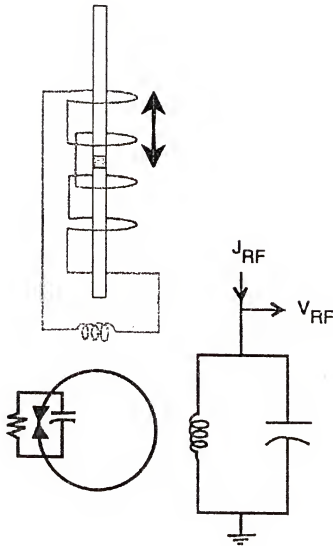


Figure 3.2: Schematic of SQUID magnetometer detection and electronics. Note that the sample is usually placed in a plastic sample holder, which is moved up and down along the coils to induce current in the circuit. The sample is centered in the middle of the coil by fully sweeping along the sample traverse range. During measurement, usually three sweeps are made for averaging purposes and with a scan length of 4 cm. Along the scan, 32 separate measurements are made, which are fitted to a signal of certain emu

CHAPTER 4

EFFECTS OF POST DEPOSITION HEAT TREATMENT

Overview

The properties of CMR films depend on the deposition parameters. Several researchers have studied the effect of various process parameters on the properties of CMR films. CMR films are extremely sensitive to post deposition heat treatments. A post deposition heat treatment leads to various effects like improvement in crystallinity, changes in composition of the films (for e.g.: in oxide films, loss of oxygen) depending on the temperature of anneal as well as ambient. In the early studies of CMR materials, a post deposition anneal in oxygen at high temperatures was critical for achieving large magnetoresistance [Von93, Jin94]. However, it was not known whether the improvement by the post annealing was due to grain refinement through grain growth and enhancement in the crystallinity of the films or due to oxygen incorporation or any changes which may be associated with the composition of the film. It is known that improvement in the crystallinity and grain growth, enhance the properties of the oxide thin films [Mat90, Sin92].

The effects of oxygen content in manganite films have been a focus since the discovery of extraordinary magnetotransport in CMR materials. There has not been a quantitative relation between the oxygen content and the magnetic and transport properties in thin films till date due to the difficulty in the determination and control of oxygen content. Substrate temperature, oxygen partial pressure during film growth, and

deposition rate could have an important effect on the oxygen content of the film [Jin94, Xio95b, Wei96]. Vacuum annealing can produce a deficiency in the oxygen content [Ju95] while excess oxygen can be incorporated into the films by annealing in oxygen [Mit96, Pre99]. All these indicate that oxygen content can be variable in manganese oxides. This is especially true for thin films due to the nature of their growth, which is performed at elevated temperatures and reduced oxygen pressure.

In this chapter, results of systematic post deposition heat treatments performed to discern the various effects discussed above are reported. This study would help in arriving at a better understanding of effects of annealing on the properties of lanthanum calcium manganite thin films. The CMR system chosen for the study is $\text{La}_{0.7}\text{Ca}_{0.3}\text{MnO}_3$, which is one of the most studied systems and is well optimized in our lab.

Experimental Details

A bulk $\text{La}_{0.7}\text{Ca}_{0.3}\text{MnO}_3$ (LCMO) target was prepared by ceramic method as described in chapter 3. Six LCMO films with a thickness of $\sim 1500 \text{ \AA}$ were grown *in situ* on (100) LaAlO_3 substrates from this target using a pulsed laser ablation system. To eliminate other external effects, all the substrates were placed side by side on sample holder. A detailed description of the deposition system is already mentioned in chapter 3. A substrate temperature of 700°C and oxygen pressure of 250 mTorr was used during the deposition of the films. Following the deposition, the films were cooled down to room temperature at a rate of $10^\circ\text{C}/\text{min}$ in 400 Torr of oxygen. After the initial characterization to check the identical properties, the films were subjected to the following post deposition anneals – (i) annealing in oxygen at 900°C for 4 hrs, (ii) annealing in argon at 900°C for 4 hrs, (iii) annealing in oxygen at 500°C for 12 hrs, (iv)

annealing in argon at 500 °C for 12 hrs and (v) annealing in vacuum at 850 °C for half-an-hour. The deposited films were characterized using x-ray diffraction (XRD), Rutherford back scattering spectrometry (RBS), x-ray photoelectron spectroscopy (XPS) and SQUID magnetometer (for transport and magnetic measurements).

Results and Discussion

Structural and Chemical Characterization

XRD patterns of the films subjected to various anneals are shown in Figure 4.1. From the figure it is clear that all the films have single phase with (00 l) peaks with $l = 1$ and 2. The presence of only sharp (00 l) peaks indicates the highly textured growth of all the films on (100) LaAlO₃ substrate. The lattice parameters for the films with no anneal (i.e. as deposited), 900 °C oxygen anneal and 900 °C argon anneal were found to be 3.86, 3.83, and 3.84 Å respectively. XRD patterns of 500 °C oxygen and argon annealed films were similar to those of as-deposited films. The films annealed in oxygen and argon at high temperature (900 °C) show a decrease in the full width at half maximum (0.1°) compared to the as-deposited film (0.25°) indicating these films are more crystalline.

RBS results obtained from these films are shown in Figure 4.2. As deposited films and 500 °C Ar and oxygen annealed films show poor crystallinity (30 % channeling yield in the film compared to 11 – 12 % in the substrate). The Vacuum annealed film showed much worse crystallinity (65 % channeling in the film compared to 20 % in the substrate). On the other hand, films annealed at 900 °C (oxygen and argon) show excellent crystallinity (7 % and 6 % channeling in the film compared to 7.5 and 8 % in the substrate, respectively). RBS results reiterate the observations made from XRD measurements that a high temperature post annealing helps significantly in improving the

crystallinity of CMR films and that the improvement in crystallinity is almost independent of the gas ambient.

RBS spectra were simulated [Doo86] to obtain the compositional differences between the films after the post deposition heat treatments. The observations are as shown in Table 4.1. It was found that that films annealed at 900 °C have higher and more uniformly distributed oxygen compared to as deposited and 500 °C annealed films. All the films exhibit stoichiometric oxygen content near the surface but as one moves away from the surface towards the interface, as deposited and 500 °C annealed films have lower oxygen contents. Films annealed at 900 °C exhibit stoichiometric oxygen contents through out the film thickness. This indicates that annealing at a high enough temperature produces a highly crystalline film with uniform oxygen content.

Table 4.1. Compositions of the LCMO films subjected to various post deposition heat treatments measured using RBS

Ambient	Annealing Temperature (°C)	Annealing Time (hours)	Composition	I-M transition temperature (K)	MR ratio (%)
as deposited	no anneal	none	$\text{La}_{0.67}\text{Ca}_{0.31}\text{Mn}_{1.02}\text{O}_{2.8}$	260	190
oxygen	900	4	$\text{La}_{0.64}\text{Ca}_{0.31}\text{Mn}_{1.05}\text{O}_3$	290	225
argon	900	4	$\text{La}_{0.62}\text{Ca}_{0.31}\text{Mn}_{1.05}\text{O}_3$	270	525
oxygen	500	12	$\text{La}_{0.62}\text{Ca}_{0.37}\text{Mn}_{1.01}\text{O}_{2.5}$	260	190
argon	500	12	$\text{La}_{0.65}\text{Ca}_{0.32}\text{Mn}_{1.03}\text{O}_{2.8}$	260	200

Another important observation made from the RBS analysis is that all these films have different lanthanum deficiency. We know that deficiency on the lanthanum site leads to self-doping effects and hence influences the magnetoresistance behavior of the

film [Man95]. As deposited, 900 °C argon and oxygen annealed, 500 °C argon and oxygen annealed films show 0.67, 0.64, 0.62, 0.62 and 0.65 lanthanum contents respectively. These have implications on the magnetoresistance of the films, which will be discussed later in the chapter.

The chemical composition and atoms bonding were investigated by x-ray photoelectron spectroscopy. The XPS spectra of the Mn 2p region acquired from as deposited and high temperature (900 °C) annealed samples are displayed in Figure 4.3. While the Mn 2p spectra of the as deposited and Ar annealed samples are very similar, that of the O₂ annealed samples exhibit some subtle differences. The satellites of the Mn 2p_{3/2} and 2p_{1/2} main lines, a feature only observed for MnO type compounds [Lan96] almost disappeared. Also the ratio of the peak intensities changed, a trend seen when MnO was annealed under vacuum and Mn evolved to higher oxidation states such as those found in Mn₂O₃ or Mn₃O₄ type compounds [Lan96].

The O 1s spectra (see Figure 4.4) are also different. The shoulder located at higher binding energy and suggested to be associated with some disorder in Mn-O compounds [Par99] was reduced in the annealed samples, more so for the O₂ anneal case. This sample also exhibits another shoulder towards lower binding energy, which might indicate some higher oxidation states. From these XPS data, one can conclude that the high temperature anneals improved the crystalline structure of the samples, as already shown by XRD and RBS data. The O₂ anneal also increased the oxidation state of Mn and resulted in the complete elimination of the MnO fraction, which might explain the improvement of CMR properties especially the transition temperature. There is little difference between the Mn 2p spectra of as deposited and Ar annealed films. Both the

films have shown similar transition temperatures. This may suggest that transition temperature might be related to the MnO content in the films. However, the magnetoresistance has a different origin, which will be discussed later in the chapter.

Magnetoresistance Behavior

The variation of electrical resistance in zero and applied field (5 T) as a function of temperature for the films subjected to various anneals are shown in Figure 4.5. All the films were grown under identical conditions so that film thickness, oxygen content and other external effects (before anneals) were identical. It is important to keep these parameters identical in order to reveal the effects of anneal upon magnetotransport properties. According to the variation of resistance shown in Figure 4.5, all films (except the vacuum annealed one) have similar qualitative magnetotransport behavior. That is, all the films undergo an insulator-to-metal (I-M) transition as the temperature is lowered down and the resistance of all the films is suppressed significantly with the application of magnetic field. The suppression in film resistance in each case is maximum near the resistivity peak in zero field as reported frequently in several manganite systems [Sea70, Von93, Jin94]. The MR ratios (calculated using the formula described in chapter 3) of the films were calculated using the data in Figure 4.5 and plotted in Figure 4.6 as a function of temperature at 5T.

The as-deposited films show an I-M transition at 260 K and a MR ratio of 190 % in 5 T. The films subjected to 500 °C oxygen and 500 °C argon anneals show little change in I-M transition and MR ratio. The films subjected to 900 °C oxygen anneal show an improvement of ~ 30 K in transition temperature and an enhancement of ~ 35 % in the MR ratio. The films subjected to 900 °C argon anneal show a slight increase in the

transition temperature (~ 10 K) but quite a significant enhancement in the MR ratio. The MR ratio improved by a factor of almost two and half (525% in Ar annealed films vs 190 % in as-deposited films). The films subjected to vacuum anneal have shown deteriorated properties remaining insulating down to 10 K.

The changes in structural and magnetoresistive properties brought about by different annealing processes can be explained as follows. The annealing of the films at high temperatures in oxygen and argon can lead to – (a) incorporation or removal of oxygen from the film depending on the ambient, (b) recrystallization and grain growth. Each of these effects has a significant influence on the properties of the film. Ju et al. [Ju 95] established a linear decrease of I-M transition with oxygen deficiency for the bulk $\text{La}_{0.67}\text{Ba}_{0.33}\text{MnO}_{3-\delta}$. Films annealed at 500 °C under oxygen and argon show little effect on the transition temperature or MR ratio of the films. This temperature is therefore not high enough for either oxygen incorporation/removal or to cause recrystallization and grain growth to improve the film crystallinity. No observable differences were found from the XRD patterns of these films as compared to the as-deposited films.

Films annealed in oxygen at 900 °C show an increase in the transition temperature from 260 to 290 K. The resistance of the films are also low as compared to as deposited ones. Both of these effects (improvement in transition temperature and decrease in resistance) are believed to result primarily from an increase in the oxygen content of these films as revealed from XRD and RBS analysis experiments. The ferromagnetic transition is strongly determined by the number of Mn^{4+} ions. The mixed $\text{Mn}^{3+}/\text{Mn}^{4+}$ valence gives rise to both ferromagnetism and metallic behavior in LCMO films, and is responsible for the occurrence of colossal magnetoresistance [Zen51]. As oxygen is

incorporated into the film, two distinct reactions occur: contraction of the lattice, as evidenced by x-ray diffraction; and gain in the O^{2-} ions. Gain of oxygen ions should lead to changes in magnetotransport similar to those resulting from the application of external pressure. Under applied pressure the lattice contracts while transition temperature (T_c) increases and resistance decreases [Hwa95, Mor95]. These results can be explained by an enhancement in the Mn-Mn electron transfer probability as the average lattice spacing is decreased. An increase in the transfer probability should lead to an enhanced ferromagnetic correlation and increased carrier mobility between adjacent Mn ions. This leads to a higher T_c and lower resistance. The second effect relating to oxygen arises from the requirement of charge neutrality within each unit cell. The chemical formula for LCMO can be written as $La_{1-x}^{3+}Ca_x^{2+}Mn_{1-x+2\delta}^{3+}Mn_{x-2\delta}^{4+}O_{3-\delta}^{2-}$. Therefore, each oxygen incorporated into LCMO should lead to a conversion of Mn^{3+} ions to two Mn^{4+} ions. The carriers in LCMO are holes whose concentration is proportional to the Mn^{4+} concentration [Uru95]. Therefore, the incorporation of oxygen should increase Mn^{4+} concentration, which leads to an increase in the carrier concentration and hence decrease in the resistance.

The high temperature oxygen annealed films have also shown an increase in the magnetoresistance ratio. The improvement in the magnetoresistance ratio of the films seems to result more likely from an improvement in the microstructure of the films rather than from the enhancement in oxygen content. As already mentioned before, annealing causes recrystallization process producing grain refinement and enlargement, which might lead to an improvement in the properties of the films. The correlation between the improvement in film microstructure and magnetoresistance ratio is established further

more strongly by results obtained from annealing the films at elevated temperature in an ambient other than oxygen such as argon. According to our results, films subjected to argon anneal at 900 °C show marginal increase in the transition temperature. The resistance of the films is higher than that of the oxygen annealed films. However, these films (annealed in argon at high temperature) exhibit a significantly high MR ratio. Nam et al. [Nam01] suggested that the MR property is likely to be related to microstructure changes caused by annealing. Annealing causes recrystallization and grain growth and hence increase in grain size. Near the grain boundaries, the pairs of spins of Mn^{3+} and Mn^{4+} may not be parallel. As a result the electron transfer between pairs of Mn^{3+} and Mn^{4+} ions across the grain boundary is difficult and the resistance is high. An increase in the grain size reduces the amount of grain boundaries in a specified area. As a result, smaller fields are necessary to align these spins, and hence the suppression of resistance is much higher for a given magnetic field and as such higher MR ratios.

However, the improvement in the microstructure does not explain the increase in the resistance of the high temperature argon annealed films. One might expect here that there should be loss of oxygen from the films and hence the resistance of the films should be higher. However, our XRD results indicate a decrease in the lattice parameter of the films compared to as deposited films (though higher than the high temperature oxygen annealed films). Further, RBS analysis results indicated that the films have stoichiometric composition of oxygen. So, the increase in the resistance of the films must have some other origin. Another observation made from the RBS analysis experiments is the creation of vacancies on the lanthanum site. Argon annealed film has higher lanthanum vacancies than that of oxygen annealed films. This probably indicates that lanthanum

comes out much more easily than oxygen in these films. The lanthanum deficiency results in internal doping [Man95]. The creation of vacancies on the lanthanum site, whose role may be enhanced by suitable annealing, might be responsible for the drastic improvement in the MR ratio and slight improvement in the transition temperature in addition to the improvement in microstructure in case of argon annealed films. As there is no decrease in the oxygen content of the films (from our chemical composition measurements), the increase in the resistance of the films must be due to the vacancies created on the lanthanum site. Vacancies on the lanthanum site lead to localization effects, which affect the mobility of charge carriers. Since the density of the lanthanum deficiency is higher in argon annealed films, the localizing effect of random vacancies is stronger in these films. Therefore, the random potential fluctuations due to missing La^{3+} ions will favor the Anderson localization strongly in these films [Ran96]. In case of oxygen annealed films also, there are some vacancies created on the lanthanum site. However, we have observed a small decrease in the resistance as compared to as deposited films. Increase in the oxygen content of the film leads to an increase in the Mn^{4+} ions, which are the carriers in LCMO films. Thus, we have two simultaneous effects trying to affect the resistance of the films – decrease in the resistance due to increase in the number of carriers (Mn^{4+}) and increase in the resistance due to the vacancies on the lanthanum site. In case of argon annealed films, which have higher lanthanum vacancies, the latter is dominant, which leads to an increase in the resistance of the films. In case of oxygen annealed films, the former is slightly dominant leading to suppression in the resistance. Vacancies are also created in films annealed at low temperatures. However, these vacancies created on the lanthanum site probably do not

have any effect on the properties of the film in the absence of suitable annealing temperature or have an effect only when the crystallinity and oxygen content of the films is improved

Vacuum annealed samples appear to have undergone the most deleterious heat treatment. The loss of oxygen from the film leads to the conversion of two Mn^{4+} ions to Mn^{3+} ions. Sun et al. [Sun00] suggested the presence of critical oxygen content for the occurrence of metal to insulator transition (I-M) in the LCMO films. According to Schiffer et al. [Sch95], I-M transition will disappear in the compound $\text{La}_{1-x}\text{Ca}_x\text{MnO}_3$ with a $\text{Mn}^{4+}/\text{Mn}^{3+}$ ratio less than 0.17. In the vacuum annealed samples, there may be a depletion of oxygen to the extent in which $\text{Mn}^{4+}/\text{Mn}^{3+}$ ratio is less than 0.17. Hence these films show insulating behavior down to 10 K.

Magnetic Properties

Temperature dependence of magnetization of the as deposited and high temperature annealed films is shown in Figure 4.7. The temperature where the bulk of the zero field magnetization disappears is taken as the transition temperature (T_c). According to the figure, the transition temperatures for the three films, as deposited and 900 °C oxygen and argon annealed films, are 260, 290 and 270 K respectively. A comparison of T_c and T_{MR} (temperature at which maximum MR occurs) values of each film indicate that T_c and T_{MR} are equal for all the films within experimental error. Upon annealing the volumetric saturation moment M_s increases due to increased ferromagnetic ordering and compacity. This can also be probably understood as a decrease in the defects and magnetic inhomogeneity present in the films upon annealing.

Figure 4.8 shows the M vs H measurements for the three films as deposited and 900 °C oxygen and argon annealed films at 10 K. The films exhibit decreased coercivities, squarer behavior and increased magnetization values upon annealing. This behavior may be understood from the improvement in the microstructure, annealing defects and decrease in magnetic inhomogeneity of the films. Also, both oxygen and argon annealed films show almost identical loops – same coercivity and magnetization values. This might shed light on the properties of the films. Since both the films show similar chemical compositions except for different lanthanum deficiencies and have gone through the similar microstructural improvements, the differences in the properties observed might be due to different lanthanum vacancies.

Conclusions

A systematic post deposition heat treatment study showed the effect of oxygen content, crystallinity and self-doping in $\text{La}_{0.7}\text{Ca}_{0.3}\text{MnO}_3$ films deposited under identical conditions. Low temperature (500 °C) oxygen and argon anneals have shown little effect on the transition temperature or MR ratio. A High temperature (900 °C) oxygen anneal significantly improved the transition temperature of the films while high temperature (900 °C) argon anneal in the same films caused a substantial increase in the MR ratio. Vacuum annealed samples have shown deteriorated properties. The improvement in the properties of high temperature (900 °C) annealed films over as-deposited and low temperature (500 °C) annealed films can be attributed to increase in the oxygen content, uniform depth distribution of oxygen and enhancement in the crystallinity of the films. The temperature of 500 °C is therefore not a high enough temperature for either oxygen incorporation/removal or to cause recrystallization and grain growth to improve the film

crystallinity. Differences in the behavior of the high temperature argon and oxygen annealed films might be due to differences in the lanthanum vacancies and elimination of MnO fraction. The transition temperature seemed to be related to the MnO fraction in the film, while the magnetoresistance to the vacancies on the lanthanum site.

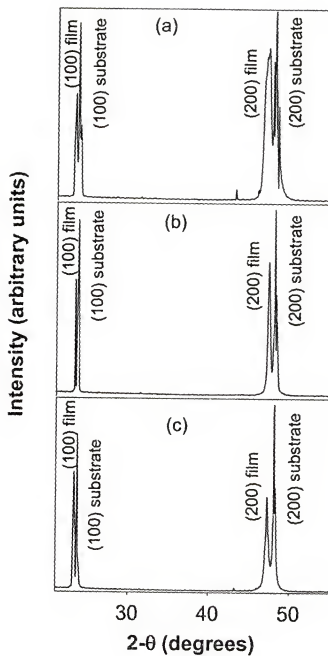


Figure 4.1: X-ray diffraction patterns of $\text{La}_{0.7}\text{Ca}_{0.3}\text{MnO}_3$ films, (a) no anneal, (b) 900 °C oxygen anneal, and (c) 900 °C argon anneal

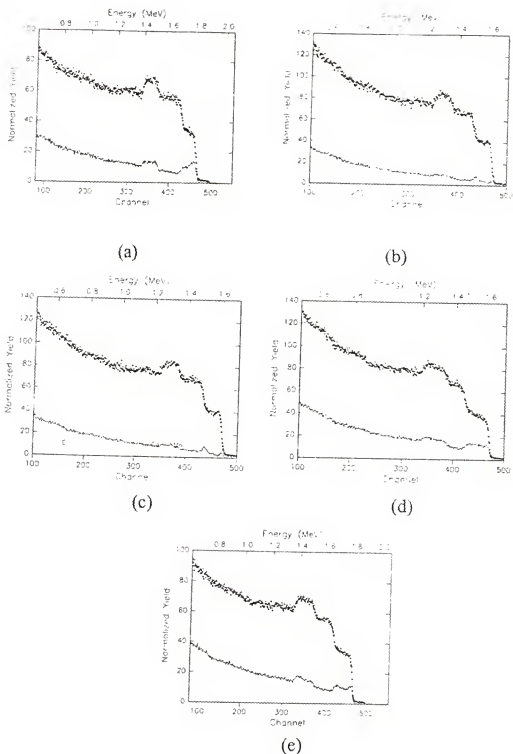


Figure 4.2: RBS spectra (random and channeling) of $\text{La}_{0.7}\text{Ca}_{0.3}\text{MnO}_3$ films, (a) no anneal, (b) 900 °C oxygen anneal, (c) 900 °C argon anneal, (d) 500 °C oxygen anneal, and (e) 500 °C argon anneal

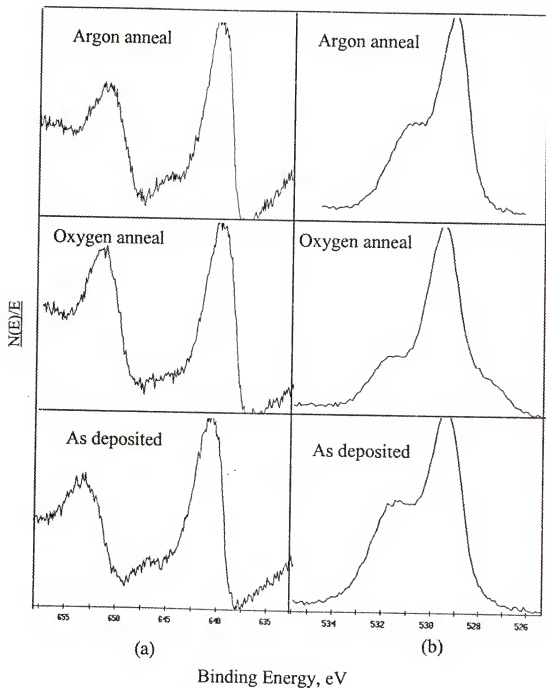


Figure 4.3: XPS spectra of the as-deposited, 900 °C oxygen and argon annealed films (a) Mn 2p and (b) O 1s regions

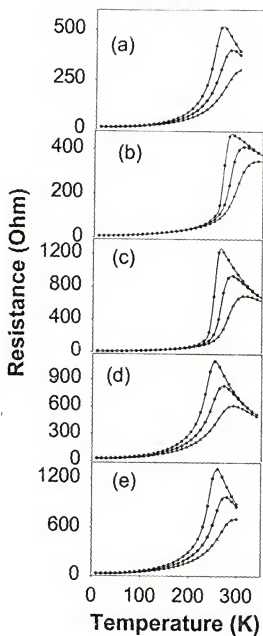


Figure 4.4: Variation of electrical resistance with temperature for (a) no anneal, (b) 900 °C oxygen anneal, (c) 900 °C argon anneal, (d) 500 °C oxygen anneal, and (e) 500 °C argon anneal (filled circle (0 T), filled diamond (2 T) and filled triangle (5 T))

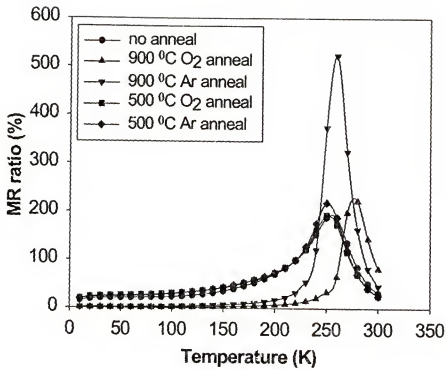


Figure 4.5: Variation of MR ratio with temperature for $\text{La}_{0.7}\text{Ca}_{0.3}\text{MnO}_3$ films subjected to various post deposition heat treatments

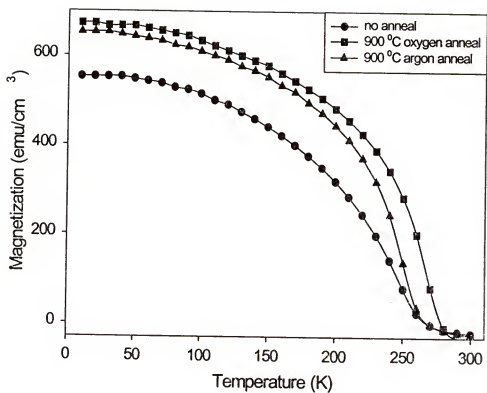


Figure 4.6: Variation of magnetization with temperature at 0.5 T for $\text{La}_{0.7}\text{Ca}_{0.3}\text{MnO}_3$ films as deposited and annealed at 900 °C in oxygen and argon ambient

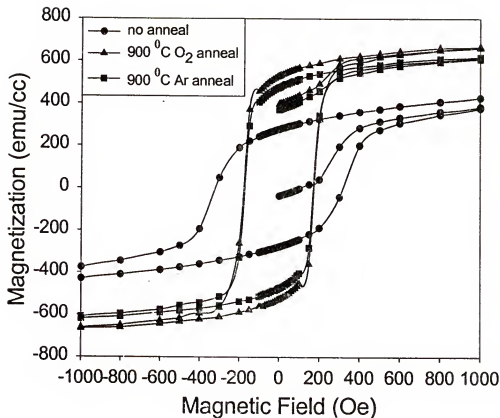


Figure 4.7: M - H curves at 10 K for $\text{La}_{0.7}\text{Ca}_{0.3}\text{MnO}_3$ films as deposited and annealed at 900 °C in oxygen and argon ambient

CHAPTER 5

STUDY OF SELF, EXTERNAL AND MIXED DOPED SYSTEMS

Overview

Self-doped lanthanum manganites, represented by the general formula, $\text{La}_{1-x}\text{MnO}_3$, are interesting because they exhibit similar properties as that of hole doped manganites without any external doping. There are relatively very few studies in the literature reporting the transport and magnetic properties of self-doped lanthanum manganites [Man95, Gup95, deS98, Pig97, Brio99, Top97]. Self-doped lanthanum manganites can be synthesized using lanthanum deficiency at lanthanum sites. Neutron diffraction and x-ray diffraction studies carried out on LaMnO_3 indicate that this compound does exist as a single-phase defect perovskite with a range of vacancies principally on the lanthanum sites [Tof74]. The electronic doping in lanthanum deficient $\text{La}_{1-x}\text{MnO}_3$ should be similar to that in other lanthanum manganites obtained by divalent substitution. In other words, the nonstoichiometric LaMnO_3 compound will have mixed $\text{Mn}^{3+}/\text{Mn}^{4+}$ valence in a manner similar to that in the divalent substituted compounds $\text{La}_{1-x}\text{M}_x\text{MnO}_3$ (as already discussed briefly in literature survey).

This chapter reports the growth and characterization of $\text{La}_{1-x-y}\text{Ca}_x\text{MnO}_3$ systems in thin film form with $x = 0, 0.3$ and 0.2 ; $y = 0.3, 0$ and 0.1 . The three different compositions have been chosen to differentiate and understand the effects of external, internal and a combination of external and internal (mixed) doping on the transport and magnetic properties of lanthanum manganites with the same lanthanum content. If M

substitution is equivalent to hole doping and oxygen is present in stoichiometric amount, $\text{La}_{0.7}\text{Ca}_{0.3}\text{MnO}_3$ ($x = 0.3$, $y = 0$), $\text{La}_{0.7}\text{MnO}_3$ ($x = 0$, $y = 0.3$), and $\text{La}_{0.7}\text{Ca}_{0.2}\text{MnO}_3$ ($x = 0.2$, $y = 0.1$) represent external, internal, and mixed doped systems, respectively. In order to maintain charge neutrality, these dopings result in a transformation of triply charged Mn ions to quadruply charged Mn ions which are shown in the respective extended formula: $\text{La}_{0.7}\text{Ca}_{0.3}\text{Mn}_{0.7}(\text{III})\text{Mn}_{0.3}(\text{IV})\text{O}_3$, $\text{La}_{0.7}\text{Mn}_{0.1}(\text{III})\text{Mn}_{0.9}(\text{IV})\text{O}_3$ and $\text{La}_{0.7}\text{Ca}_{0.2}\text{Mn}_{0.5}(\text{III})\text{Mn}_{0.5}(\text{IV})\text{O}_3$ respectively. Thus in all these systems, vacancies on the lanthanum site are systematically varied.

Experimental Details

Self doped, mixed doped and external doped pellets with nominal composition $\text{La}_{0.7}\text{MnO}_3$, $\text{La}_{0.7}\text{Ca}_{0.2}\text{MnO}_3$ and $\text{La}_{0.7}\text{Ca}_{0.3}\text{MnO}_3$ were prepared by ceramic method discussed before in chapter 3. In situ film deposition of these materials on (100) LaAlO_3 were carried out in a pulsed laser ablation system. A 248 nm KrF pulsed laser with 5 Hz repetition rate and 1.6 J/cm^2 energy density was used. A substrate temperature of 700 – 800 °C and oxygen pressure of 250 mTorr was used during the deposition of the films. The films deposited were characterized using x-ray diffraction (XRD), atomic force microscopy (AFM) and transmission electron microscopy (TEM) measurements. Samples for transmission electron microscope studies were prepared by a conventional technique, which was discussed in chapter 3. Gatan dimpler was used for dimpling and ion milling was done using the precision ion polishing system (PIPS). The guns were oriented at an angle of 8° with respect to the surface and a voltage of 4.5 KeV was used during milling. Electron diffraction patterns and high resolution images were obtained using JEOL 2010FX microscope operated at 200 KV. The resolution of the microscope is

of the order of 1.8\AA . Resistivity and magnetization measurements were performed using the quantum design superconducting quantum interference device (SQUID) magnetometer. Temperature dependence of resistance of the films was examined in zero and applied field using a four-probe technique. Both transport current and applied field were in the film plane. The MR ratio, $\Delta R/R(H)$, was calculated as described in chapter 3. The thin film samples were held in a plastic straw. Measured data contained contributions from the film, LaAlO_3 substrate, which is diamagnetic with a small paramagnetic impurity and plastic straw, which is diamagnetic. The contribution from the straw has been corrected.

Results and Discussion

Structural Characterization

XRD patterns of $\text{La}_{0.7}\text{Ca}_{0.3}\text{MnO}_3$, $\text{La}_{0.7}\text{Ca}_{0.2}\text{MnO}_3$ and $\text{La}_{0.7}\text{MnO}_3$ targets used for pulsed laser deposition experiments are shown in Figure.5.1. All the peaks in each XRD pattern could be indexed for a single-phase compound except for a weak peak at $2\theta = 36^\circ$ corresponding to Mn_3O_4 only in case of $\text{La}_{0.7}\text{MnO}_3$ system. From this figure, we can also see that in case of the self doped system ($\text{La}_{0.7}\text{MnO}_3$), there is a splitting in the peaks while no such splitting is seen in the case of the other two systems. It has been pointed out that this kind of splitting may arise due to the distortions of the lattice from cubic symmetry [Jon50]. The number and relative intensities of the diffraction lines into which an ideal reflection splits by distortion of the unit cube is characteristic of the symmetry of the distorted structure. In some cases, the splitting may be so slight that the separate reflections are almost indistinguishable [Meg46]. Therefore, the splitting of XRD peaks in case of the self-doped system indicates that the self doped system has

possibly undergone a distortion from cubic structure, while the absence of such splitting in case of the other two systems suggests that there is apparently no distortion from cubic symmetry in them. XRD patterns of the films fabricated from the corresponding targets are shown in Figure. 5.2. The films were grown on (100) LaAlO_3 substrates at 700 °C and were 1000 Å thick. According to XRD patterns, all the films are single phase with (00 l) peaks with $l = 1$ and 2. The presence of only (00 l) peaks implies the highly textured growth of all the films on (100) LaAlO_3 substrate. The lattice parameters of $\text{La}_{0.7}\text{Ca}_{0.3}\text{MnO}_3$, $\text{La}_{0.7}\text{Ca}_{0.2}\text{MnO}_3$ and $\text{La}_{0.7}\text{MnO}_3$ films were found to be 3.87, 3.91 and 3.90 Å, respectively.

Figure.5.3 shows the AFM micrographs of $\text{La}_{0.7}\text{Ca}_{0.3}\text{MnO}_3$, $\text{La}_{0.7}\text{Ca}_{0.2}\text{MnO}_3$ and $\text{La}_{0.7}\text{MnO}_3$ films. The root mean square (rms) roughnesses of the films measured using AFM were found to be 1.425 nm, 3.17 nm and 5.83 nm respectively. The value of rms roughness obtained suggests that as-deposited manganite thin films in the present study are very smooth and the roughness observed is sometimes similar to the roughness of the bare substrate surface.

Multibeam bright field electron diffraction contrast images have been used to obtain an overview of the microstructure of the films. Figure 5.4 shows such images of the cross section of $\text{La}_{0.7}\text{Ca}_{0.3}\text{MnO}_3$, $\text{La}_{0.7}\text{Ca}_{0.2}\text{MnO}_3$ and $\text{La}_{0.7}\text{MnO}_3$ films grown on (100) LaAlO_3 substrate at 700 °C. We can see that in all the three cases the film-substrate interface is flat and sharp and all the films have a similar microstructure. A minute observation of these images suggests that the film microstructure can be qualitatively divided into two layers. The first layer, closer to the substrate, appears to be perfectly coherent with the substrate and the second layer shows a typical domain structure. The

thicknesses of the films determined from these images are ~ 1000 Å which, coincides with the thickness data obtained from ellipsometry.

Electron diffraction patterns obtained from the cross section of the $\text{La}_{0.7}\text{Ca}_{0.3}\text{MnO}_3$, $\text{La}_{0.7}\text{Ca}_{0.2}\text{MnO}_3$ and $\text{La}_{0.7}\text{MnO}_3$ films on (100) LaAlO_3 substrate along [112], [001] and [011] zone axes are shown in Figure 5.5, respectively. These patterns are the superposition of the patterns produced by the substrate and the film. It can be seen from these diffraction patterns that there is clearly a doubling of periodicity in the direction of the substrate normal. Figure 5.6 shows the expanded electron diffraction pattern obtained from the cross-section of a $\text{La}_{0.7}\text{Ca}_{0.3}\text{MnO}_3$ film on (100) LaAlO_3 substrate along [112] zone axis. Although it appears that all the films have a cubic crystal pattern, in actuality it is found that the lattice is not cubic but to a good approximation orthorhombic since $g_{222} \neq g_{110}$ [Leb98]. The angle between g_{222} and g_{110} is equal to 90° with an experimental error of ± 1.0 . It can also be seen from Figure 5.6 that spots in rows parallel to the substrate are not split (or feebly split), while the spots in the rows along the substrate normal are distinctly split. The splitting of spots is attributed to a difference in lattice parameters between the film and the substrate, which is much more pronounced along the perpendicular direction to the substrate surface than along the substrate surface [Leb98]. Due to substrate effect [Jin95b], the film along the substrate surface is perfectly coherent with the substrate lattice, and hence, splitting is not seen.

Figure 5.7 shows high-resolution transmission electron microscopy (HRTEM) images of the interface of $\text{La}_{0.7}\text{Ca}_{0.3}\text{MnO}_3$, $\text{La}_{0.7}\text{Ca}_{0.2}\text{MnO}_3$ and $\text{La}_{0.7}\text{MnO}_3$ films on (100) LaAlO_3 substrate. All the films were grown under identical deposition conditions. In case of $\text{La}_{0.7}\text{MnO}_3$ film, high-resolution image of the interface could not be obtained as the

interface was not thin enough. It is evident from these images that all the films grow epitaxially on (100) LaAlO_3 substrates. These images also indicate that the interface between the films and the substrate is quite sharp with an excellent lattice match between the substrate and the film.

Magnetoresistance Behavior

The variation of electrical resistance in zero and applied field (5T) as a function of temperature for $\text{La}_{0.7}\text{Ca}_{0.3}\text{MnO}_3$, $\text{La}_{0.7}\text{Ca}_{0.2}\text{MnO}_3$ and $\text{La}_{0.7}\text{MnO}_3$ films is shown in Figure 5.8. The three films were grown under identical conditions so that the film thickness and oxygen content of all the films could be kept identical. According to the variation of resistance shown in Figure 5.8, all the three films have similar qualitative magnetotransport behavior. That is, all the films undergo an insulator to metal (I-M) transition as the temperature is lowered down and the resistance of all the films is suppressed significantly with the application of magnetic field. As observed frequently by others in several manganite systems, here also the suppression in film resistance in each case is maximum near the resistivity peak in zero field. However, the temperature at which I-M transition takes place in each system is different from each other. The internal doped system ($\text{La}_{0.7}\text{MnO}_3$) attains the metallic state earliest (240 K) followed by the mixed doped system ($\text{La}_{0.7}\text{Ca}_{0.2}\text{MnO}_3$), and external doped ($\text{La}_{0.7}\text{Ca}_{0.3}\text{MnO}_3$) system with I-M transitions around 220 and 200 K, respectively. Thus, it appears that the electronic doping in self-doped compounds is similar to that of the compounds with external doping.

The difference in the values of I-M transition temperature in these systems may be explained on the basis of Mn^{4+} content. As has been discussed in the previous chapter (chapter 4), the ferromagnetic transition temperature is strongly determined by the

number of Mn^{4+} ions. The mixed $\text{Mn}^{3+}/\text{Mn}^{4+}$ valence gives rise to both ferromagnetism and metallic behavior in $\text{La}_{0.7}\text{Ca}_{0.3}\text{MnO}_3$ films, and is responsible for the occurrence of colossal magnetoresistance [Zen51]. The Mn^{4+} content of the compounds investigated in the present study, $\text{La}_{0.7}\text{Ca}_{0.3}\text{MnO}_3$, $\text{La}_{0.7}\text{Ca}_{0.2}\text{MnO}_3$ and $\text{La}_{0.7}\text{MnO}_3$, were calculated to be 0.3, 0.5, and 0.9, respectively. Therefore, these compounds with different Mn^{4+} contents are likely to exhibit different transition temperatures. $\text{La}_{0.7}\text{MnO}_3$ films which have the highest Mn^{4+} content has the highest transition temperature (240 K) followed by $\text{La}_{0.7}\text{Ca}_{0.2}\text{MnO}_3$ (I-M transition: 220 K) and $\text{La}_{0.7}\text{Ca}_{0.3}\text{MnO}_3$ (I-M transition: 200 K) films.

Resistance-temperature plots also indicate that the self-doped system exhibits the highest resistance followed by mixed doped and external doped systems. The resistance of the film seems to depend on the vacancies on the lanthanum site (as already discussed in the previous chapter). Due to the difference in the vacancies at La-sites (arising from lanthanum deficiency), the localization effects, and hence, the mobility of charge carriers is different in different systems. Since the density of lanthanum deficiency is more in $\text{La}_{0.7}\text{MnO}_3$ system (internal/self doped), the localizing effect of random vacancies is stronger in $\text{La}_{0.7}\text{MnO}_3$ films than that in $\text{La}_{0.7}\text{Ca}_{0.2}\text{MnO}_3$ (mixed doped) film. Therefore, the random potential fluctuations due to missing La^{3+} ions will favor the Anderson localization more strongly in the former system than in the later system [Ran96]. As a result of this, the resistance of $\text{La}_{0.7}\text{MnO}_3$ is higher than that of the $\text{La}_{0.7}\text{Ca}_{0.2}\text{MnO}_3$ film. There is no such localization effect in the stoichiometric $\text{La}_{0.7}\text{Ca}_{0.3}\text{MnO}_3$ films due to the absence of vacancies, which is manifested with the observation of smallest resistance among the three systems discussed here.

The MR ratios of $\text{La}_{0.7}\text{Ca}_{0.3}\text{MnO}_3$, $\text{La}_{0.7}\text{Ca}_{0.2}\text{MnO}_3$ and $\text{La}_{0.7}\text{MnO}_3$ films were calculated using the data in Figure 5.8. The MR ratios obtained are plotted in Figure 5.9 as a function of temperature at 5 T. The figure shows that $\text{La}_{0.7}\text{Ca}_{0.3}\text{MnO}_3$ has the highest MR ratio (~825%) which is followed by $\text{La}_{0.7}\text{Ca}_{0.2}\text{MnO}_3$ (MR ratio~750 %) and $\text{La}_{0.7}\text{MnO}_3$ (MR ratio ~700%) systems. MR property of the film seems to be related to the microstructure of the film rather than the Mn^{4+} content or vacancies on the lanthanum site (as has been discussed in chapter 4). The presence of defects, impurities, grain boundary scattering may affect the MR properties of the film. Self-doped system is the structure, which has the maximum deviation from the ideality. Hence, it exhibits the least magnetoresistance ratio, followed by mixed doped and external doped systems.

For a much better understanding of the nature of the transport phenomena in each film, we have analyzed low temperature resistance for all the three films using a polynomial expansion in temperature (T). As shown in Fig. 5.10, resistances of $\text{La}_{0.7}\text{Ca}_{0.3}\text{MnO}_3$ and $\text{La}_{0.7}\text{Ca}_{0.2}\text{MnO}_3$ films are fit well by the equation: $R = R_0 + R_I T^2$, whereas the resistance of $\text{La}_{0.7}\text{MnO}_3$ film is fit well by equation: $R = R_0 + R_I T^{2.5}$ for temperatures less than $T_c/2$. Here, T_c is the paramagnetic-to-ferromagnetic (FM) transition temperature and R_0 is the residual resistance. The $R_I T^{2.5}$ fit suggests a combination of electron-electron, electron-phonon, and electron-magnon scattering (observed in the case of $\text{La}_{0.7}\text{MnO}_3$), while $R_I T^2$ fits suggest an electron-electron scattering (observed in $\text{La}_{0.7}\text{Ca}_{0.2}\text{MnO}_3$ and $\text{La}_{0.7}\text{Ca}_{0.3}\text{MnO}_3$). The temperature dependence for any of these systems is not fit well by $R_I T^{4.5}$, as was suggested by Kubo and Ohata [Kub72] based on a calculation of electron-magnon scattering. However, an equation of the form $R_0 + R_I T^2 + R_I T^{4.5}$, which represents a combination of electron-

electron scattering (T^2) and electron-magnon scattering $T^{4.5}$ is fit well by all the three systems (Figure 5.11). In contrast to the $R = R_0 + R_1 T^2$ and $R = R_0 + R_1 T^{2.5}$ fittings up to $T_c/2$, the $R_0 + R_1 T^2 + R_2 T^{4.5}$ fitting has been carried out over an extended range of temperatures up to T_c of each system. The values of the R_1 and R_2 fitting parameters used in the $R_0 + R_1 T^2 + R_2 T^{4.5}$ fitting were 1.7×10^{-4} and 2.4×10^{-8} , 4.5×10^{-4} and 7.6×10^{-10} , and 6.7×10^{-4} and 8.7×10^{-10} , respectively, for the $\text{La}_{0.7}\text{Ca}_{0.3}\text{MnO}_3$, $\text{La}_{0.7}\text{Ca}_{0.2}\text{MnO}_3$ and $\text{La}_{0.7}\text{MnO}_3$. The confirmation of all three systems to the same type of fitting in the higher range of temperatures may be considered to suggest that the contribution of electron-phonon scattering is reduced due to more random vibrations of the lattices at higher temperatures. It should be noted; however, that the residual resistances for the three films are different. Residual resistance may arise from impurity, defects, grain boundary and domain wall scattering. We see that the value of R_0 (the dimensions of all the films were identical) is highest for $\text{La}_{0.7}\text{MnO}_3$, followed by $\text{La}_{0.7}\text{Ca}_{0.2}\text{MnO}_3$ and $\text{La}_{0.7}\text{Ca}_{0.3}\text{MnO}_3$. As discussed earlier, the localization effects arising due to the difference in vacancies on La-sites cause a difference in the mobility of charge carriers in different systems. In case of $\text{La}_{0.7}\text{MnO}_3$, the localization effects are the highest, and hence, mobility of the charge carriers is the least, which leads to a higher value of R_0 .

Shown in Fig. 5.12 is the variation of MR (at 3T) as a function of temperature in low-temperature regime for $\text{La}_{0.7}\text{Ca}_{0.3}\text{MnO}_3$, $\text{La}_{0.7}\text{Ca}_{0.2}\text{MnO}_3$ and $\text{La}_{0.7}\text{MnO}_3$ films. There are three interesting features which can be observed from these plots: (i) there is a minimum in MR for all the films at low temperatures (0.03% for $\text{La}_{0.7}\text{MnO}_3$, 0.27 % for $\text{La}_{0.7}\text{Ca}_{0.2}\text{MnO}_3$ and 4.7% for $\text{La}_{0.7}\text{Ca}_{0.3}\text{MnO}_3$), (ii) these minima occur at different temperatures (110 K for $\text{La}_{0.7}\text{MnO}_3$, 65 K for $\text{La}_{0.7}\text{Ca}_{0.2}\text{MnO}_3$ and 40 K for

$\text{La}_{0.7}\text{Ca}_{0.3}\text{MnO}_3$), and (iii) the MR ratios increase beyond these minima. While the first and second features are material dependent, the third feature seems to be associated with domain wall effects [Sch95, Cul72]. According to Schiffer et al. [Sch95], the domain wall contribution to the MR probably results from the strong correlation between local FM order and metallic behavior in double exchange. At low fields, spins in the domain walls are not ferromagnetically aligned, causing more resistance than when the spins are ferromagnetically aligned in higher fields [Fis68]. Since the spin-disordered phase is insulating, even a small perturbation from ferromagnetism within the domain walls can lead to significant resistivity. In strong fields, magnetizations are nearly parallel and the domain walls are less of a perturbation away from ferromagnetism. Evidence in favor of this argument comes from MR measurements at low temperatures using high external magnetic field. The results obtained are shown in the inset of Figure 5.12. It is clear from the plot in the inset figure that MR ratio does not show a minimum as observed in the case of MR measurements at 3T. This might be due to the fact that either the domain walls are of negligible thickness or the spins in the domain walls are already aligned in 5T. Obviously, if the domain walls were very thin, the perturbation due to them would be weak. Hence, MR ratio may not increase furthermore when temperature is lowered below T_c in presence of high magnetic field.

In the regime above T_c , resistance of all the three systems closely follow the law predicted by small polaron hopping: $\ln(R/T) = \ln(R_h) + E_a/k_bT$ [Mot71], as opposed to that predicted for a semiconductor: $\ln(R)\propto 1/T$ (Figure 5.13). Therefore, we conclude that the temperature dependence of the resistance is due to the temperature dependence of mobility while the carrier concentration remains constant [Sny96].

Magnetic Properties

Using spin only moment (orbital contribution quenched), saturation magnetization expected for high spin manganese in octahedral co-ordination is given by, $\mu = g s \mu_B$, $g = 2$. Due to the presence of mixed valency of Mn ions in a doped lanthanum manganite, this formula can be expanded to $\mu = 2\mu_B [nx2 \text{ (from Mn}^{3+}) + (1-n)3/2 \text{ (from Mn}^{4+})]$, where n and $(1-n)$ are the atomic ratios of Mn^{3+} and Mn^{4+} ions in the compound. The values of s for Mn^{3+} and Mn^{4+} are 2 and 3/2, respectively, if only the spin moments are considered. Using the above formula the net magnetic moment per formula unit for $\text{La}_{0.7}\text{Ca}_{0.3}\text{MnO}_3$ is calculated to be $\mu = 2\mu_B [0.7 \times 2 \text{ (from Mn}^{3+}) + 0.3 \times 3/2 \text{ (from Mn}^{4+})] = 3.7\mu_B$. Similarly, the net magnetic moments per formula unit for $\text{La}_{0.7}\text{Ca}_{0.2}\text{MnO}_3$ and $\text{La}_{0.7}\text{MnO}_3$ are calculated to be $3.5\mu_B$ and $3.10\mu_B$, respectively. This corresponds to a saturation magnetization of 484.66 emu/cm^3 , 543.01 emu/cm^3 and 592.02 emu/cm^3 for $\text{La}_{0.7}\text{MnO}_3$, $\text{La}_{0.7}\text{Ca}_{0.2}\text{MnO}_3$ and $\text{La}_{0.7}\text{Ca}_{0.3}\text{MnO}_3$. In these calculations for saturation magnetization, the volume of each unit cell was estimated using the lattice parameter measured by XRD and TEM measurements and assuming a cubic structure for each material.

It is known that the double-exchange interaction between Mn^{3+} and Mn^{4+} ions provides a ferromagnetic coupling, resulting in a ferromagnetic long-range order below the Curie temperature T_c . Figure 5.14 shows the variation of magnetization with temperature at 0.5T. The temperature where the bulk of the zero field magnetization disappears is taken as the transition temperature (T_c). According to Figure 5.14, the transition temperatures for the three films, $\text{La}_{0.7}\text{Ca}_{0.3}\text{MnO}_3$, $\text{La}_{0.7}\text{MnO}_3$, and $\text{La}_{0.7}\text{Ca}_{0.2}\text{MnO}_3$ are 200 K, 240 K and 220 K respectively. The value of saturation magnetization measured from the data in Figure 5.14 for $\text{La}_{0.7}\text{Ca}_{0.3}\text{MnO}_3$, $\text{La}_{0.7}\text{MnO}_3$, and

$\text{La}_{0.7}\text{Ca}_{0.2}\text{MnO}_3$ films are 595.05 emu/cm^3 , 585 emu/cm^3 and 575.75 emu/cm^3 respectively. We see that the saturation magnetization values are close to the calculated value only in the case of $\text{La}_{0.7}\text{Ca}_{0.3}\text{MnO}_3$. In case of $\text{La}_{0.7}\text{MnO}_3$, and $\text{La}_{0.7}\text{Ca}_{0.2}\text{MnO}_3$ films, there is considerable deviation from the calculated value, much higher for the self-doped case. However, from the comparison of experimentally measured saturation magnetizations of the three systems, we see that the deviation is much less than that observed in calculated values. This deviation can be attributed to the defects, impurities and grain boundary scattering. A comparison of T_c and T_{MR} (temperature at which maximum MR occurs) values of each film indicated that T_c and T_{MR} are equal for all the films within experimental certainty. Figure 5.15 shows M vs H measurements for all the three films at 10K. All the films show reasonably square hysteresis loops. From the figure, we can see that $M(H)$ at low temperatures increases rapidly for $H \leq 0.5\text{T}$ and then saturates for all the films.

A T^2 dependence of magnetization is predicted by the Moriya theory of spin fluctuation in itinerant electron ferromagnets, as shown by a calculation for the weak metallic ferromagnet Ni_3Al [Lon85]. A T^2 dependence in a simplest model is due to single (k -space) particle spin-flip excitations, while a $T^{3/2}$ law is expected for collective oscillations [Kle95]. From Figure 5.16, we can see that in $\text{La}_{0.7}\text{MnO}_3$ and $\text{La}_{0.7}\text{Ca}_{0.2}\text{MnO}_3$, saturation magnetization decreases as T^2 (single particle excitations), similar to results obtained by Snyder et al. [Sny96], while in $\text{La}_{0.7}\text{Ca}_{0.3}\text{MnO}_3$ it decrease as $T^{3/2}$ (collective oscillations).

Bolometric Properties

In addition to the applications in magnetic information storage, read heads and low-field magnetic sensors, CMR materials can also be used in bolometric devices. Bolometric application of these materials is associated with its metal-insulator transition. As these materials exhibit a large temperature coefficient of resistance, TCR (defined as $1/R \, dR/dT$) close to the resistivity peak, they seem to be potential candidates for infrared detectors. The temperature of operation (T_p) and TCR are important parameters in the development of CMR bolometers. Figure 5.17 shows the TCR and T_p for all the three films grown under identical conditions. The T_p and TCR for $\text{La}_{0.7}\text{Ca}_{0.3}\text{MnO}_3$, $\text{La}_{0.7}\text{MnO}_3$, and $\text{La}_{0.7}\text{Ca}_{0.2}\text{MnO}_3$ were found to be 180 K and 16 %/K, 225 K and 14 %/K, 205 K and 13 %/K, respectively. The values of TCR obtained here are quite high as compared to the values reported in literature [Goy97].

For bolometric applications, $\text{La}_{0.7}\text{Ca}_{0.3}\text{MnO}_3$ is superior in terms of TCR but the value of T_p is much lower compared to that of $\text{La}_{0.7}\text{MnO}_3$. Typical operating temperatures desirable for moderately cooled bolometers are in the range of 250 – 300 K. Among the three films, $\text{La}_{0.7}\text{MnO}_3$ has the highest T_p (225 K). Though $\text{La}_{0.7}\text{Ca}_{0.3}\text{MnO}_3$ has higher value of TCR (TCR = 16% and T_p = 180 K), $\text{La}_{0.7}\text{MnO}_3$ has the best combination of TCR and T_p (TCR = 14% and T_p = 225 K).

T_p , which is determined by T_c , for the three films could be explained in the same way as we have explained the I-M transition temperature before (on the basis of Mn^{4+} content). The behavior of TCR is not easily explainable on the basis of Mn^{4+} content. It is interesting to note that the TCR value for all the three films are very close though the T_p varies by as high as 45 K. Goyal et al. [Goy97] suggest that these observed differences in

the TCR are linked to the intrinsic nature of transport. The TCR probably is related to the microstructure of the film, same as the MR behavior.

Conclusions

A systematic study on the microstructure, magnetoresistance and magnetic properties of $\text{La}_{0.7}\text{Ca}_{0.3}\text{MnO}_3$, $\text{La}_{0.7}\text{MnO}_3$, and $\text{La}_{0.7}\text{Ca}_{0.2}\text{MnO}_3$, which represent external, internal, and mixed doped systems with the same lanthanum content showed the presence of different scattering mechanisms and magnetic excitations. Microstructural characterization results have shown that the films are smooth, free from impurities and grow epitaxially with negligible lattice mismatch. The results obtained showed that the electronic doping in non-stoichiometric compounds is similar to that of the compounds with divalent substitution. The variation in insulator to metal transition in these systems could be explained on the basis of Mn^{4+} content. The resistance of the films seems to depend on the vacancies on the lanthanum site, while the MR property on the microstructure of the film. Analysis of low temperature resistance has shown that in $\text{La}_{0.7}\text{Ca}_{0.3}\text{MnO}_3$ and $\text{La}_{0.7}\text{Ca}_{0.2}\text{MnO}_3$ electron-electron scattering dominates while in $\text{La}_{0.7}\text{MnO}_3$ a combination of electron-electron, electron-phonon and electron-magnon scattering dominates. High temperature resistance is consistent with small polaron hopping conductivity for all the three systems. Magnetization measurements carried out on the films showed that the films have reasonably square hysteresis loops with sharp transition temperatures (T_c). Below $T_c/2$, saturation magnetization in $\text{La}_{0.7}\text{MnO}_3$ and $\text{La}_{0.7}\text{Ca}_{0.2}\text{MnO}_3$ decreases as T^2 (single particle excitations) while in $\text{La}_{0.7}\text{Ca}_{0.3}\text{MnO}_3$ it decreases as $T^{3/2}$ (collective oscillations). Of the three systems, $\text{La}_{0.7}\text{MnO}_3$ shows the best

combination of temperature coefficient of resistance (TCR) and operating temperature (T_p) for bolometric applications.

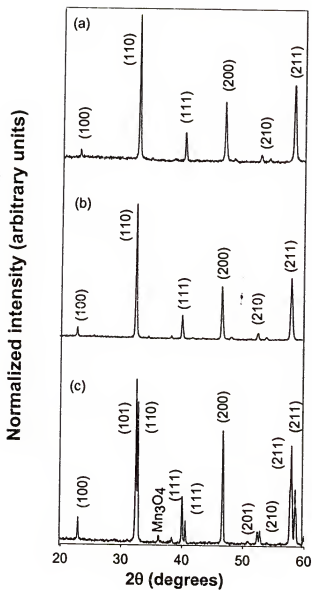


Figure 5.1: X-ray diffraction patterns of (a) $\text{La}_{0.7}\text{Ca}_{0.3}\text{MnO}_3$, (b) $\text{La}_{0.7}\text{Ca}_{0.2}\text{MnO}_3$, and (c) $\text{La}_{0.7}\text{MnO}_3$, targets synthesized using a ceramic route

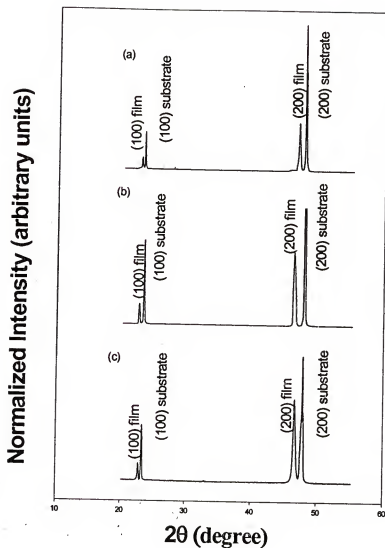
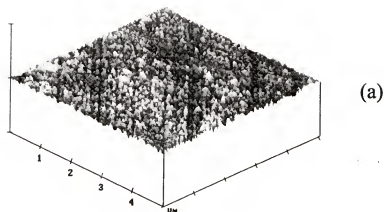
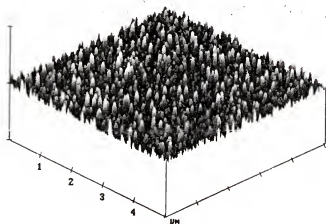


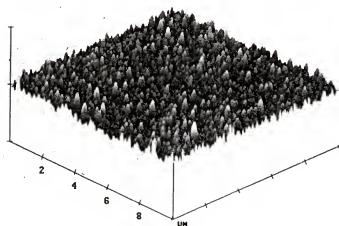
Figure 5.2: X-ray diffraction patterns of (a) $\text{La}_{0.7}\text{Ca}_{0.3}\text{MnO}_3$, (b) $\text{La}_{0.7}\text{Ca}_{0.2}\text{MnO}_3$, and (c) $\text{La}_{0.7}\text{MnO}_3$ films grown at 700 °C on (100) LaAlO_3 substrates



(a)

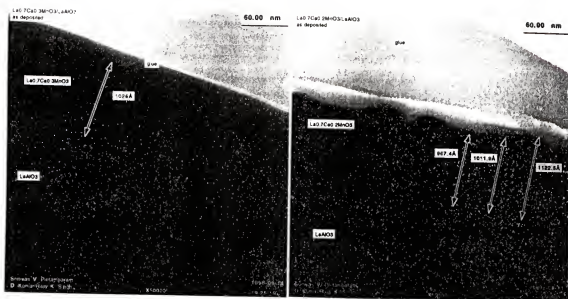


(b)



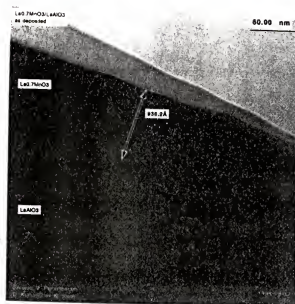
(c)

Figure 5.3: AFM micrographs of (a) $\text{La}_{0.7}\text{Ca}_{0.3}\text{MnO}_3$, (b) $\text{La}_{0.7}\text{Ca}_{0.2}\text{MnO}_3$, and (c) $\text{La}_{0.7}\text{MnO}_3$ films grown at 700 °C on (100) LaAlO_3 substrates



(a)

(b)



(c)

Figure 5.4: Multi-beam diffraction contrast images of the cross sections of (a) $\text{La}_{0.7}\text{Ca}_{0.3}\text{MnO}_3$, (b) $\text{La}_{0.7}\text{Ca}_{0.2}\text{MnO}_3$, and (c) $\text{La}_{0.7}\text{MnO}_3$ films grown at 700 °C on (100) LaAlO_3 substrates

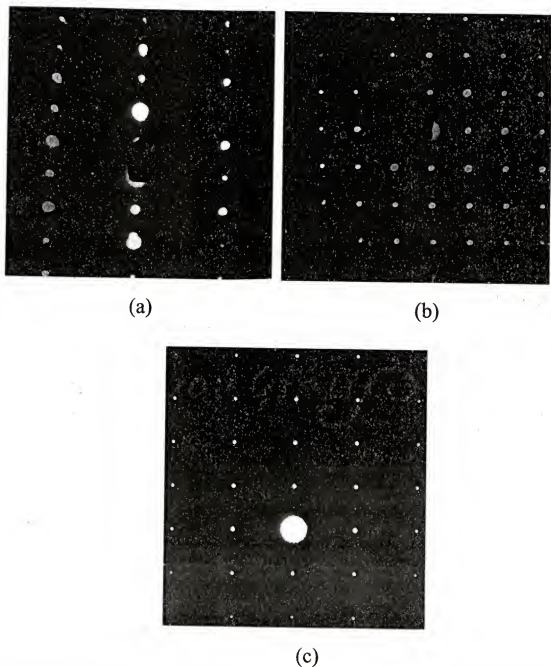


Figure 5.5: Electron diffraction patterns of the cross sections of (a) $\text{La}_{0.7}\text{Ca}_{0.3}\text{MnO}_3$, (b) $\text{La}_{0.7}\text{Ca}_{0.2}\text{MnO}_3$, and (c) $\text{La}_{0.7}\text{MnO}_3$ films grown at 700 °C on (100) LaAlO_3 substrates

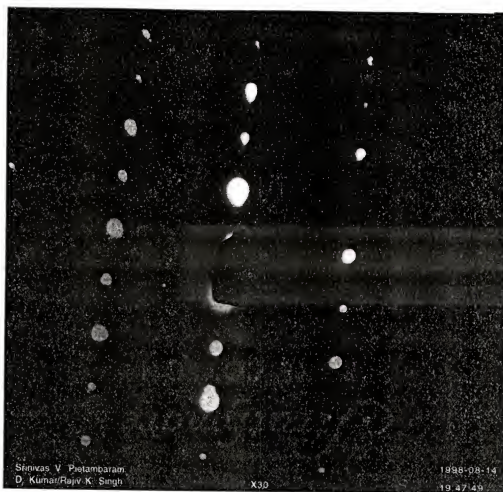


Figure 5.6: Selected area diffraction pattern of the cross section of the $\text{La}_{0.7}\text{MnO}_3$ film grown at 700 °C on (100) LaAlO_3 substrates

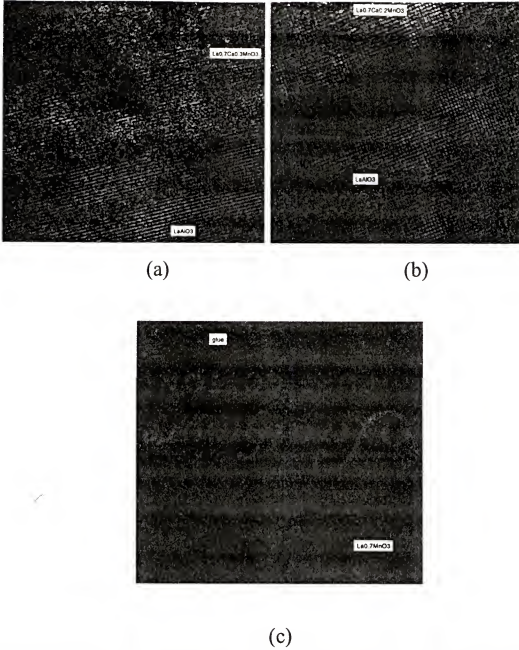


Figure 5.7: High resolution transmission electron microscopy images of the cross sections of (a) $\text{La}_{0.7}\text{Ca}_{0.3}\text{MnO}_3$, (b) $\text{La}_{0.7}\text{Ca}_{0.2}\text{MnO}_3$, and (c) $\text{La}_{0.7}\text{MnO}_3$ films grown at 700 °C on (100) LaAlO_3 substrates

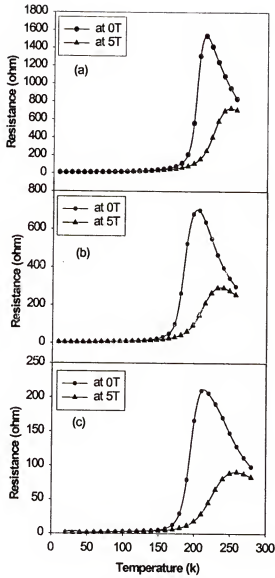


Figure 5.8: Resistance versus temperature plots for (a) $\text{La}_{0.7}\text{MnO}_3$, (b) $\text{La}_{0.7}\text{Ca}_{0.2}\text{MnO}_3$, and (c) $\text{La}_{0.7}\text{Ca}_{0.3}\text{MnO}_3$ films in 0 and 5 T magnetic field

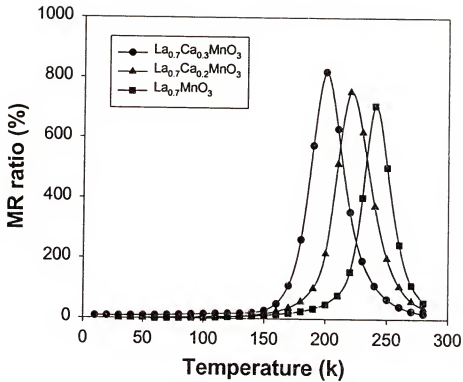


Figure 5.9: Variation of MR ratio with temperature for $\text{La}_{0.7}\text{MnO}_3$ (filled square), $\text{La}_{0.7}\text{Ca}_{0.2}\text{MnO}_3$ (filled triangle), and $\text{La}_{0.7}\text{Ca}_{0.3}\text{MnO}_3$ (filled circle) films

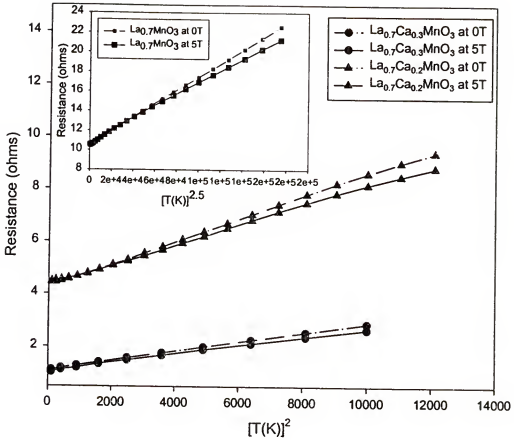


Figure 5.10: Low temperature (below $T_c/2$) resistance fits for $\text{La}_{0.7}\text{Ca}_{0.3}\text{MnO}_3$ (filled circle), $\text{La}_{0.7}\text{Ca}_{0.2}\text{MnO}_3$ (filled triangle), and $\text{La}_{0.7}\text{MnO}_3$ (inset) films at 0 and 5 T

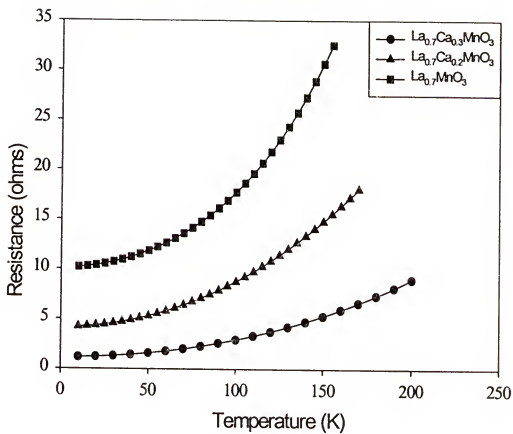


Figure 5.11: Resistance temperature fits for $\text{La}_{0.7}\text{Ca}_{0.3}\text{MnO}_3$ (filled circle), $\text{La}_{0.7}\text{Ca}_{0.2}\text{MnO}_3$ (filled triangle), and $\text{La}_{0.7}\text{MnO}_3$ (filled square) films at 0 and 5 T up to T_c

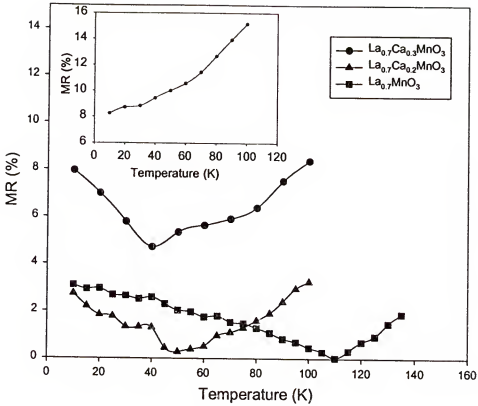


Figure 5.12: Low temperature MR for $\text{La}_{0.7}\text{Ca}_{0.3}\text{MnO}_3$ (filled circle), $\text{La}_{0.7}\text{Ca}_{0.2}\text{MnO}_3$ (filled triangle), and $\text{La}_{0.7}\text{MnO}_3$ (filled square) films at 3 T. Inset shows the low-temperature MR for $\text{La}_{0.7}\text{Ca}_{0.3}\text{MnO}_3$ at 5 T

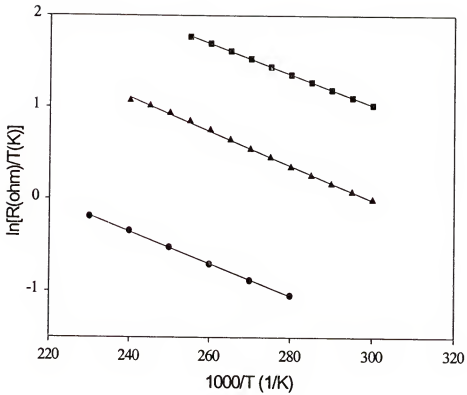


Figure 5.13: High-temperature resistance fits for $\text{La}_{0.7}\text{Ca}_{0.3}\text{MnO}_3$ (filled circle), $\text{La}_{0.7}\text{Ca}_{0.2}\text{MnO}_3$ (filled triangle), and $\text{La}_{0.7}\text{MnO}_3$ (filled square) films

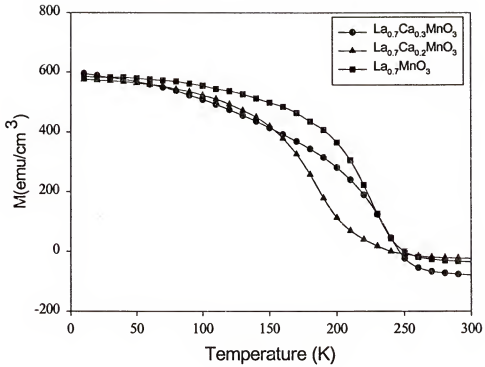


Figure 5.14: Variation of magnetization with temperature for $\text{La}_{0.7}\text{Ca}_{0.3}\text{MnO}_3$ (filled circle), $\text{La}_{0.7}\text{Ca}_{0.2}\text{MnO}_3$ (filled triangle), and $\text{La}_{0.7}\text{MnO}_3$ (filled square) films at 0.5 T

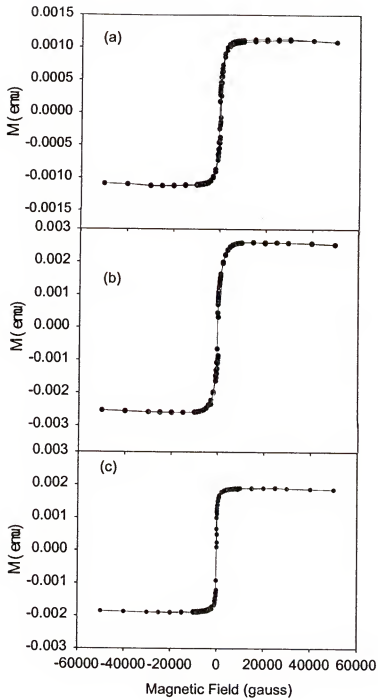


Figure 5.15: M - H curves for (a) $\text{La}_{0.7}\text{Ca}_{0.3}\text{MnO}_3$, (b) $\text{La}_{0.7}\text{Ca}_{0.2}\text{MnO}_3$, and (c) $\text{La}_{0.7}\text{MnO}_3$ at 10 K

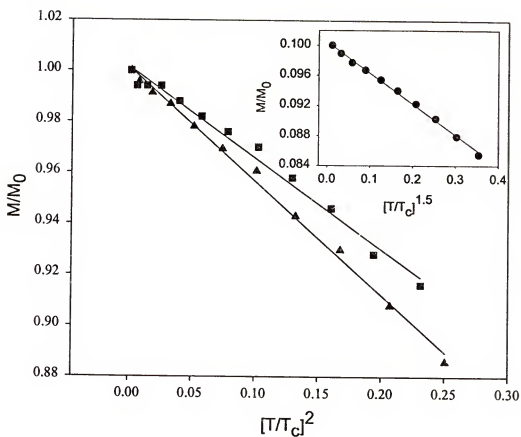


Figure 5.16: Saturation magnetization fits for $\text{La}_{0.7}\text{Ca}_{0.3}\text{MnO}_3$ (filled circle), $\text{La}_{0.7}\text{Ca}_{0.2}\text{MnO}_3$ (filled triangle), and $\text{La}_{0.7}\text{MnO}_3$ (filled square) films up to $T_c/2$

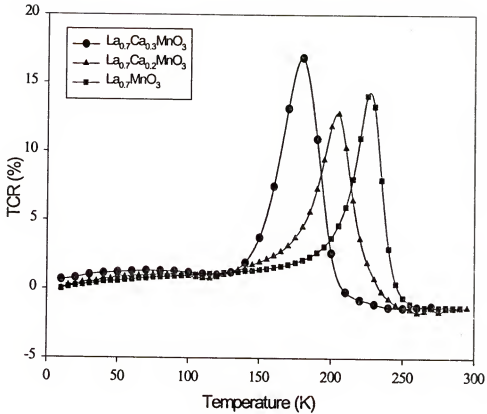


Figure 5.17: TCR and T_p for $\text{La}_{0.7}\text{Ca}_{0.3}\text{MnO}_3$ (filled circle), $\text{La}_{0.7}\text{Ca}_{0.2}\text{MnO}_3$ (filled triangle), and $\text{La}_{0.7}\text{MnO}_3$ (filled square) films

CHAPTER 6

EFFECT OF A LOCAL FERROMAGNETIC BIASING FIELD

Overview

The huge magnetoresistance (MR) of the manganite perovskites has a serious drawback due to the need for large magnetic fields to obtain such large changes of the resistance. This fact was an important handicap since many of their potential applications require a good response in the low field regime. One of the ways to reduce the external magnetic field necessary to produce the CMR effect may be to provide a local biasing field. This local biasing field may be generated either by the addition of a magnetic impurity (such as cobalt in this study) or by another ferromagnetic film in close proximity as that in a superlattice configuration. In this chapter, the effect of addition of a magnetic impurity as well as the effect of superlattice configuration is discussed in detail. In addition the effect of a non-magnetic impurity such as silver, which is known to improve the crystallinity of the films is also presented.

Effects of Magnetic and Non-Magnetic Impurity Addition

Overview

The magnetoresistance properties of the film are improved by increasing the oxygen content of the films (as has been discussed in detail in chapter 4). In the early studies on CMR materials, a post deposition anneal was critical for obtaining large magnetoresistance [Von93, Jin94]. Silver (Ag) has been used as the most suitable dopant to improve superconducting properties of bulk high T_c cuprate superconductors [Pet88,

Mat90]. Ag doping promotes crystallization, improves evaporation characteristics enhances orientation of the grains along the c axis and grain growth [Mat90, Sin92]. The high field necessary to produce the CMR effect can be reduced if we can provide a local biasing field. The local biasing field can be realized by the addition of magnetic impurities like Co.

In this study, the role of the addition of a non-magnetic impurity such as Ag and magnetic impurity such as Co on the magnetotransport and magnetic properties of $\text{La}_{0.7}\text{Ca}_{0.3}\text{MnO}_3$ films is reported.

Experimental Details

Three bulk samples of nominal composition $\text{La}_{0.7}\text{Ca}_{0.3}\text{MnO}_3$ were prepared by a ceramic method (discussed before in chapter 3). The pellets were reground and 5 wt % of silver and cobalt was added to two of the samples. The samples were repressed and sintered. EDX was done on the samples to confirm the presence of Ag and Co. The films of these materials were grown *in situ* using a pulsed laser ablation system. Details of the deposition system were mentioned in chapter 3. A 248 nm KrF pulsed laser with 5 Hz repetition rate and 1.6 J/cm^2 energy density was used. A substrate temperature of 700 – 800 °C and an oxygen pressure of 250 m Torr were used during the deposition of the films. The films deposited were characterized using x-ray diffraction (XRD) and atomic force microscopy (AFM). The temperature dependence of resistance of the films in the 10 – 300 K range was examined in zero and applied field using a four-probe technique and magnetization measurements were measured using the quantum design superconducting quantum interference device (SQUID) magnetometer. The MR ratio, $\Delta R/R(H)$, was calculated as described in chapter 3.

Results and Discussion

Structural characterization

XRD patterns of the $\text{La}_{0.7}\text{Ca}_{0.3}\text{MnO}_3$, Ag added $\text{La}_{0.7}\text{Ca}_{0.3}\text{MnO}_3$ and Co added $\text{La}_{0.7}\text{Ca}_{0.3}\text{MnO}_3$ films grown on (100) LaAlO_3 substrate at 700 °C are shown in Figure 6.1. It is clear from the figure that all the films are single phase with (00 l) peaks with $l = 1$ and 2. The presence of only (00 l) peaks implies the highly textured growth of all the films on (100) LaAlO_3 substrate. The lattice parameters of the $\text{La}_{0.7}\text{Ca}_{0.3}\text{MnO}_3$, Ag added $\text{La}_{0.7}\text{Ca}_{0.3}\text{MnO}_3$ and Co added $\text{La}_{0.7}\text{Ca}_{0.3}\text{MnO}_3$ films were found to be 3.864, 3.859 and 3.876 Å, respectively. We see that there is a slight decrease in the lattice parameter in case of Ag added $\text{La}_{0.7}\text{Ca}_{0.3}\text{MnO}_3$ films, while there is a small increase in the lattice parameter in case of Co added $\text{La}_{0.7}\text{Ca}_{0.3}\text{MnO}_3$ films. All the films were 1000 Å thick. The root mean square (rms) roughness of the films measured using AFM was found to be 2-3 nm, respectively. The value of rms roughness obtained here suggests that as-deposited manganite thin films in the present study are very smooth and the roughness is sometimes similar to the roughness of the bare substrate surface. The AFM was also run in the magnetic force measurement mode on the Co added $\text{La}_{0.7}\text{Ca}_{0.3}\text{MnO}_3$ films to see if there is any local magnetic field being created by the added Co. The measurements were unsuccessful. The probable reasons might be that the magnetic tip was not able to pick up the field from randomly distributed Co particles across the film. However, the magnetization measurements seem to provide evidence for some local biasing field from cobalt.

Magnetoresistance behavior

The variation of electrical resistance in zero and applied field (0.1 T and 5 T) as a function of temperature for $\text{La}_{0.7}\text{Ca}_{0.3}\text{MnO}_3$, Ag added $\text{La}_{0.7}\text{Ca}_{0.3}\text{MnO}_3$ and Co added

$\text{La}_{0.7}\text{Ca}_{0.3}\text{MnO}_3$ films are shown in Figure 6.2. According to the variation of resistance shown in Figure 6.2, all the three films have similar qualitative magnetotransport behavior. All the films undergo an insulator to metal (I-M) transition as the temperature is lowered and the resistance is suppressed with the application of magnetic field. The suppression in each case is maximum near the resistivity peak in zero field as frequently observed by many others in several manganite systems [Sea69, Von93, Cha93, Jin94, Ju 94]. It is interesting to note that there is a double-hump in the resistance versus temperature (R vs. T) plot of Co added LCMO film, which is apparently missing in R vs. T plots of pure and Ag added LCMO films. The presence of a double-hump may be due to the presence of two phases in the Co added LCMO films but XRD patterns of these films do not support this argument. One of the reasons might be due to the formation of cobalt oxide (discussed later in the chapter). However, it seems a more detailed study is required to propose a definite mechanism for the occurrence of the double-hump. Figure 6.3 shows the variation of MR ratios of the films calculated using the data in Figure 6.2 with temperature at 0.1 and 5 T. The figure shows that the Ag added $\text{La}_{0.7}\text{Ca}_{0.3}\text{MnO}_3$ and Co added $\text{La}_{0.7}\text{Ca}_{0.3}\text{MnO}_3$ films have higher MR ratio as compared to $\text{La}_{0.7}\text{Ca}_{0.3}\text{MnO}_3$.

Table 6.1. MR ratio (%) of the films at low and high fields

System	MR ratio (%) at 0.1 T	MR ratio at 5 T
LCMO	21.43% at 140 K	207.37% at 230 K
Ag added LCMO	435 % at 80 K	33686% at 70 K
Co added LCMO	29.9% at 50 K	633.12% at 70 K

Ag added $\text{La}_{0.7}\text{Ca}_{0.3}\text{MnO}_3$ films show enhanced MR ratio at high and low fields as compared to LCMO films (table 6.1). This enhancement might be due to the increase in the oxygen content of the film or due to an improvement in the crystallinity of the films.

XRD patterns of the films show that there is a slight decrease in the lattice parameter for Ag added $\text{La}_{0.7}\text{Ca}_{0.3}\text{MnO}_3$ films, which might indicate an increase in the oxygen content of the films. A decrease in the lattice parameter of lanthanum manganites with an increase in oxygen content has been observed by others as well [Von93, Jin94]. Such a small decrease in the lattice parameter was also observed in the high temperature argon annealed films (chapter 4). In the latter case, we assume that this decrease might be due to the uniform distribution of oxygen across the thickness of the film rather than due to the increase in the oxygen content of the film, as there is no oxygen available in the ambient. The other reason for the decrease in lattice parameter of $\text{La}_{0.7}\text{Ca}_{0.3}\text{MnO}_3$ films with Ag addition may be associated with its atomic radius. The EDX analysis carried out on silver added $\text{La}_{0.7}\text{Ca}_{0.3}\text{MnO}_3$ films and targets have shown that silver present in the film is less than 1 wt. % even though the target contained ~5 wt. % silver. A similar difference in silver content has frequently been observed in case of high temperature superconducting films and targets [Pet88, Mat90]. It is expected that the loss of silver in the films may be caused by high vapor pressure and high surface mobility of silver atoms at high temperatures of film growth. Therefore, presence of small amount of silver in $\text{La}_{0.7}\text{Ca}_{0.3}\text{MnO}_3$ films in the present study may not cause an identifiable variation in the lattice parameter. Hence the decrease in the lattice parameter may be due to the increase in the oxygen content of the film.

In chapter 4, we have discussed in detail and have concluded that the transition temperature of the films depends on the Mn^{4+} content (determined by the oxygen content of the films), while the MR behavior seems to be related to the microstructure. As-deposited films have less and non-uniformly distributed oxygen across the thickness of

the films and poor crystallinity (chapter 4). Ag added $\text{La}_{0.7}\text{Ca}_{0.3}\text{MnO}_3$ films have shown a dramatic improvement in the MR ratio (3.37×10^4 % compared to 207.37 % in as-deposited films). This drastic improvement in the MR ratio of the films may be attributed to a superior crystallinity and microstructure of Ag added $\text{La}_{0.7}\text{Ca}_{0.3}\text{MnO}_3$ films

Ag addition is known to improve the crystallinity and microstructure of the films. Due to high mobility of Ag adatoms at the surface of the substrate, which is maintained at a fairly high temperature (700 °C), they possibly act as surfactants and cause enlargement in size of the grains as well as their alignment with respect to the substrate edge [Kum93]. Enhancement in grain size reduces the number of grain boundaries over a specified surface area whereas the enhanced grain alignment results in a reduction of the width of grain boundaries. Both these factors influence the MR ratio of the films. Near the grain boundaries, the pairs of spins of Mn^{3+} and Mn^{4+} may not be parallel. As a result the electron transfer between pairs of Mn^{3+} and Mn^{4+} ions across the grain boundary is difficult and the resistance is high. An increase in the grain size reduces the amount of grain boundaries in a specified area. As a result, smaller fields are necessary to align these spins, and hence the suppression of resistance is much higher for a given magnetic field and as such higher MR ratios.

Ag added films are also known to improve the net oxygen content of the films. Hence, the Ag added $\text{La}_{0.7}\text{Ca}_{0.3}\text{MnO}_3$ films should also show an improvement in the transition temperature as compared to as-deposited films. However, we have observed a decrease in the transition temperature. The actual reason is still not understood. Co added $\text{La}_{0.7}\text{Ca}_{0.3}\text{MnO}_3$ films have shown much higher decrease in the transition temperature. The decrease in transition temperature in the latter case can; however be attributed to the

decrease in the oxygen content of the films (observed increase in the lattice parameter of the films).

Co added $\text{La}_{0.7}\text{Ca}_{0.3}\text{MnO}_3$ films show enhanced MR ratio at high and low fields as compared to $\text{La}_{0.7}\text{Ca}_{0.3}\text{MnO}_3$ films. This enhancement might be due to the presence of magnetic impurities, which provide some local magnetic field or biasing field. This would reduce the field necessary to observe the CMR effect. The evidence that the magnetic impurities provide the biasing field comes from the magnetization measurements (discussed later in the chapter).

Magnetization measurements

Figure 6.4 shows the variation of magnetization as a function of temperature for $\text{La}_{0.7}\text{Ca}_{0.3}\text{MnO}_3$, Ag added $\text{La}_{0.7}\text{Ca}_{0.3}\text{MnO}_3$ and Co added $\text{La}_{0.7}\text{Ca}_{0.3}\text{MnO}_3$ films in 0.5 T magnetic field. The saturation magnetization values calculated using the spin only moment for these films are found to be 594.8, 597.1, and 589.5 emu/cc respectively. In these calculations for saturation magnetization, the volume of each unit cell was estimated using the lattice parameter measured by XRD and assuming a cubic structure for each material. The measured values of saturation magnetization for the films were found to be 472, 746.8 and 972 emu/cc, respectively, which are quite different from the calculated values

The measured saturation magnetization value for $\text{La}_{0.7}\text{Ca}_{0.3}\text{MnO}_3$ was found to be 472 emu/cc. The measured value of saturation magnetization for pure $\text{La}_{0.7}\text{Ca}_{0.3}\text{MnO}_3$ film was less than the calculated value. This might be due to the presence of magnetic inhomogeneities. The measured value in case of Ag added and Co added $\text{La}_{0.7}\text{Ca}_{0.3}\text{MnO}_3$ films were found to be higher than the $\text{La}_{0.7}\text{Ca}_{0.3}\text{MnO}_3$ films. The higher value of magnetization in case of Ag added films could be understood from improved crystallinity

and microstructure of the films. Improved crystallinity and microstructure leads to increase magnetization values. In case of Co added $\text{La}_{0.7}\text{Ca}_{0.3}\text{MnO}_3$ films, the higher value of saturation magnetization can be attributed to metallic cobalt, which was added as a magnetic impurity.

One might rise the question that Co addition would result in the doping of the system (Co substituting for Mn in $\text{La}_{0.7}\text{Ca}_{0.3}\text{MnO}_3$). However, it should be noted that 5 wt. % cobalt was added to stoichiometric $\text{La}_{0.7}\text{Ca}_{0.3}\text{MnO}_3$ compound after its synthesis and therefore, it may not substitute any of the metal cations in the $\text{La}_{0.7}\text{Ca}_{0.3}\text{MnO}_3$, although a definite proof of this is not presently available to us. Also, it is not unlikely that Co forms an oxide during laser ablation in oxygen ambient. However as a result of non-equilibrium nature of laser ablation and very fast film growth-rate, considerable fraction of Co may not get oxidized, and hence may be present in the film as a pure metal [Sin98]. But the increase in saturation magnetization of Co-added LCMO is lower than expected if all the Co added was present in pure metal form (Co has a saturation magnetization value of 1422 emu/cc). The lesser increase in magnetization value may be associated with the formation of cobalt oxide, which is paramagnetic. This might be the reason for the double hump observed in the magnetotransport measurements. Nevertheless, the presence of some amount of unreacted Co is thought to be providing some local biasing field which manifests in the observation of enhanced MR ratio in case of Co added $\text{La}_{0.7}\text{Ca}_{0.3}\text{MnO}_3$ films.

Effect of Superlattice Configuration – Perovskite Oxide Superlattices

Overview

LaMnO_3 is the basic compound among lanthanum-based manganite systems, the transport properties of which can be varied dramatically by means of partial substitution of trivalent lanthanum ions with divalent cations (as discussed in literature review in chapter 2). Giant magnetoresistance (GMR) was observed in antiferromagnetically-coupled magnetic/nonmagnetic metallic superlattices [Bai88]. Spin dependent transmission of the conduction electrons through the non-magnetic layer gives rise to this magnetoresistance. There are relatively few studies on manganite superlattices involving perovskite manganites, which have been shown recently to exhibit magnetoresistance ratios several orders of magnitude larger than GMR superlattices [Sun95b, Gon96, Kwo97].

In this study, the results of the growth and magnetoresistance behavior of $\text{La}_{0.7}\text{MnO}_{3-\delta}$ (LMO) and $\text{Pr}_{0.65}\text{Ba}_{0.05}\text{Ca}_{0.3}\text{MnO}_{3-\delta}$ (PBCMO) superlattices in which the thickness of the PBCMO layer is varied systematically are presented. Previous studies have shown that $\text{La}_{0.7}\text{MnO}_{3-\delta}$ and $\text{Pr}_{0.65}\text{Ba}_{0.05}\text{Ca}_{0.3}\text{MnO}_{3-\delta}$ systems exhibit colossal magnetoresistance (CMR) behavior. The former has an insulator-to-metal (I-M) transition temperature of 240 K and shows an MR ratio of 700% in 5T [Pie98a] while the latter has a much lower I-M transition temperature (60 K) and MR ratio of 5.3×10^8 % in 5T magnetic field [Kum98]. It is expected that LMO, having a high transition temperature, will behave as a ferromagnetic metal and act as a biasing source for PBCMO. We have found that the superlattice structure has a profound influence on the M-I transition

temperature and MR ratio. Besides, a large enhancement in the MR ratio is observed at low temperatures compared to that of a single LMO film.

Experimental Details

LMO and PBCMO bulk targets were synthesized by a conventional ceramic route (as described in chapter 3). The LMO/PBCMO superlattices on (100)-oriented LaAlO_3 substrates were grown using a multitarget pulsed laser deposition system. A focused 248 nm KrF pulsed laser with a repetition rate of 5 Hz and 1.6 J/Cm^2 energy density was used. The films were deposited at a substrate temperature of 700°C and an oxygen pressure of 250 mTorr. The deposition rates from the LMO and PBCMO targets were calibrated against the number of laser pulses. Following the deposition, the films were cooled down to room temperature at the rate of 10°C/min and in 400 Torr of oxygen. Each superlattice is designated by a symbol n/m , where n and m represent the number of unit cells (1 u.c. $\sim 3.9 \text{ \AA}$) of LMO and PBCMO, respectively. Several superlattices in which the PBCMO thickness was varied from 1 to 8 unit cells were made. The thickness of LMO was kept constant.

The films were characterized by x-ray diffraction (XRD) and transmission electron microscopy (TEM). The temperature dependence of resistance of the films was examined in zero and applied field using a four-probe technique and the quantum design superconducting quantum interference device (SQUID) magnetometer. Both the transport current and applied field were in the film plane. The MR ratio, $\Delta R/R(H)$, was calculated as described in chapter 3. The magnetization measurements were also made with the SQUID magnetometer.

Results and Discussion

Structural characterization

X-ray scans around the first diffraction peak (100) for superlattices with various stacking periodicities are shown in Figure 6.5. Characteristic satellite peaks can be observed adjacent to the main (100) peak, indicating chemical modulation of the superlattice. Transmission electron microscopy confirmed the epitaxial growth of LMO/PBCMO superlattices. Shown in Figure 6.6 (a) is typical cross-sectional TEM micrograph involving LMO/PBCMO (18/8) superlattices and LaAlO_3 substrates. The corresponding selective area diffraction (SAD) pattern obtained from the cross-section is shown in Figure 6.6 (b). These figures indicate a cube-on-cube epitaxial relationship between the film and the substrate. The absence of interfacial contrast between LMO and PBCMO layers in the superlattice structure may be attributed to the close scattering intensities of the two layers. However, an unambiguous evidence of chemical modulation in the XRD pattern suggests clearly the formation of a superlattice structure.

Magnetoresistance behavior

The LMO film shows the familiar resistance-temperature dependence with a maximum MR ratio of about 700% near $T_c = 240$ K. PBCMO films show a much higher MR ratio of 5.6×10^6 % at 60 K (T_c). The LMO film becomes conducting and ferromagnetic below 240 K while the PBCMO film remains insulating and paramagnetic until cooled to below 60 K. We have made a series of superlattices in which the PBCMO thicknesses were varied from 1 to 8 unit cells. Figure 6.7 shows the resistance versus temperature plots for various superlattices. The shape of the resistance-temperature plots for the 18/1 and 18/2 superlattices resemble that of the individual LMO film. This may be due to short-circuit effect of the LMO films behaving as a conductor below 240 K. As the

thickness of the PBCMO layer is gradually increased, the transition temperature decreases and tends towards that of an individual PBCMO film.

To get a much better insight into the underlying transport properties of the superlattices, we concentrated on two important parameters – resistance in zero field and MR ratio in 5T. With 1 and 2 unit cells (u.c.) of PBCMO, the values of resistance in zero field for the superlattices are slightly larger compared to that of the pure LMO film. As the thickness of the PBCMO layers is increased to 5 unit cells, the resistances increase and are much higher than that of pure LMO film. Increasing the PBCMO layer thickness beyond this value does not show appreciable effect on the resistance. This indicates that the PBCMO film becomes continuous once the thickness approaches about 5 unit cells.

Varying the thickness of the PBCMO layer affects the MR ratio dramatically. In the case of superlattices with 5 and 8 unit cells of PBCMO, the MR ratio at $T = 240$ K, where the MR ratio of pure LMO film is maximum, drops significantly with increasing thickness of PBCMO films. The most interesting feature of the superlattice configuration is the enhancement of the MR ratio at lower temperatures. This enhancement is observed in films with thicknesses of above 5 unit cells of PBCMO that is in films with a continuous PBCMO film. The superlattices with less than five unit cells of PBCMO showed a MR behavior similar to that of the pure LMO films. The enhancement in MR ratio can be understood in terms of the ferromagnetic biasing field provided by the LMO films. LMO films become ferromagnetic below 240 K, and they provide an additional local bias for the PBCMO films causing them to undergo transition at a higher temperature compared to that of a pure PBCMO film.

Magnetization measurements

The evidence that there is some biasing field comes from the magnetization versus temperature plots (Figure 6.8) for the superlattices. We observe that the magnetization values of the superlattice films (with thickness of PBCMO > 5 u.c.) below 240 K are higher than those of the superlattices with PBCMO thickness less than 5 u.c.. Continuous film of PBCMO seems to form at thicknesses greater than 5 u.c.. So, we cannot comment on the magnetization values in case of films with thickness less than 5 u.c.. The increase in magnetization values for structures having PBCMO unit cells > 5 u.c. is not clearly understood. A more uniform film may be formed at this thickness and hence the effect of biasing field may be higher. A more detailed study is required to purpose a definite mechanism for the observation of high magnetization values for structures having PBCMO unit cells > 5 u.c.

Gupta et al. [Gup96] have explained the enhancement in the MR ratio in a superlattice configuration at low temperatures in terms of spin dependent scattering at the interfaces. However, LMO/PBCMO superlattices did not show significant magnetoresistance at low temperatures. The temperature dependence of resistance at low temperatures was similar to that of pure PBCMO and LMO films. This seems to suggest the absence of spin dependent scattering in our superlattices. Also our results are unlike the behavior of $\text{La}_{0.7}\text{Ca}_{0.3}\text{MnO}_{3-x}/\text{SrTiO}_3$ superlattices [Kwo97] where, at low temperatures, an enhanced magnetoresistance was observed over a broad temperature range, from 4.2 K to 150 K. Enhancement of magnetoresistance could also be due to grain boundary effects. However, the grain boundary magnetoresistance is observed at low temperatures and saturates in high field [Gup96], which is not observed in our

superlattices. Thus, enhancement of MR in these multilayer films can be due to the biasing provided by the LMO films below its transition temperature.

Conclusions

High magnetoresistance of doped manganites (CMR materials) have a potential drawback in the necessity for a high field in the Tesla range, which severely limits its practical utility. A novel approach to reduce the field scale may be to provide local biasing. In this study, we have performed experiments in which the local biasing is provided either by the addition of a magnetic impurity such as cobalt or by another ferromagnetic film in close proximity as that in a superlattice configuration.

The effects of magnetic (Co) and non-magnetic impurity addition on the magnetoresistance behavior of lanthanum manganite thin films have been investigated. The results obtained have shown that there is an enhancement in the MR ratio of the films by the addition of these impurities. The enhancement in the MR ratio in the case of Ag addition can be explained by the improvement in the crystallinity and microstructure of the films. In the case of Co addition it can be attributed to the local biasing field induced by magnetic impurities. The magnetization measurements performed on the films provide the evidence for biasing field provided by added cobalt.

The effect of superlattice structure was studied by fabricating high-quality epitaxial $\text{La}_{0.7}\text{MnO}_{3-\delta}$ (LMO, exhibiting a transition temperature of 240 K and MR ratio of 700 % in 5 T) and $\text{Pr}_{0.65}\text{Ba}_{0.05}\text{Ca}_{0.3}\text{MnO}_{3-\delta}$ (PBCMO, exhibiting a transition temperature of 60 K and MR ratio of 5.3×10^8 % in 5 T) superlattices. It was found that the thickness of the PBCMO layer greatly influences the MR ratio and transition temperature. When the thickness of the PBCMO layer is less than 5 unit cells, the

superlattice structure exhibits a behavior similar to that of an individual LMO film, which might be due to the short-circuit effect of the LMO films behaving as a conductor below 240 K. There has been an enhancement of magnetoresistance ratio at low temperatures in the case of superlattices with thickness of PBCMO greater than 5 unit cells. We attribute this enhancement to a ferromagnetic biasing provided by the LMO films. LMO films become ferromagnetic below 240 K, and they provide an additional local bias for the PBCMO films causing them to undergo transition at a higher temperature compared to that of pure PBCMO film. As the thickness of the PBCMO layer is further increased (beyond 5 unit cells), the transition temperature of the superlattice decreases and tends towards an individual PBCMO film.

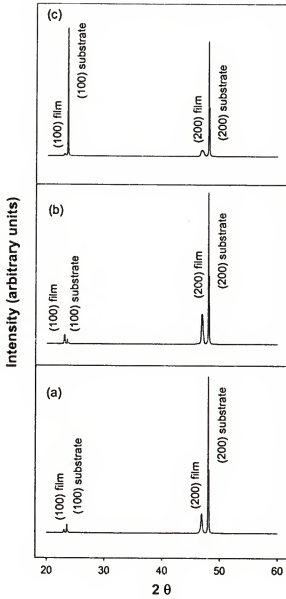


Figure 6.1: X-ray diffraction patterns of (a) $\text{La}_{0.7}\text{Ca}_{0.3}\text{MnO}_3$, (b) Ag added $\text{La}_{0.7}\text{Ca}_{0.3}\text{MnO}_3$, and (c) Co added $\text{La}_{0.7}\text{Ca}_{0.3}\text{MnO}_3$ films grown on LaAlO_3 substrates

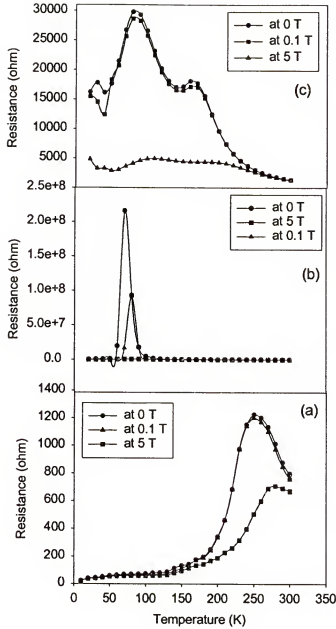


Figure 6.2: Resistance versus temperature plots for (a) $\text{La}_{0.7}\text{Ca}_{0.3}\text{MnO}_3$, (b) Ag added $\text{La}_{0.7}\text{Ca}_{0.3}\text{MnO}_3$, and (c) Co added $\text{La}_{0.7}\text{Ca}_{0.3}\text{MnO}_3$ films in 0, 0.1 and 5 T

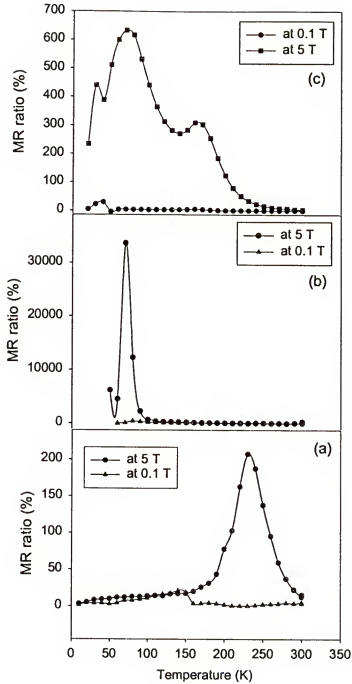


Figure 6.3: Variation of MR ratio with temperature for (a) $\text{La}_{0.7}\text{Ca}_{0.3}\text{MnO}_3$, (b) Ag added $\text{La}_{0.7}\text{Ca}_{0.3}\text{MnO}_3$, and (c) Co added $\text{La}_{0.7}\text{Ca}_{0.3}\text{MnO}_3$ films in 0.1 and 5 T

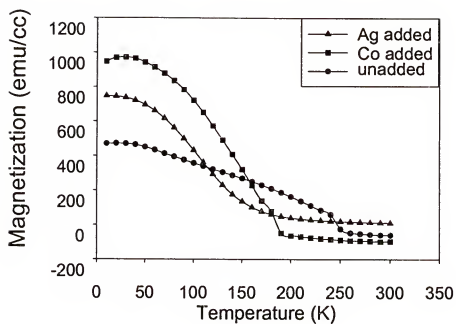


Figure 6.4: Variation of magnetization for the films with temperature at 0.5 T

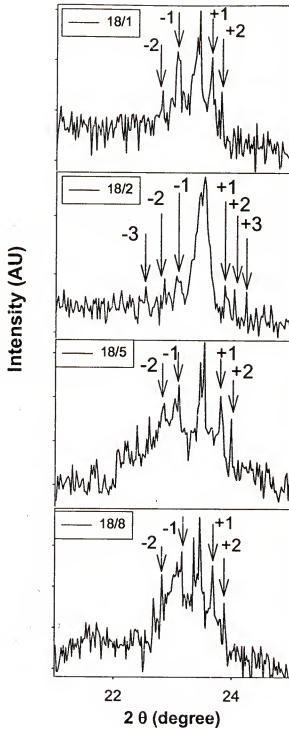
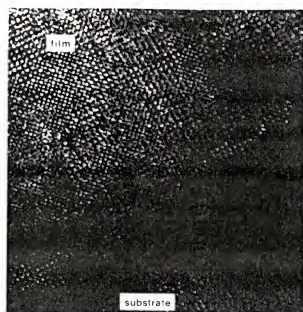
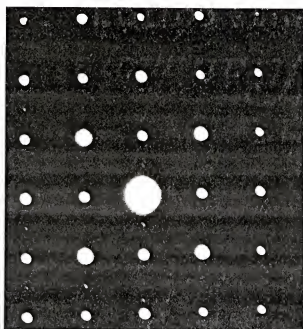


Figure 6.5: Symmetric X-ray diffraction patterns of various superlattices (legend inset shows each type of super lattice)



(a)



(b)

Figure 6.6: (a) High-resolution TEM micrograph and (b) corresponding SAD pattern of a typical superlattice (18/5)

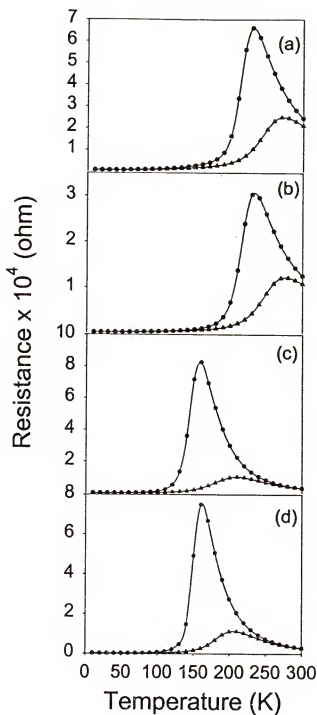


Figure 6.7: Resistance versus temperature plots for (a) 18/1, (b) 18/2, (c) 18/5, and (d) 18/8 superlattices in 0 T (circle) and 5 T (triangle) fields

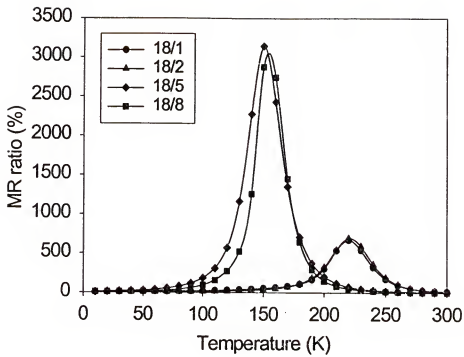


Figure 6.8: Variation of MR ratio with temperature for various superlattices in 5 T field

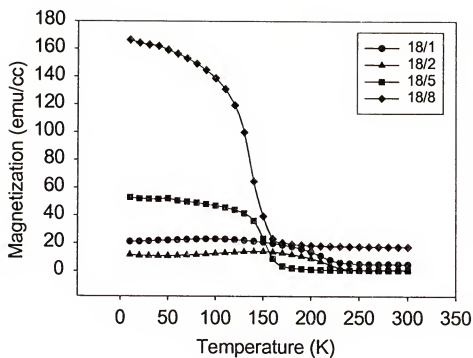


Figure 6.9: Variation of magnetization with temperature for various superlattices at 150 G

CHAPTER 7 CONCLUSIONS AND FUTURE WORK

Conclusions

In this study, experiments were conducted with a view to understand some of the outstanding issues in the area of colossal magnetoresistant thin films and to explore novel approaches to reduce the field scale necessary for obtaining high magnetoresistance values in these films.

A systematic post deposition heat treatment study showed the effect of oxygen content, crystallinity and self-doping in $\text{La}_{0.7}\text{Ca}_{0.3}\text{MnO}_3$ films deposited under identical conditions. Low temperature (500 °C) oxygen and argon anneals have shown little effect on the transition temperature or MR ratio. A High temperature (900 °C) oxygen anneal significantly improved the transition temperature of the films while high temperature (900 °C) argon anneal in the same films caused a substantial increase in the MR ratio. Vacuum annealed samples have shown deteriorated properties. The improvement in the properties of high temperature (900 °C) annealed films over as-deposited and low temperature (500 °C) annealed films can be attributed to increase in the oxygen content, uniform depth distribution of oxygen and enhancement in the crystallinity of the films. The temperature of 500 °C is therefore not a high enough temperature for either oxygen incorporation/removal or to cause recrystallization and grain growth to improve the film crystallinity. Differences in the behavior of the high temperature argon and oxygen

annealed films might be due to differences in the lanthanum vacancies and elimination of MnO fraction. The transition temperature seemed to be related to the MnO fraction in the film, while the magnetoresistance to the vacancies on the lanthanum site.

A systematic study on the microstructure, magnetoresistance and magnetic properties of $\text{La}_{0.7}\text{Ca}_{0.3}\text{MnO}_3$, $\text{La}_{0.7}\text{MnO}_3$, and $\text{La}_{0.7}\text{Ca}_{0.2}\text{MnO}_3$, which represent external, internal, and mixed doped systems with the same lanthanum content showed the presence of different scattering mechanisms and magnetic excitations. Microstructural characterization results have shown that the films are smooth, free from impurities and grow epitaxially with negligible lattice mismatch. The results obtained showed that the electronic doping in non-stoichiometric compounds is similar to that of the compounds with divalent substitution. The variation in insulator to metal transition in these systems could be explained on the basis of Mn^{4+} content. The resistance of the films seems to depend on the vacancies on the lanthanum site, while the MR property on the microstructure of the film. Analysis of low temperature resistance has shown that in $\text{La}_{0.7}\text{Ca}_{0.3}\text{MnO}_3$ and $\text{La}_{0.7}\text{Ca}_{0.2}\text{MnO}_3$ electron-electron scattering dominates while in $\text{La}_{0.7}\text{MnO}_3$ a combination of electron-electron, electron-phonon and electron-magnon scattering dominates. High temperature resistance is consistent with small polaron hopping conductivity for all the three systems. Magnetization measurements carried out on the films showed that the films have reasonably square hysteresis loops with sharp transition temperatures (T_c). Below $T_c/2$, saturation magnetization in $\text{La}_{0.7}\text{MnO}_3$ and $\text{La}_{0.7}\text{Ca}_{0.2}\text{MnO}_3$ decreases as T^2 (single particle excitations) while in $\text{La}_{0.7}\text{Ca}_{0.3}\text{MnO}_3$ it decreases as $T^{3/2}$ (collective oscillations). Of the three systems, $\text{La}_{0.7}\text{MnO}_3$ shows the best

combination of temperature coefficient of resistance (TCR) and operating temperature (T_p) for bolometric applications.

High magnetoresistance of doped manganites (CMR materials) have a potential draw back in the necessity for a high field in the Tesla range, which severely limits its practical utility. A novel approach to reduce the field scale may be to provide local biasing. In this study, we have performed experiments in which the local biasing is provided either by the addition of a magnetic impurity such as cobalt or by another ferromagnetic film in close proximity as that in a superlattice configuration.

The effects of magnetic (Co) and non-magnetic impurity addition on the magnetoresistance behavior of lanthanum manganite thin films have been investigated. The results obtained have shown that there is an enhancement in the MR ratio of the films by the addition of these impurities. The enhancement in the MR ratio in the case of Ag addition can be explained by the improvement in the crystallinity and microstructure of the films. In the case of Co addition it can be attributed to the local biasing field induced by magnetic impurities. The magnetization measurements performed on the films provide the evidence for biasing field provided by added cobalt.

The effect of superlattice structure was studied by fabricating high-quality epitaxial $\text{La}_{0.7}\text{MnO}_{3-\delta}$ (LMO, exhibiting a transition temperature of 240 K and MR ratio of 700 % in 5 T) and $\text{Pr}_{0.65}\text{Ba}_{0.05}\text{Ca}_{0.3}\text{MnO}_{3-\delta}$ (PBCMO, exhibiting a transition temperature of 60 K and MR ratio of 5.3×10^8 % in 5 T) superlattices. It was found that the thickness of the PBCMO layer greatly influences the MR ratio and transition temperature. When the thickness of the PBCMO layer is less than 5 unit cells, the superlattice structure exhibits a behavior similar to that of an individual LMO film, which

might be due to the short-circuit effect of the LMO films behaving as a conductor below 240 K. There has been an enhancement of magnetoresistance ratio at low temperatures in the case of superlattices with thickness of PBCMO greater than 5 unit cells. We attribute this enhancement to a ferromagnetic biasing provided by the LMO films. LMO films become ferromagnetic below 240 K, and they provide an additional local bias for the PBCMO films causing them to undergo transition at a higher temperature compared to that of pure PBCMO film. As the thickness of the PBCMO layer is further increased (beyond 5 unit cells), the transition temperature of the superlattice decreases and tends towards an individual PBCMO film.

Future Work

The magnetoresistance of doped manganites is of unprecedented magnitude; however, these large resistance changes are achieved only in a strong field in the Tesla range, thus severely limiting their practical utility. Reducing the field scale and increasing the operating temperature has been the goal of a number of research groups worldwide. Operating temperatures pretty close to the room temperature can and have been achieved by adjusting the processing parameters. However, the reduction of the field scale has been the bottleneck in the practical realization of these materials.

One of the other applications where this material can be used is in magnetic tunnel junctions (MTJ), which were recently shown to have tremendous potential in magnetic random access memories (MRAM). A magnetic tunnel junction consists of two ferromagnetic electrodes separated by a thin layer of an insulator, usually an oxide. The tunnel junction magnetoresistance depends on the polarizations of the two ferromagnetic materials or rather the two ferromagnetic electrodes. Theoretical calculations predict that

CMR materials are 100 % spin polarized. Experimental investigations also have shown that these materials to be highly spin polarized. Materials with a high degree of spin polarization are expected to exhibit enhanced spin dependent transport phenomenon.

Introduction of a highly spin polarized material in place of one or two of the ferromagnetic electrodes in a magnetic tunnel junction configuration should hence yield enhanced spin polarized transport and hence high magnetoresistance. Study of magnetotransport properties in such multi-layered structures is anticipated to be fruitful and to propose new device concepts based on these materials.

LIST OF REFERENCES

- Ach95 V. S. Achutharaman, P. A. Kraus, V. A. Vas'ko, C. A. Nordman, and A. M. Goldman, *Appl. Phys. Lett.* **67**, 1019 (1995).
- All98 R. Allenspach and W. Weber, *IBM J. Res. Develop.* **42**, 7 (1998).
- And55 P. W. Anderson and H. Hasegawa, *Phys. Rev.* **100**, 675 (1955).
- Arn95 Z. Arnold, K. Kamenev, M. R. Ibarra, P. A. Algarabel, C. Marquina, J. Blasco, and J. Garcia, *Appl. Phys. Lett.* **67**, 2875 (1995).
- Asa95 A. Asamitsu, Y. Moritomo, Y. Tomioka, T. Arima and Y. Tokura, *Nature* **373**, 407 (1995).
- Bae96 S.-Y. Bae and S. X. Wang, *Appl. Phys. Lett.* **69**, 121 (1996).
- Bai88 M. N. Baibich, J. M. Broto, A. Fert, F. Nguyen van Dau, F. Petroff, P. Etienne, G. Creuzet, A. Friedrich, and J. Chazelas, *Phys. Rev. Lett.* **61**, 2472 (1988).
- Bar90 J. Barnas, A. Fuss, R. E. Camley, P. Grünberg, and W. Zinn, *Phys. Rev. B* **42**, 8110 (1990).
- Bat94 C. E. Batten, K. G. Brown, and B. M. Lewis, *NASA Technical Memorandum* **4612**, Dec. (1994).
- Ben90 W. R. Bennett, W. Schwarzacher, and W. F. Egelhof, *Phys. Rev. Lett.* **65**, 3019 (1990).
- Bou99 S. Boughaba, M. U. Islam, J. A. Greer, and M. Tabat, *Vacuum and Thin Film* **2** (10), 14 (1999).
- Brio99 S. de Brion, F. Ciorcas, G. Chontea, P. Lejay, P. Radaelli, and C. Chaillont, *Phys. Rev. B* **57**, 1304 (1999).
- Bro93 J. A. Broekart, *Glow Discharge Spectroscopies*, edited by R. K. Marcus, Plenum, New York (1993).
- Bru96 James A. Brug, Thomas C. Anthony, and Janice H. Nickel, *MRS Bulletin* **23**, Sept. (1996).

- Cab97 J. A. Caballero, *Ph. D. Dissertation*, University of Florida, Gainesville (1997).
- Cam82 I. A. Campbell and A. Fert, *Ferromagnetic Materials 3*, edited by E. P. Wohlfarth, North Holland Publishing Company, Amsterdam (1982).
- Cam89 R. E. Camley and J. Barnas, *Phys. Rev. Lett.* **63**, 664 (1989).
- Cha93 K. Chahara, T. Ohno, M. Kasai, and Y. Kozono, *Appl. Phys. Lett.* **63**, 990 (1993).
- Cho90 J. Cho, M. Gomi, and M. Abe, *Jpn. J. Appl. Phys.* **29**, 1686 (1990).
- Cho97 K. G. Cho, D. Kumar, D. G. Lee, S. L. Jones, P. H. Holloway, and R. K. Singh, *Appl. Phys. Lett.* **71** (23), 3335 (1997).
- Chr94 D. B. Chrisey and G. K. Hubler, *Pulsed Laser Deposition*, Wiley, New York (1994).
- Cra98 V. Craciun, D. Craciun, and I. W. Boyd, *Electr. Lett.* **34** (15), 1527 (1998).
- Cul72 B. D. Cullity, *Introduction to Magnetic Materials*, Addison-Wesley, Massachusetts (1972).
- DeG59 P. G. De Gennes, *Phys. Rev.* **118**, 141 (1959).
- deS98 P. S. I. P. N. de Silva, F. M. Richards, L. F. Cohen, J. A. Aionso, M. J. Martinez-Lope, M. T. Casais, K. A. Thomas and J. L. MacManus-Driscoll, *J. Appl. Phys.* **83**, 394 (1998).
- Die94 B. Dieny, *J. Magn. Magn. Mater.* **136**, 335 (1994).
- Dij87 D. Dijkkamp, T. Venkatesan, X. D. Wu, S. A. Shaheen, N. Jisrawi, Y. H. Minlee, W. L. Mclean, and M. Croft, *Appl. Phys. Lett.* **51**, 619 (1987).
- Doo86 L. R. Doolittle, *Nucl. Instr. Methods Phys. Res. B* **15**, 227 (1986).
- Eve98 J. E. Evetts, M. G. Blamire, N. D. Mathur, S. P. Isaac, B.-S. Teo, L. F. Cohen, J. L. Macmanus-Driscoll, *Philos. Trans. Roy. Soc. London A* **356**, 1593 (1998).
- Fer94 A. Fert and P. Bruno, *Ultrathin Magnetic Structures II*, edited by B. Heinrich and J. A. C. Bland, Springer-Verlag, New York (1994).
- Fis89 G. Fishman and D. Calecki, *Phys. Rev. Lett.* **62**, 1302 (1989).

- Fis68 M. E. Fisher and J. S. Langer, *Phys. Rev. Lett.* **20**, 665 (1968).
- Geo94 D. B. Geohegan, *Pulsed Laser Deposition of Thin Films*, edited by D. B. Chrisey and G. K. Hubler, Wiley, New York (1994).
- Goo55 J. B. Goodenough, *Phys. Rev.* **100**, 564 (1955).
- Goo61 J. B. Goodenough, A. Wold, R. J. Arnott, and N. Menyuk, *Phys. Rev.* **124**, 373 (1961).
- Gon96 G. Q. Gong, A. Gupta, G. Xiao, P. Lecoeur, and T. R. McGuire, *Phys. Rev. B* **54**, R3742 (1996).
- Goy97 A. Goyal, M. Rajeswari, R. Shreekala, S. E. Lofland, S. M. Bhagat, T. Boettcher, C. Kwon, R. Ramesh, and T. Venkatesan, *Appl. Phys. Lett.* **71**, 2535 (1997).
- Gre94 S. M. Green, A. Pique, K. S. Harshavardhan, and J. S. Bernstein, *Pulsed Laser Deposition*, edited by D. B. Chrisey and G. K. Hubler, Wiley, New York (1994).
- Gre95 J. A. Greer and M. D. Tabat, *J. Vac. Sc. Technol. A* **13** (3), 1175 (1995).
- Gup96 A. Gupta, G. Q. Gong, G. Xiao, P. R. Duncombe, P. Trouilloud, P. Lecoeur, Y. Y. Wang, V. P. Dravid, and J. Z. Sun, *Phys. Rev. B* **54**, R15629 (1996).
- Gup95 A. Gupta, T. R. McGuire, P. R. Duncombe, M. Rupp, J. Z. Sun, W. J. Gallagher, and G. Xiao, *Appl. Phys. Lett.* **67**, 3494 (1995).
- Hec92 J. Hecht, *Laser Focus World* (June), 63 (1992).
- Hwa96 H. Y. Hwang, S.-W. Cheong, N. P. Ong, and B. Batlogg, *Phys. Rev. Lett.* **77**, 2041 (1996).
- Hwa95 H. W. Hwang, T. T. M. Palstra, S.-W. Cheong, and B. Batlogg, *Phys. Rev. B* **52**, 15046 (1995).
- Ino95 J. Inoue and S. Maekawa, *Phys. Rev. Lett.* **74**, 3407 (1995).
- Isa98 S. P. Isaac, N. D. Mathur, J. E. Evetts, M. G. Blamire, *Appl. Phys. Lett.* **72**, 2038 (1998).
- Jai96 M. Jaimie, M. B. Salamon, M. Rubinstein, R. E. Treece, J. S. Horwitz, and D. B. Chrisey, *Phys. Rev. B* **54**, 11914 (1996).

- Jin94 S. Jin, T. H. Tiefel, M. McCormack, R. A. Fastnatch, R. Ramesh, and L. H. Chen, *Science* **264**, 413 (1994).
- Jin95a S. Jin, M. O'Bryan, T. H. Tiefel, M. McCormack, and W. W. Rhodes, *Appl. Phys. Lett.* **66**, 382 (1995).
- Jin95b S. Jin, T. H. Tiefel, M. McCormack, H. M. O'Bryan, L. H. Chen, R. Ramesh and D. Schurig, *Appl. Phys. Lett.* **67**, 557 (1995).
- Jon56 G. H. Jonker, *Physica XXII*, 707 (1956).
- Jon50 G. H. Jonker and J. H. Van Santen, *Physica (Amsterdam)* **16**, 337 (1950).
- Ju 94 H. L. Ju, C. Kwon, Qi Li, R. L. Greene, and T. Venkatesan, *Appl. Phys. Lett.* **65**, 2108 (1994).
- Ju 95 H. L. Ju, J. Gopalakrishnan, J. L. Peng, Q. Li, G. C. Xiong, T. Venkatesan, and R. L. Greene, *Phys. Rev. B* **51**, 6143 (1995).
- Kas90 M. Kasai and T. Ohno, *Jpn. J. Appl. Phys.* **29**, L2219 (1990).
- Kim96 T. Kimura, Y. Tomioka, H. Kuwahara, A. Asamitsu, M. Tamura, Y. Tokura, *Science* **274**, 1698 (1996).
- Kle95 L. Klein, J. S. Dodge, T. H. Geballe, A. Kapitulnik, A. F. Marshall, L. Antognazza, and K. Char, *Appl. Phys. Lett.* **66**, 2427 (1995).
- Kub72 K. Kubo and N. Ohata, *J. Phys. Soc. Jpn.* **33**, 21 (1972).
- Kum93 D. Kumar, M. Sharon, P. R. Apte, R. Pinto, S. P. Pai, S. C. Purandare, L. C. Gupta, R. Vijayaraghavan, *Appl. Phys. Lett.* **62**, 3522 (1993).
- Kum98 D. Kumar, S. V. Pietambaram, R. K. Singh and C. B. Lee, *Mat. Res. Soc. Symp. Proc.* **517**, 171 (1998).
- Kus89 R. M. Kusters, J. Singleton, D. A. Keen, R. McGreevy, and W. Hayes, *Phys. B* **155**, 362 (1989).
- Kuw96 H. Kuwahara, Y. Tomioka, Y. Moritomo, A. Asamitsu, M. Kasai, R. Kumai, and Y. Tokura, *Science* **272**, 80 (1996).
- Kwo97 C. Kwon, K.-C. Kim, M. C. Robson, J. Y. Gu, M. Rajeswari, and T. Venkatesan, *J. Appl. Phys.* **81**, 4950 (1997).
- Lan96 M. A. Langell, C. W. Hutchings, G. A. Carson, and M. H. Nassir, *J. Vac. Sci. Technol. A* **14**, 1656 (1996).

- Leb98 O. I. Lebedev, G. Van Tendeloo, S. Amelinckx, B. Leibold and H. -U. Habermeier, *Phys. Rev. B* **58**, 8065 (1998).
- Lec97 P. Lecoeur, P. L. Trouilloud, G. Xiao, A. Gupta, G. Q. Gong, and X. W. Li, *J. Appl. Phys.* **82**, 3934 (1997).
- Lee98 D. G. Lee, *Ph. D. Dissertation*, University of Florida, Gainesville (1997).
- Lev90 P. M. Levy, S. Zhang, and A. Fert, *Phys. Rev. Lett.* **65**, 1642 (1990).
- Lof95 S. E. Lofland, and S. M. Bhagat, H. L. Lu, G. C. Xiong, T. Venkatesan, and R. L. Greene, *Phys. Rev. B* **52**, 15058 (1995).
- Lon85 G. G. Lonzarich and L. Taillefer, *J. Phys. C* **18**, 4339 (1985).
- Low96 D. H. Lowndes, D. B. Geohegan, A. A. Puretzky, D. P. Norton, and C. M. Rouleau, *Science* **273**, 898 (1996).
- Lu 96 Y. Lu, X. W. Li, G. Q. Gong, G. Xiao, A. Gupta, P. Lecoeur, J. Z. Sun, Y. Y. Wang, V. P. Dravid, *Phys. Rev. B* **54**, R8357 (1996).
- Man95 S. S. Manoharan, D. Kumar, M. S. Hegde, K. M. Satyalakshmi, V. Prasad, and S. V. Subramanyam, *J. Solid State Chem.* **117**, 420 (1995).
- Mat90 Y. Matsumoto, J. Hombo, Y. Yamaguchi, M. Nishida, and A. Chiba, *Appl. Phys. Lett.* **56**, 1585 (1990).
- Mat97 N. D. Mathur, G. Burnell, S. P. Isaac, T. J. Jackson, B.-S. Teo, J. L. MacManus-Driscoll, L. F. Cohen, J. E. Evetts, M. G. Blamire, *Nature* **387**, 266 (1997).
- Mat91 J. Mathon, *Contemp. Phys.* **32**, 143 (1991).
- McC94 M. McCormack, S. Jin, T. H. Tiefel, R. M. Fleming, Julia M. Philips, and R. Ramesh, *Appl. Phys. Lett.* **64**, 3045 (1994).
- McG75 T. R. McGuire and R. I. Potter, *IEEE Trans. Magn.* **11**, 1018 (1975).
- Meg46 H. D. Megaw, *Proc. Phys. Soc. (London)* **58**, 133 (1946)
- Mil95 A. J. Millis, P. B. Littlewood, and B. I. Shraiman, *Phys. Rev. Lett.* **74**, 5144 (1995).
- Mit96 J. F. Mitchell, D. D. Argyriou, C. D. Potter, D. G. Hinks, J. D. Jorgensen, and S. D. Bardar, *Phys. Rev. B* **54**, 6172 (1996).

- Mor96 Y. Moritomo, A. Asamitsu, H. Kuwahara, and Y. Tokura, *Nature* **380**, 141 (1996).
- Mor95 Y. Moritomo, A. Asamitsu, and Y. Tokura, *Phys. Rev. B* **51**, 16491 (1995).
- Mot64 N. F. Mott, *Adv. Phys.* **13**, 325 (1964).
- Nam01 B. C. Nam, W. S. Kim, H. S. Choi, J. C. Kim, N. H. Hur, I. S. Kim, and Y. K. Park, *J. Phys. D: Appl. Phys.* **34**, 54 (2001).
- Par94 S. S. P. Parkin, *Ultrathin Magnetic Structures II*, edited by B. Heinrich and J. A. C. Bland, Springer-Verlag, New York (1994).
- Par91 S. S. P. Parkin, *Phys. Rev. Lett.* **67**, 3598 (1991).
- Par99 F. Parmigiani, L. Sangaletti, *J. Electron Spectroscop. Rel. Phen.* **287**, 98 (1999).
- Pet88 P. N. Peters, R. C. Sisk, E. W. Urban, C. Y. Huang, and M. K. Wu, *Appl. Phys. Lett.* **52**, 2066 (1988).
- Per98 T. G. Perring, G. Aeppli, T. Kimura, Y. Tokura, M.A. Adams, *Phys. Rev. B* **58**, 14963 (1998).
- Pic96 W. E. Pickett and D. J. Singh, *Phys. Rev. B* **53**, 1146 (1996).
- Pig97 S. Pignard, H. Vincent, J. P. Senateur, J. Pierre and A. Abrutis, *J. Appl. Phys.* **82**, 4445 (1997).
- Pie98a Srinivas V. Pietambaram, D. Kumar, Rajiv K. Singh and C. B. Lee, *Phys. Rev. B* **56**, 8182 (1998).
- Pie98b Srinivas V. Pietambaram, D. Kumar, Rajiv K. Singh and C. B. Lee, *Mat. Res. Soc. Symp. Proc.* **517**, 123 (1998).
- Pie99a Srinivas V. Pietambaram, D. Kumar, Rajiv K. Singh, C. B. Lee, and Vidya S. Kaushik, *J. Appl. Phys.* **86**, 3317 (1999).
- Pie99b Srinivas V. Pietambaram, D. Kumar, Rajiv K. Singh and C. B. Lee, *Mat. Res. Soc. Symp. Proc.* **562**, 87 (1999).
- Pie00 Srinivas V. Pietambaram, D. Kumar, Rajiv K. Singh, and C. B. Lee, *Mat. Res. Soc. Symp. Proc.* **617**, J3.14.1 (2000).

- Pie01 Srinivas V. Pietambaram, D. Kumar, Rajiv K. Singh, and C. B. Lee, *Appl. Phys. Lett.* **78**, 243 (2001).
- Pre99 W. Prellier, M. Rajeswari, T. Venkatesan, and R. L. Greene, *Appl. Phys. Lett.* **75**, 1446 (1999).
- Ran96 L. Ranno, M. Viret, A. Mari, R. M. Thomas, and J. M. D. Coey, *J. Phys.: Condens. Matter* **8**, L33 (1996).
- Rad95 P. G. Radaelli, D. E. Cox, M. Marezio, S. -W. Cheong, P. E. Schiffer, and A. P. Ramirez, *Phys. Rev. Lett.* **75**, 4488 (1995).
- Rud54 M. A. Ruderman and C. Kittel, *Phys. Rev.* **96**, 99 (1954).
- Sch95 P. Schiffer, A. P. Ramirez, W. Bao, and S. -W. Cheong, *Phys. Rev. Lett.* **75**, 3336 (1995).
- Sea69 C. W. Searle and S. T. Wang, *Can. J. Phys.* **47**, 2703 (1969).
- Sea70 C. W. Searle and S. T. Wang, *Can. J. Phys.* **48**, 2023 (1970).
- Shi96 Y. Shimakawa, Y. Kubo, and T. Manako, *Nature* **379**, 53 (1996).
- Sim95 J. L. Simonds, *Physics Today* (April), 26 (1995).
- Sin90 R. K. Singh and J. Narayan, *Phys. Rev. B* **41**, 8843 (1990).
- Sin98 R. K. Singh and D. Kumar, *Mat. Sci. & Engineering Reports: A Review Journal* **R22** (4), 113 (1998).
- Sin92 R. K. Singh, D. Bhattacharya, P. Tiwari, J. Narayan, and C. B. Lee, *Appl. Phys. Lett.* **60**, 255 (1992).
- Sny96 G. J. Snyder, R. Hiskes, S. DiCarolis, M. R. Beasley, and T. H. Geballe, *Phys. Rev. B* **53**, 14434 (1996).
- Sri95 G. Srinivasan, V. S. Babu, and M. S. Seehra, *Appl. Phys. Lett.* **67**, 2090 (1995).
- Sri99 A. Srivastava, V. Craciun, J. M. Howard, and R. K. Singh, *Appl. Phys. Lett.* **75**, 3002 (1999).
- Sub96 M. A. Subramanian, B. H. Toby, A. P. Ramirez, W. J. Marshall, A. W. Sleight, and G. H. Kwei, *Science* **273**, 81 (1996).

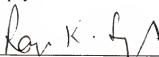
- Sun95a J. Z. Sun, L. Krusin-Elbaum, S. S. P. Parkin, and G. Xiao, *Appl. Phys. Lett.* **67**, 2726 (1995).
- Sun96a J. Z. Sun, L. Krusin-Elbaum, A. Gupta, G. Xiao, and S. S. P. Parkin, *Appl. Phys. Lett.* **69**, 1002 (1996).
- Sun96b J. Z. Sun, W. J. Gallagher, P. R. Duncombe, L. Krusin-Elbaum, R. A. Altman, A. Gupta, G. Xiao, Y. Lu, G. Q. Gong, G. Xiao, *Appl. Phys. Lett.* **69**, 3266 (1996).
- Sun00 J. R. Sun, C. F. Yeung, K. Zhao, L. Z. Zhou, C. H. Leung, H. K. Wong, and B. G. Shen, *Appl. Phys. Lett.* **76**, 1164 (2000).
- Sun95b S. Sundar Manoharan, K. M. Satyalakshmi, V. Prasad, S. V. Subramanyam, and M. S. Hegde, *Curr. Sci.* **69**, 356 (1995).
- Tof74 B. C. Tofield and W. R. Scott, *J. Solid State Chem.* **10**, 183 (1974).
- Top97 J. Topfer and J. B. Goodenough, *Chem Mater.* **9**, 1467 (1997).
- Tra96 Z. Trajanovic, C. Kwon, M. C. Robson, K. -C. Kim, M. Rajeswari, R. Ramesh, T. Venkatesan, S. E. Lofland, S. M. Bhagat, and D. Fork, *Appl. Phys. Lett.* **69**, 1005 (1996).
- Uru95 A. Urushibara, Y. Moritomo, T. Arima, A. Asamitsu, G. Kido, and Y. Tokura, *Phys. Rev. B* **51**, 14103 (1995).
- Van81 T. Van Duzer and C. W. Turner, *Principles of Super-conducting Devices and Circuits*, Elsevier, New York (1981).
- Vir97 M. Viret, M. Drouet, J. Nassar, J. P. Contour, C. Fermon, A. Fert, *Europhys. Lett.* **39**, 545 (1997).
- Von93 R. Von Helmont, J. Wecker, B. Holzapfel, L. Schultz, and K. Samver, *Phys. Rev. Lett.* **71**, 2331 (1993).
- Wei96 Z. Wei, W. Boyd, M. Elliot, and W. Herrenden-Harkerand, *Appl. Phys. Lett.* **69**, 3926 (1996).
- Wol55 E. O. Wollan and W. C. Koehler, *Phys. Rev.* **100**, 545 (1955).
- Xio97 G. C. Xiong, S. C. Wu, D. S. Dai, B. Zhang, Z. X. Lu, G. J. Lian, Z. Z. Gan, Q. Li, H. L. Ju, J. Wu, L. Senapati, R. L. Greene, and T. Venkatesan, *Phys. Rev. B.* (1997).

- Xio95a G. C. Xiong, Q. Li, H. L. Ju, S. N. Mao, L. Senapati, X. X. Xi, R. L. Greene, and T. Venkatesan, *Appl. Phys. Lett.* **66**, 1427 (1995).
- Xio95b G. C. Xiong, Qi Li, H. L. Ju, R. L. Greene, and T. Venkatesan, *Appl. Phys. Lett.* **66**, 1689 (1995).
- Xu 95 Xianfan Xu, *J. Appl. Phys.* **77**, 6715 (1995).
- Zen51 C. Zener, *Phys. Rev.* **82**, 403 (1951).
- Zen95 X. T. Zeng and H. K. Wong, *IEEE Trans. Magn.* **31**, 3910 (1995).
- Zha96 S. Zhang, *J. Appl. Phys.* **79**, 4542 (1996).

BIOGRAPHICAL SKETCH

Srinivas V. Pietambaram was born on October 30, 1974, in the city of Guntur in India. He graduated in 1996 with a bachelor's degree in engineering from Regional Engineering College, Rourkela, India, receiving a gold medal for being the best undergraduate student in the Department of Metallurgical Engineering. With inspiration from his dad, who was a professor of physics, he decided to pursue his graduate studies in the United States. He joined the University of Texas at El Paso in January 1997 and then transferred to the University of Florida in August 1997 to join Dr. Rajiv Singh's group to work in the area of electronic materials. He received his Master of Science degree with a non-thesis option in May 2000 and proceeded to work for the degree of Doctor of Philosophy. After completion, Srinivas will be joining Digital DNA laboratories of Motorola, Inc. in Phoenix, AZ.

I certify that I have read this study and that in my opinion it conforms to acceptable standards of scholarly presentation and is fully adequate, in scope and quality, as a dissertation for the degree of Doctor of Philosophy.



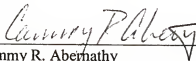
Rajiv K. Singh, Chairman
Professor of Materials Science and
Engineering

I certify that I have read this study and that in my opinion it conforms to acceptable standards of scholarly presentation and is fully adequate, in scope and quality, as a dissertation for the degree of Doctor of Philosophy.



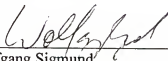
Stephen J. Pearton
Professor of Materials Science and
Engineering

I certify that I have read this study and that in my opinion it conforms to acceptable standards of scholarly presentation and is fully adequate, in scope and quality, as a dissertation for the degree of Doctor of Philosophy.




Cammy R. Abernathy
Professor of Materials Science and
Engineering

I certify that I have read this study and that in my opinion it conforms to acceptable standards of scholarly presentation and is fully adequate, in scope and quality, as a dissertation for the degree of Doctor of Philosophy.



Wolfgang Sigmund
Assistant Professor of Materials Science
and Engineering


I certify that I have read this study and that in my opinion it conforms to acceptable standards of scholarly presentation and is fully adequate, in scope and quality, as a dissertation for the degree of Doctor of Philosophy.



Fan Ren
Professor of Chemical Engineering

This dissertation was submitted to the Graduate Faculty of the College of Engineering and to the Graduate School and was accepted as partial fulfillment of the requirements for the degree of Doctor of Philosophy.

August 2001



Pramod Khargonekar
Dean, College of Engineering

Winfred Phillips
Dean, Graduate School